INTEGRATION OF RESERVOIR SIMULATION AND GEOMECHANICS

by

Nan Zhao

A dissertation submitted to the faculty of
The University of Utah
in partial fulfillment of the requirements for the degree of

Doctor of Philosophy

Department of Chemical Engineering

The University of Utah

August 2012

The University of Utah Graduate School

STATEMENT OF DISSERTATION APPROVAL

The dissertation of **Nan Zhao**

has been approved by the following supervisory committee members:

Milind D. Deo	, Chair	**5/30/2012** Date Approved
Eric G. Eddings	, Member	**5/30/2012** Date Approved
Feng Liu	, Member	**5/30/2012** Date Approved
John D. McLennan	, Member	**5/30/2012** Date Approved
Peter E. Rose	, Member	**5/30/2012** Date Approved

and by **JoAnn S. Lighty** , Chair of the Department of **Chemical Engineering**

and by Charles A. Wight, Dean of The Graduate School.

ABSTRACT

Fluid production from tight and shale gas formations has increased signicantly, and this unconventional portfolio of low-permeability reservoirs accounts for more than half of the gas produced in the United States. Stimulation and hydraulic fracturing are critical in making these systems productive, and hence it is important to understand the mechanics of the reservoir. When modeling fractured reservoirs using discrete-fracture network representation, the geomechanical effects are expected to have a signicant impact on important reservoir characteristics. It has become more accepted that fracture growth, particularly in naturally fractured reservoirs with extremely low permeability, cannot be reliably represented by conventional planar representations. Characterizing the evolution of multiple, nonplanar, interconnected and possibly nonvertical hydraulic fractures requires hydraulic and mechanical characterization of the matrix, as well as existing latent or healed fracture networks. To solve these challenging problems, a reservoir simulator (Advanced Reactive Transport Simulator (ARTS)) capable of performing unconventional reservoir simulation is developed in this research work. A geomechanical model has been incorporated into the simulation framework with various coupling schemes and this model is used to understand the geomechanical effects in unconventional oil and gas recovery. This development allows ARTS to accept geomechanical information from external geomechanical simulators (soft coupling) or the solution of the geomechanical coupled problem (hard coupling). An iterative solution method of the flow and geomechanical equations has been used in implementing the hard coupling scheme. The hard coupling schemes were verified using one-dimensional and two-dimensional analytical solutions. The new reservoir simulator is applied to learn the influence of geomechanical impact on unconventional oil and gas production in a number of practical recovery scenarios. A commercial simulator called 3DEC was the geomechanical simulator used in soft coupling. In a naturally fractured reservoir, considering geomechanics may lead to an increase or decrease in production depending on the relationship between the reservoir petrophysical properties and mechanics. Combining geomechanics and flow in multiphase flow settings showed that production decrease could be caused by a combination

of fracture contraction and water blockage. The concept of geomechanical coupling was illustrated with a complex naturally fractured system containing 44 fractures. Development of the generalized framework, being able to study multiphase flow reservoir processes with coupled geomechanics, and understanding of complex phenomena such as water blocks are the major outcomes from this research. These new tools will help in creating strategies for efficient and sustainable production of fluids from unconventional resources.

To my family

CONTENTS

LIST OF FIGURES

LIST OF TABLES

NOMENCLATURE

A Surface area of the control volume

B_p Volumetric factor for phase p

C Arbitrary property of interest

C_f Fluid compressibility

C_p Pore volume compressibility

D Coefficent matrix for strain stress relationship

F External force load

$F_{convective}$ Convective flow term

$F_{diffusive}$ Diffusive flow term

G Shear modulus

K_b Drained bulk modulus of the rock

K_g Bulk modulus of rock's individual grain

$K_{p1-p2,i}$ Thermodynamics equilibrium constant of the i component

K_{req} Chemical equilibrium constant for reaction req

K_{wb} Permeability perpendicular to well

N_c Maximum number of components

N_e Maximum number of thermal equilibrium relationships

N_f Maximum number of fluid phases

N_p Maximum number of phases

N_r Maximum number of reactions

N_v Total number of finite volumes in the reservoir discretization model

P_p Pore pressure of phase p

P_{avg} Average pore pressure

Q_p Source/sink/well molar flow rate of phase p

$Q_{Source,sink}$ Source or sink term of the property C

Q_e Heat flow through wells

Q_{loss} Heat loss to over/underburden

R Residual term of the generalized governing equation

R_{Acc} Residual term for the accumulation

R_{Flow} Residual term for flow related terms

S_p Saturation of phase p

$S_{req,i}$ Stoichiometry coefficient of i component for req chemical equilibrium reaction

T Temperature

$T_{i,I,J}$ Transmissibility between finite volumes I and J

$T_{i,j}$ Transmissivity coefficient between control volume i and j

U_p Energy per unit volume

V Volume of a arbitrary control volume

Z Elevation

a_i Activity of the i aqueous component

c_{ter} Consolidation coefficient

f Well fraction

f_h Interval length factor

h The length of the well segment

kr_p Relative permeability of phase p

$l_{x,y,z}$ Dimension of idealized matrix block in each normal direction

m_p Mobility term of phase P

p_p Pressure of flow in phase p

p_{ter} Water pressure in Terzaghi's experiment

q_p Source and sink term for phase p

q_{mf} Flow between matrix and fracture,

r_{eff} Effective radius

r_{wb} Well bore radius

t Time

u_i Deformation in i direction

v_l Fluid velocity in the reservoir

v_p	Velocity of flow in phase p
v_p	Volumetric flux of phase p
v_s	Solid velocity in the reservoir
z	Depth of the reservoir
z_{ter}	Distance along the soil column
Φ^*	Arbitrary potential term
ρ	Density of the flow media
α	Biot coefficient
$\bar{\bar{\mathbf{K}}}$	Permeability tensor
$\bar{\bar{\tau}}$	Arbitrary tensor property
$\bar{\bar{\mathbf{K}}}$	Absolute permeability
$\bar{\bar{D}}$	Diffusivity of the property of interest
$\bar{\gamma_p}$	Gravitational factor
$\bar{U}_{rock}$	Volumetric internal energy of rock
β	Coefficient of linear thermal expansion
$\delta_{i.j}$	Kronecker delta
$\dot{\rho_s}$	Real solid density of the reservoir
γ_p	Gravity density
$\hat{H}_p$	Molar enthalpy of phase p
$\hat{U}_p$	Molar internal energy of phase p
$\bar{\bar{\mathbf{K}}}_\mathbf{c}$	Thermal conductivity of rock
$\mathcal{G}$	Geometry factor
$\mathcal{L}$	Representative of matrix block dimension
$\mathcal{R}_r$	r_{th} reaction
s	Skin factor
μ	Fluid viscosity
μ_p	Viscosity of phase p, cP
ν	Poisson's ratio
ν_p	Viscosity of the flow in phase p

ω	Step length
Φ	Porosity of the reservoir
ϕ	Reservoir porosity
ϕ^*	Reservoir real porosity
$\phi_{gas,i}$	The fugacity coefficient of gas component i
Φ_p	Flow potential of phase p
ρ_f	Fluid density in the reservoir
ρ_p	Molar density of phase p
ρ_r	Average density of the reservoir
ρ_s	Solid density in the reservoir
ρ_{avg}	Average reservoir density
σ	Total stress in the reservoir
σ'	Effective stress in the reservoir
$\varepsilon_{i,j}$	Strain component
φ_p	Potential function of phase p
$\vec{\sigma}$	Vector format of total stress
$\vec{b}$	Unit external force load vector
$\vec{d}$	Search direction vector
$\vec{R}$	Residual vector
$\vec{v}$	Velocity of the flow
$\vec{Y}$	Solution space vector
ζ	Arbitrary scalar volumetric property

ACKNOWLEDGMENTS

First and foremost, I am extremely grateful to my supervising advisor, Professor Milind D. Deo, who provided knowledge, guidance, and support through some of the tough and challenging times over the last four years. I am also grateful to the members of my dissertation committee–Dr. John McLennan, Eric G. Eddings, Peter Rose and Feng Liu–for their comments and suggestions in critiquing the final draft of this dissertation.

I am thankful to all my friends at the Petroleum Research Center for their input and help during my research time. I would like to thank Dr. Chung-Kan Huang and Zhiqiang Gu, in particular, for helping me out with different aspects of reservoir engineering problems and guiding me all the way through the completion of my research.

I would like to thank all the faculty and staff of the Chemical Engineering Department for making my graduate study pleasant.

I wish to thank my friends in Salt Lake City, who I regard as family, for making my stay a memorable one. Finally, I would like to express my gratitude to my family members, especially my wife and my parents, for their unconditional love and support and for giving me courage and motivation through the difficult and enjoyable times.

CHAPTER 1

INTRODUCTION

Unconventional resources provide a significant amount of oil and gas in North America. In 2007, almost half of the natural gas production was contributed by unconventional resources [1]. In the annual energy review of 2010 [2], unconventional gas resources were predicted to be almost 60% of the total proved reserves. Unconventional oil and gas resources are those that are extracted by new technologies. These unconventional resources include oil shale, tight gas, shale gas and coal bed methane, and their extractions typically incorporate either hydraulic fracturing, thermal processing, or a combination of these and other methods [3]. Unconventional oil and gas reservoirs behave differently than conventional ones, and the production schemes are still not clearly understood. All these differences make it hard to learn and predict the reservoir behavior using conventional methods.

Reservoir simulation has proven to be a promising tool to learn about oil and gas reservoir behaviors, but it is difficult to simulate the behavior of unconventional reservoirs in an accurate manner as several physical models like geomechanics are not properly integrated. Geomechanics has proven to be important in the recovery process of unconventional oil and gas, as the permeability and porosity change significantly during this process. In order to accurately simulate unconventional oil and gas recovery processes, a geomechanical model is needed in the conventional reservoir simulator. For instance, in the hydraulic fracturing process (Figure 1.1), new fractures are created and the geomechanical properties in the reservoir, such as in situ stress and deformation, are considered to vary when compared to the original [4]. In this case, it is difficult to simulate this process as the reservoir rock media is assumed to be static. A geomechanical model must be incorporated to simulate the dynamic behavior of the reservoir induced by hydraulic fracturing. Another example is the thermal process. The reservoir has considerable deformation because of the heating in the thermal process such as field heating or steam injection. In general, the reservoir property changes induced by the geomechanical effects have impact on production and recovery.

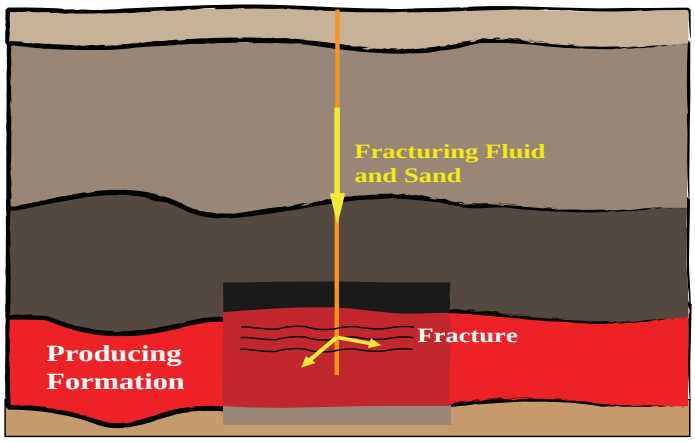

Figure 1.1: Typical hydraulic fracturing process

1.1 Unconventional Reservoir Simulation

As a result of the significance of unconventional oil and gas, several adaptations of conventional reservoir simulation are introduced to learn the behavior of unconventional reservoirs. For example thermal components have been integrated to simulate the thermal process in developing Canadian oil sand. Other components like reactive transport and geomechanics also need to be integrated to simulate recovery processes. Among all the adaptations, the integration of geomechanics with conventional reservoir simulator is the most important. With the help of geomechanics, many oil field physical phenomena such as compaction [5], subsidence, wellbore failure, and sand production can be explained. Therefore, the most important consideration in unconventional reservoir simulation is the integration of geomechanics.

1.1.1 Commercial and Research Simulators

The integration of geomechanics with reservoir simulation is generally referred to as the coupling of a geomechanical model. Conventional reservoir simulators normally do not incorporate deformation and stress changes in response to pressure, saturation and temperature changes, but instead assume that the mechanical properties do not change. The properties related to geomechanics like porosity are solely computed from rock compressibility and this is not accurate. A variety of methodologies have been introduced to take geomechanics into account. Several commercial and research reservoir simulators have been integrated with geomechanics in recent years. For Instance, ECLIPSE (a commercial reservoir simulator from Schlumberger) [6] has a geomechanical model coupled with a thermal module E300,

STARS [7] (a commercial thermal reservoir simulator from Computer Modeling Group) has integrated a thermal stress model.

Other reservoir simulators developed for research purposes are also in development to add geomechanical models in their frameworks. For example, GPRS (General Purpose Reservoir Simulator) [8] developed at Stanford University and IPARS (Integrated Parallel Accurate Reservoir Simulator) [9, 10, 11] at the University of Texas are integrating geomechanical models in the existing frameworks to learn the geomechanical effects on oil and gas recovery [12].

However, introducing geomechanical models in the conventional reservoir simulator has several limitations. The geomechanical model is typically a finite element model for the calculation of the displacement vector, while the reservoir simulation model is finite difference based. There may be some conflicts between these two discretization methods, and the computational time increases considerably. In the worst scenario, the reservoir simulator may become unstable and the result may not reflect the reality. Research and further development are still going on into integrating geomechanics in those simulators mentioned above, while more sophisticated techniques have been applied to make the unconventional reservoir simulator stable and accurate [13, 14].

1.1.2 Difficulties in Unconventional Reservoir Simulation

Geomechanical models are governed by a vector field equation set which is solved using the finite element method. Conventional reservoir models like the black oil model and thermal model, however, are governed by balance equations of scalar fields. In order to couple these two models, different schemes can be applied such as a soft coupling scheme and a hard coupling scheme. In the soft coupling approach the geomechanical problems are solved externally and the input data are generated to modify the physical properties in the conventional reservoir simulator. In contrast, hard coupling approaches solve the geomechanical problems inside the reconstructed reservoir simulator, and the solution of the two problems is simultaneous or separate. Several different variations of the hard coupling scheme can be applied to achieve optimization in respect to computational efficiency and accuracy. Different coupling schemes have been described previously [15, 16].

Coupling geomechanics with fractured systems is even more difficult. Fractures (natural or hydraulic) are thought to be the primary production pathway in the low permeability and porosity formations like shale [17]. Hence, the key component of a geomechanical coupling method is the fracture modeling method. In the conventional reservoir simulator,

the fractured reservoirs are usually modeled using single-porosity, dual-porosity or discrete fractured network representations. The integration of geomechanics with single and dual porosity fracture models has been introduced by several researches [18, 19]. It is hard, however, to model a reservoir with complex fracture networks with these approaches. The discrete fracture network method has the advantage to represent complex fracture geometry and networks, and it can be integrated with geomechanical models. This methodology may be the ideal solution to simulate a reservoir with a complex fracture network [20, 21].

As the complexity of the system increases dramatically with more models integrated in the unconventional reservoir simulation. The running speed is a big bottleneck in practical simulations. So, finding the balance of the running speed, accuracy and adaptability is a challenge. In previous studies, different models and coupling methods have been applied to overcome this problem [22, 23, 24]. Coupling geomechanics in reservoir simulators is becoming more important in the oil and gas industry, especially after the shale gas boom in North America. However, it is difficult to model the geomechanics in traditional reservoir simulation. Adding a geomechanical model in the traditional reservoir simulation dramatically increases the complexity of the system. Building a reservoir simulator with geomechanical functionality is a complex task. Two important tasks among all the tasks required to integrate geomehcanics are overcoming the difficulties due to the use of different discretization methods and improving the computational efficiency.

The method of combining DFN with geomechanics is unique. It gives us an opportunity to model real work complex systems. The integrated simulator will be capable of carrying out simulations to learn the dynamic behavior of the reservoir system, which is another significant advantage compared to conventional simulators.

1.2 Geomechanics

The record of observations related to geomechanics dates back to A.D. 77, when two men noticed that the level of water in a well corresponded to the ocean tides and then recorded this in a book [25]. Starting from 1900, more phenomena related to geomechanics were recorded by scientists through the observation of water level change in wells and other underground facilities [26]. Since then, the research of geomechanics progressed slowly. Since the petroleum exploration and production boom in the early 20th Century, more observations have been noticed in the oil and gas reservoirs which are related to geomechanics. For example, an oil field in Texas was reported to sink into the sea after oil production in the early 20th century [27]. Starting from 1920s, the research of the physical

theory behind all these observations was developed with the contribution of Biot and other scientists.

1.2.1 Theoretical Background

The theory of geomechanics was first introduced by Karl Terzaghi (1883-1963) through a series of lab experiments [28]. In these experiments, a fully saturated soil sample was confined laterally in a cylinder with a constant load. This theory can be described by the following equation:

$$\frac{\partial p_{ter}}{\partial t} = c\frac{\partial^2 p_{ter}}{\partial z_{ter}^2} \tag{1.1}$$

where c is a diffusivity known as the consolidation coefficient, t is the time, p_{ter} is the fluid pressure and z_{ter} is the distance along the soil column in the experiment. Terzaghi [29] also defined the concept of effective stress, which has influenced ongoing research today. The effective stress law describes the relationship between pore pressure and the total stress σ:

$$\sigma_{i,j} = \sigma_{i,j}^{'} \pm \delta_{i,j} p \tag{1.2}$$

where $\sigma^{'}$ is the effective stress contributed by the solid. The use of + or − in the equation is dependent on how to define the positive stress direction. If compressible stress is defined as positive, then + should be used. Later, the effective stress laws were modified by introducing a coefficient α [30, 31] in equation 1.2:

$$\sigma_{i,j} = \sigma_{i,j}^{'} \pm \alpha\delta_{i,j} p \tag{1.3}$$

where the coefficient α is the Biot parameter, and it can be calculated by:

$$\alpha = 1 - \frac{K_b}{K_g} \tag{1.4}$$

The value of α is between 0 and 1. 0 which represents rocks which are without interconnected pores, and 1 represents highly porous and compliant rocks. The physical meanings of each term in equation 3.3 can be illustrated by Figure 1.2.

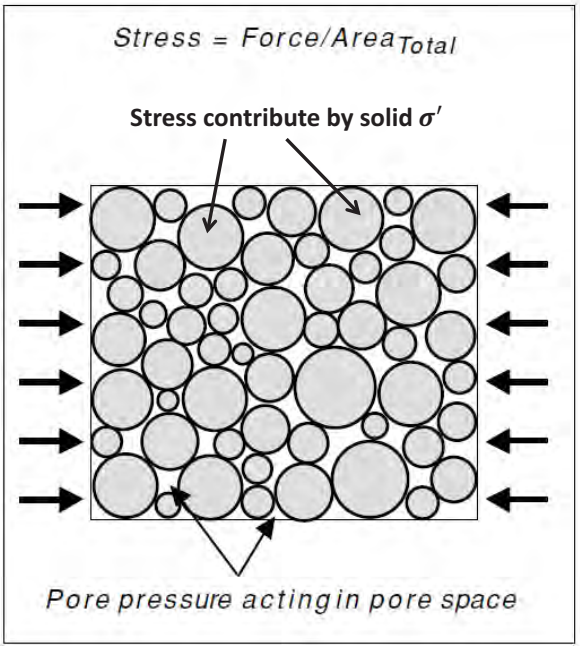

Figure 1.2: Illustration of effective stress law

Biot (1941) developed a theoretical governing equation system for the 3-D consolidation [32]. This model is considered to be the basis of computational geomechanics and this Biot 3-D consolidation model describes the soil consolidation with pore pressure change. Biot coefficient and effective stress was formally introduced in this research. This consolidation theory was later expanded to model the dynamic behavior of the soil [33]. Then, some other theories were developed for modeling fluid flow in the soil, based on Biot theory [34]. In order to deal with more complex problems, incremental forms of the Biot equation have been developed [35]. The original Biot theory has also been further developed by modifying some of his original assumptions [36].

Zienkiewicz summarized some of the research work on geomechanics and pointed out a possible numerical solution method to the dynamic problem [35]. Several other papers also introduced analytical solutions to the Biot equation. However these are extensions of the original analytical solution given by Biot, and are applicable only in limited scenarios [37]. But, with the development in Finite Element Method (FEM) and computer science, more research has been done on the numerical solution of geomechanical problems.

1.2.2 Numerical Method

Solving mechanical problems with FEM has proven to be successful in various applications and provided the basis for solving geomechanics problems numerically. The original geomechanical governing equation can be expressed in the variational formulation, and discrete formulation can be developed based on the FEM method. Finally, the system can be solved numerical with specific nonlinear and linear solvers. The advantage of this method is that the result is guaranteed to be the exact solution, because the variational formulation is mathematically identical to the original equation. Furthermore, a number of established numerical methods and codes in classical mechanical computations can be applied to geomechanics with little modification.

In order to develop the discrete formulation of the variational formulation, various methods can be applied. The Galerkin method and Least Squares(LS) method are the most common methods applied [28]. Most solid mechanics simulators prefer the Galerkin method for simplicity. Generally speaking, the FEM method is the best for solving geomechanical problems numerically. Several algorithms have been reported for the stabilization of the system and for improving the accuracy of the computation [38].

Some hybrid methods have been developed to solve geomechanics problems numerically to improve the speed of computation [39]. For example, the combination of FEM and DEM (Discrete Element Method) has been applied in flood induced landslide simulation. Particle models were also introduced to solve specific geomechanical problems such as rock failure. All these methods introduced above are computationally expensive. FLAC and 3DEC are two popular numerical codes for solving dynamic geomechanical problems. The basic methodology is DEM in both software, but the computational time is still considered to be long and the flow model coupled with the geomechanics is too simple to model the fluid flow in the reservoir [40]. Some research also introduced BEM (Boundary Element Method) in geomechanics. This method is more complicated to implement than others, and is only applied in limited scenarios.

The numerical methods for solving geomechanical problems are well established. FEM is the most common method, but is computationally challenging for dynamic problems, hence a more sophisticated method is necessary for coupling the dynamic geomechanics and flow model.

1.2.3 Constitutive Relationships

The constitutive relationships are used to describe deformation behaviors of the material during loading. Elastic, poroelastic and thermoporoelastic models are three major categories of geomechanical constitutive relationships which are widely used in reservoir simulations. The behavior of a material under load is complicated based on observations, but all the constitutive laws mentioned above are just some simplifications of reality and they can be expressed in linear or nonlinear mathematical formulations depending on the requirement of the practical application.

Figure 1.3 shows how to simplify a stress strain relationship. The point A in Figure 1.3(A) is the elastic limit of the material. Meaning that, the material behaves linearly before this point and the deformation is reversible. The point B is the yield point; the material behaves nonlinearly in the region between A and B. If the stress is unloaded, the deformation is nonreversible. In the reservoir simulation, the stress strain relationship can be simplified to linear, which is shown in Figure 1.3(B). It is also called the ideal elastic-plastic constitutive relationship. Although a linear relationship is convenient for simulation, lab experiments show that the soil never behaves linearly even in the elastic region [41]. Hence, it is important to apply the appropriate stress strain relationship to gain accuracy and efficiency. In practical unconventional reservoir simulations, the linear poroelastic model is widely applied. This model is simple but reflects the mechanical change due to pore pressure depletion. Thermoporoelastic models are more complex due to the combined effects of pressure and temperature. A large variety of constitutive relationships, which are available in the literature, based either on theory or on experimental data, can also be applied in unconventional reservoir simulation, but linear relationships are most common[42].

Another important task in applying stress constitutive relationships is to decide when the material behaves plastically, and failure criteria is used to accomplished this. In Figure 1.3, if stress loads are continuously applied to the material after point B, the material will eventual collapse or form fractures. This phenomenon is important in recovering oil and gas from ultra low permeability and porosity reservoirs, such as the created fractures (natural fractures) may be the primary flow path for the production. Furthermore, this is also important in some thermal recovery processes like SAGD (Steam Assist Gravity Drainage) as the material failure may cause the crash of the productive steam chamber. In order to avoid the damage caused by rock failure, several failure functions are applied. There are generally four kinds of classical failure functions:

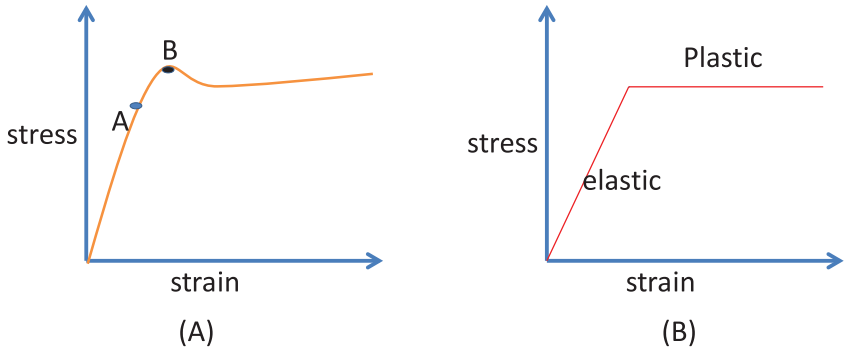

Figure 1.3: Typical stress strain relationships (A) lab experiment (B) simulator used)

1. Mohr Coulomb criterion
2. Tresca criterion
3. Von Mises criterion
4. Drucker-Prager criterion

1.3 Geomechanics in Reservoir Simulation

Since the discovery of geomechanical effect in the oil reservoir, simulation techniques have been used to prevent geomechanical disasters and predict the reservoir behavior. In modern reservoir simulations, geomechanics is the key component in simulating the unconventional reservoirs like shale gas and tight gas reservoirs. However, to include geomechanics in reservoir simulation is a difficult task and it requires a variety of advanced physical, mathematical and computational methods.

1.3.1 Field Examples

In the real reservoir system, oil, water and natural gas all exist in the pore space and fractures. Rock compaction occurs as oil and gas are produced. The magnitude of compaction depends on the geomechanical properties and the fluid flow in the reservoir. Under certain circumstances, reservoir subsidence can dramatically affect production and even safety. Consideration of geomechanics became important due to several high profile subsidence incidences.

Ekofisk is a large oil field where geomechanics has played an important role. The Ekofisk field is located in the North Sea off the coast of Norway. The total area of the North-South anticline reservoir is about 12,000 acres [43]. The chalky limestone Ekofisk and Tor formations are the producing horizons of the field. There is an extensive natural fracture

system in the field, and these fractures form the primary conductive path for production and injection. Water depth is about 235 ft (72 m) and the production rate was about 349,000 barrels/day in 1976. Seabed subsidence was first reported in 1984, with the total subsidence at about 14 ft (4.3 m) in 1989 [44]. Subsidence is also accompanied by lateral movement of the seabed towards the center of the subsidence bowl [45]. Possible reasons for subsidence have been investigated. The subsidence was believed to be related to the reservoir pressure depletion alone. However, after more observations and data collection from the production after water injection, some researchers suggested that the compaction indicated a weakening of the chalk material in contact with nonequilibrium sea water [44]. Research on 3-D finite element model to demonstrate the impact of compaction on the oil production has subsequently been performed [46].

Other field examples include the Wilmington field in California [47], Vahall field in the North Sea [48] and the South Belridge field in California [49]. All these fields had compaction and subsidence related problems with reservoir management. Research showed that the numerical modeling of geomechanics could provide guidance for reservoir management. Laboratory studies have confirmed the findings of numerical simulations. Table 1.1 summarizes some of the famous field examples of geomechanical influence.

1.3.2 Compressibility Modification

In order to solve the geomechanical problems in the field, one simplified solution was introduced in the conventional reservoir simulation. This solution was to model the change of porosity by using the pore compressibility concept. The fluid compressibility and the

Table 1.1: Some field examples of subsidence

Name of the field	Location
Venice field	Venice, Italy
Ekofisk field	North Sea, Norway
Valhall field	North Sea, Norway
Wilmington field	Long Beach, California, U.S.A
South Belridge field	Kern County, California, U.S.A
Bolivar field	Lake Maracaibo, Venezuela
Latrobe Valley field	Victoria, Australia
Wairakei field	Wairakei, New Zealand

pore volume compressibility [50] can be defined as:

$$C_f = \frac{1}{\rho}(\frac{\partial \rho}{\partial p})_T \tag{1.5}$$
$$C_p = \frac{1}{\phi}(\frac{\partial \phi}{\partial p})_T$$

where ϕ is the porosity of the reservoir, and when integrated the equation 1.5 by assuming the compressibility is fairly small:

$$\phi = \phi_0(1 + C_p(p - p_0)) \tag{1.6}$$

where φ_0 is the reference porosity, and φ is the porosity used in the reservoir simulation. The term C_p (or C_r [51] in some legacy books for reservoir simulations) refers to rock compressibility. Based on equation 1.6, the porosity will change linearly during the production as the pressure changes in the reservoir. But the equation 1.6 cannot address the geomechanical accurately when it is applied to the stress sensitive reservoir where the rock properties changes dramatically with stress evolution. In reality, the rock compressibility concept can not adequately represent the mechanical property changes of rock, this is partially because the deformation of rock may be nonlinear depending on the pore pressure as stress changes and failure happens [52]. In addition, the parameter C_p is not easy to obtain through the lab experiment. A better method to incorporate geomechanical effect in the reservoir simulation is needed to address the problem accurately, not just with a simplified assumption.

1.3.3 Geomechanical Coupling

Geomechanical coupling is introduced to accurately model the rock property change due to the geomechanical effect. One of the first researches done on geomechanical coupling was a 3-D finite element model reported by Lin and Prevost [46]. Other extensive efforts have also been reported [53]. The basis of coupling geomechanics is the Biot consolidation model, but several modifications have been introduced. The most important part of coupling geomechanics is the coupling scheme. One-way, two-way, interactive, fully and other coupling schemes have been discussed. These different coupling schemes differ in the way in which the geomechanical problem with flow is solved. The geomechanical model is introduced first before the literature review of the various coupling schemes.

The governing equation for geomechanics in reservoir simulation is based on the 3-D consolidation theory. It shows the force balance of the stress field and pore pressure field in the reservoir:

$$\nabla \cdot \sigma + \rho_r \vec{b} = 0 \tag{1.7}$$

where σ is the stress tensor and is assumed to be symmetric. Various models can be used to calculate the in-situ stress based on the characteristics of the reservoir system. The governing equation reflects the equilibrium between the stress field and the pore pressure field in the reservoir. In addition to the geomechanical governing equation, a set of conventional material balance equations will need to be solved. Several methods have been used to couple geomechanical models with reservoir models, and Figure 1.4 illustrates how different coupling schemes work.

In the one way coupling scheme, the geomechanical model is solved separately and the reservoir properties are updated from time to time. As the term indicates, information is transformed only in one direction: geomechanical model to flow simulation. Two way coupling is an extension of this concept and the data from the flow portion of the model is also used to update the geomechanical implementation. Data exchange and frequency are the considerations in making one way and two way coupling schemes work. Convergence and numerical stability are issues that these coupling schemes must deal with, and the iterative coupling scheme addresses some of these. The results from these models may not be accurate and some kind of simultaneous (geomechanics and flow) modeling may be necessary.

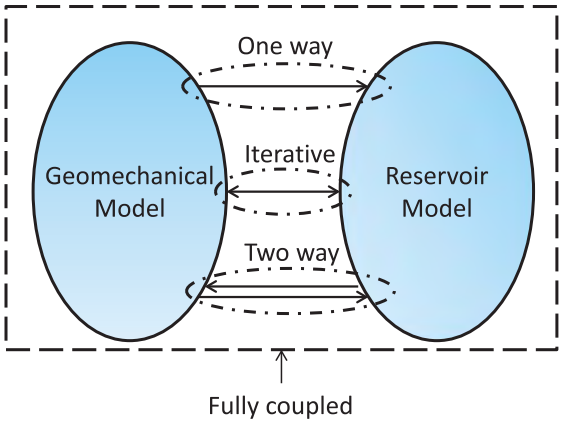

Figure 1.4: Different methods of coupling the geomechanical model in reservoir simulation

Fully coupled schemes are used to solve the geomechanical and flow problems simultaneously. The advantage of the fully coupled approach is the accuracy of the solution, but the computation complexity is significant. Matrix free algorithms have been introduced to address some of these issues [54]. The choice of the coupling schemes would depend on the required accuracy and available computation time.

In summary, adaptability, computational effort and accuracy are the three aspects of coupling a geomechanical model with reservoir simulations. Different coupling schemes and models have different characteristics with respect to these three aspects. For example, a model or coupling scheme that has good adaptability and computational speed may not have the accuracy desired. There is a trade-off between these three aspects. In the practical application, different schemes may be used based on the requirement of the project, but a coupling scheme which has reasonably good properties in all three aspects is always needed in the reservoir simulation for real oil and gas fields. Figure 1.5 represents the three aspects as the corner of a triangle, and the different coupling schemes can be fit inside the triangle to reflect the advantages and disadvantages.

1.3.4 Numerical Modeling

The numerical modeling of geomechanics in reservoir simulation follows the idea of traditional geomechanical modeling. FEM is still the default discretization method, and this is a major challenge for integrating reservoir simulation and geomechanics. In order to solve the geomechanical problems in a stable and accurate manner, several algorithms have been introduced in traditional reservoir simulation.

Mixed finite element was introduced in a research code at Stanford [55] to make the

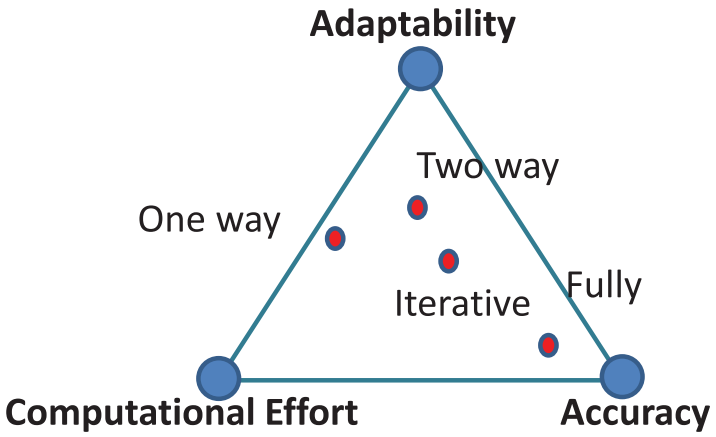

Figure 1.5: Triangle of aspects of coupling geomechanics in reservoir simulation

coupling more stable numerically. This mixed finite element formulation was first applied to Darcy flow problems to stabilize the finite element formulation and reduce the mesh dependence [56]. A mixed finite element formulation was also developed for black oil reservoir simulation [38]. Recently, a stabilization term was introduced in the discrete geomechanical governing equation to obtain fast convergence and stability [57]. Both mixed finite element and stabilization terms are targeted to solve the instability and oscillation caused by LBB (Ladyshenskaya, Babuska, Brezzi [55]) condition. However, the application of these two algorithms may increase the computational time of geomechanical simulation significantly and make it difficult for implementation.

Another numerical problem for modeling geomechanics in reservoir simulation is due to the difference between discretization methods. Most geomechanical models in reservoir simulation are FEM based, but discretization method applied to conventional reservoir simulation varies. The difference between two discretization systems contributes to the numerical instability. Schur complement was introduced to couple geomechanics with a finite difference based reservoir simulator [19, 54]. This algorithm was reported to solve part of the discretization conflict. The discretization difference is still a big challenge for coupling geomechanics even with some advanced algorithms, because the interpolation for the properties in different systems is computationally expensive.

Numerical modeling for geomechanics in reservoir simulation is well established theoretically. However, in the practical implementation and computation, stability and computational cost are challenges. Finding the balance between applying advanced algorithms and manageable computational time is another big challenge for modeling geomechanics in reservoir simulation.

1.3.5 Dynamic Modeling

One goal of performing geomechanical simulation is to predict the dynamic behavior of the reservoir such as hydraulic fracturing and reservoir compaction. To simulate that, a dynamic model of geomechanics and an appropriate reservoir model are needed. 3DEC is one of the commercial softwares with this capability, but the integrated flow model is too simple to simulate real reservoir flow. Particle and hybrid models were introduced for fracturing creation modeling, the problem for these two methods was the expensive computational cost. Other FEM based methods can also be applied in order to reduce the complexity.

The Material point method (MPM) is applied to dynamically model the geomechanics in

some research. The computational cost of this method is usually very expensive and super computers may be required. If modeling a real field project, this method is not practical. Other research uses the particle model to simulate the fracture growth dynamically, but it still has problems like slow running speed and considering multiphase fluid flow.

The other important factor of dynamic modeling is the integration of the fracture representation model. Generally speaking, three main fracture models, single porosity, dual porosity and discrete fracture network, are used in reservoir simulation. Single and dual porosity models consider matrix and fracture separately. Structured mesh is usually coupled with these types of fracture models, which makes it difficult to model the dynamic behavior. In contrast, the DFN model is able to integrate with unstructured mesh and FEM methods. These characteristics of the DFN model benefit the dynamic modeling of geomechanics in reservoir simulation. A number of papers have been published on this aspect, but there are still major difficulties for a dynamic model with reasonable computational time. The dynamic modeling is still an unsolved problem in the geomechanical modeling aspect in reservoir simulation.

1.4 Fracture Modeling

Unconventional reservoirs often contain gelogic discontinuities, such as natural fractures, faults, and damage zones. These are considered to be potential pathways for the oil and gas flow. However, modeling these geologic discontinuities in the reservoir is difficult especially in the unconventional reservoirs where geomechanics must be considered. There are three common methods of fracture modeling in conventional reservoir simulation. These models are introduced in the following sections, including the advantage and disadvantage of integrating each method in unconventional reservoir simulation.

1. Single porosity model
2. Dual porosity model
3. Discrete fractured model

1.4.1 Single Porosity Model

In the single porosity model, the fracture and matrix are considered to be the same continua with different properties. There are two approaches for the single porosity model. The first approach is to represent fracture explicitly. The fracture has the same or even thinner mesh [58, 59] compared with matrix, but different porosities and permeabilities are

assigned to fractures and matrices. Local grid refinement is usually applied to address the complexity of fractured reservoir in this approach, which results in a dramatic increase of the quantity of blocks and more computational time. Figure 1.6 shows the basic concept of this method.

The second approach is to modify the permeability term to represent fractures. In the effective permeability method, an effective permeability tensor, which can be obtained using cell-based upscale methods such as Oda's method [60] or the boundary element method[61], is calculated for a grid block to reflect the influence of fractures on fluid flow. A multiple point flow simulator was integrated with this method to perform flow simulation in fractured reservoirs [62], but the results were accurate only when the characteristic length of the fractures was smaller than the characteristic length of the grid block. Another method in this approach is the modification of the relative permeability term. The concept of pseudo relative permeability curves was introduced for modeling stratified water flooding in Hearn's work [63], but several restrictions of this method were found in other research work [64].

The single porosity model can be integrated with geomechanics with modifications of porosity and permeability terms in the reservoir simulation. However, it lacks the power for modeling complex fractures. Indeed, a mapping method is needed when a finite element geomechanical model is integrated because the default discretization method in single porosity model is the finite difference method. This also reduces the computational speed and accuracy.

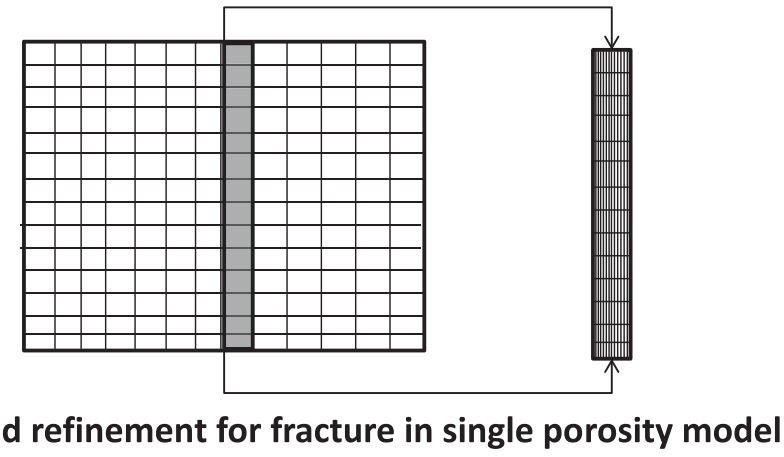

Figure 1.6: Local grid refinement used in single porosity model

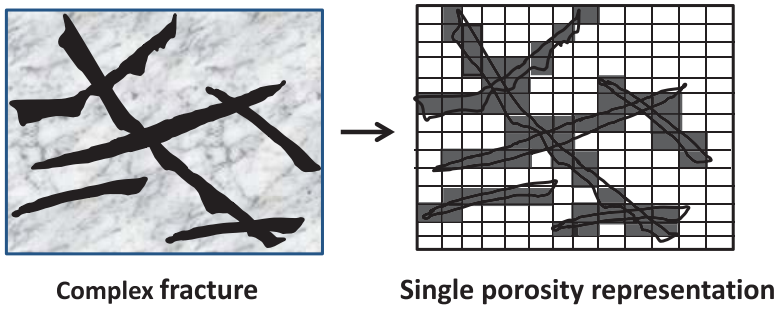

Figure 1.7: Fracture representation within a finite difference mesh using the single porosity model for 2-D complex fracture

1.4.2 Dual Porosity Model

In dual porosity model, matrices and fractures are represented separately by two different continua. This method was introduced in the research work of Warren and Root (1963) [65] to model single phase flow in fractured reservoirs. The major assumption of this model is that real reservoir can be an interconnected parallel fracture system which is surrounded by numerous small matrix blocks. This means that matrix blocks contain most of the reservoir volume and act as sources or sinks to fractures. The only fluid flow path is through fractures and all matrix blocks are isolated.

During the discretization procedure of a reservoir, fractures are represented by the connections of grid blocks and each grid block is given a fracture porosity (Figure 1.8). A grid block can have more than one matrix block. In the original dual porosity model, identical physical properties are assigned to matrix blocks. The matrix and fracture are actually in the same grid block, and the whole discretization process is just to divide the whole reservoir into two continuum models. Various models have been implemented to apply the original dual porosity model in the reservoir simulation. In most of the implementations, a shape factor is needed to calculate the flow between fracture and matrix.

Kazemi applied the dual porosity model to perform the simulation of multiphase flow in 1976 [66]. The material balance for two immiscible phases in the simulation can be represented by the following formulation:

$$\Omega_f : \quad \frac{\partial}{\partial t}(\frac{\phi S_p}{B_p})_f = q_{p,mf} + \nabla \cdot (\frac{kr_p}{\mu_p})_f \bar{\bar{\mathbf{K}}}_f \nabla \Phi_p \tag{1.8}$$

$$\Omega_m : \quad \frac{\partial}{\partial t}(\frac{\phi S_p}{B_p})_m = -q_{p,mf} \tag{1.9}$$

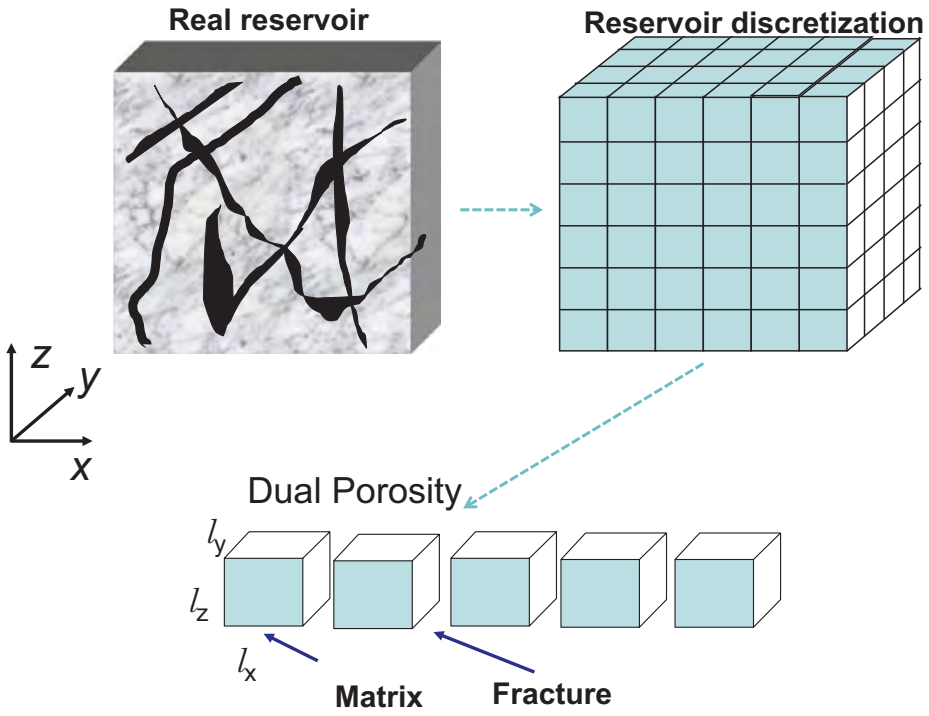

Figure 1.8: Discretization procedure for dual porosity model

The $q_{p,mf}$ term shown in Equation (1.8) and (1.9) is the matrix - fracture transfer function. It can be calculate using the shape factor:

$$q_{p,mf} = \sigma \bar{\bar{\mathbf{K}}}_m (\frac{kr_p}{\mu_p})(\Phi_{p,m} - \Phi_{p,f}) \tag{1.10}$$

Matrix permeability is used in Equation (1.10).

There are several approaches to computing shape factor (σ) (α in some references):

The first approach is the original Warren and Root formulation [65]

$$\sigma = \frac{4N(N+2)}{l^2} \tag{1.11}$$

where N is the number of normal sets of fracture that are equal to 1, 2 or 3 and l is the representative of matrix block dimension which can be computed by the following

formulations:

$$l = \begin{cases} l_x & N = 1 \\ \dfrac{2l_x l_y}{l_x + l_y} & N = 2 \\ \dfrac{3l_x l_y l_z}{l_x l_y + l_y l_z + l_x l_z} & N = 3 \end{cases} \tag{1.12}$$

$l_{x,y,z}$ is the dimension of idealized matrix block in x, y, z direction. The second approach is the Gilman and Kazemi formulation [67]

$$\sigma = 4(\frac{1}{L_x{}^2} + \frac{1}{L_y^2} + \frac{1}{L_z{}^2}) \tag{1.13}$$

where L_x, L_y, L_z are the spacing of fracture planes existing in x, y and z directions. In addition, the shape factor in transfer function has long remained controversial because a solid theoretical system was missing, and strong evidence was found for its dependence on the flow mechanism and the uniqueness of different fracture systems. Thus, it is necessary to improve the calculation of the shape factor to make the modeling of physics more rigorous.

The classic dual porosity model did not consider several important mechanisms in fracture and matrix flow exchange, such as gravity drainage, capillary continuity, re-infiltration, and viscous displacement. Many studies have been proposed to improve the dual porosity model [68, 69]. Subdomain, or "multiple-interacting continua" (MINC) refines the matrix blocks within the grid block to include the influence of the driving force gradient in matrix [70]. Two possible pseudo function methods have been investigated for capillary continuity [71, 72]. Static pseudo function computes pseudo capillary curves, which combine the capillary and gravity forces by using the vertical equilibrium assumption. The dynamic pseudo function obtains the pseudo functions from fine grid simulations or history data.

The dual porosity/dual permeability model extends the assumptions of the dual porosity model by considering both matrix-to-matrix and fracture-to-fracture flow between grid blocks . Thus, the material balances for any phase in two continua become [73, 74]:

$$\Omega_m : \quad \frac{\partial}{\partial t}(\frac{\phi S_p}{B_p})_m = q_{p,mf} + \nabla \cdot (\frac{kr_p}{\mu_p})_m \bar{\bar{\mathbf{K}}}_m \nabla \Phi_p \tag{1.14}$$

$$\Omega_f : \quad \frac{\partial}{\partial t}(\frac{\phi S_p}{B_p})_f = -q_{p,mf} + \nabla \cdot (\frac{kr_p}{\mu_p})_f \bar{\bar{\mathbf{K}}}_f \nabla \Phi_p \tag{1.15}$$

The dual porosity/dual permeability model requires greater computational effort than the dual porosity model. Figure 1.9 shows the conceptual connectivity difference among the dual porosity model, subdomain model, and dual porosity/dual permeability model in the one-dimensional domain.

However, in some applications, it is very difficult to estimate good parameters of the shape factor. The dual porosity model over-regularizes geometrical representation of the fracture network and oversimplifies assumptions of the conventional dual continuum models, which poses many uncertainties. Thus, extensive calibration techniques and accurate descriptions on the fracture network distribution and mass transfer between matrix and fractures are required before using these dual porosity models.

The coupling of geomechanics with dual porosity model is not easy and may be expensive in computational time as the challenges existed in the dual porosity model. Also, it is not easy to model the geomechanics as the two continua classifications in the reservoir. In summary, the dual porosity model is not the ideal fracture model working with geomechanics because of the complexity in computation.

1.4.3 Discrete Fracture Model

The discrete fracture model is similar to the single porosity model, but it reduces the dimensionality of the fracture instead of mesh it as same as the matrix. The dimensionality of fractures is reduced from n to $n-1$, as shown in Figure 1.10. For instance, the fracture is represented by a line in 2-D simulation and by a surface in 3-D simulation.

The discrete fracture model was introduced by Wilson and Witherspoon [75] in their work to examine fluid flow in a fractured porous medium. Two different finite element models were developed in this research for steady state flow in fractured media. In the first model, fractures were represented by triangular elements and different properties can be assigned to fractures and matrices like the single porosity model. In the second model, fractures were represented by line elements and this model required fewer nodes, hence large problem can be solved. Most of discrete fracture models developed later were based on finite element method.

Gureghian [76] developed a finite element based discrete fracture model for simulating fluid flow in a 3-D fractured porous medium. In this work, tetrahedron element represents the matrix, and the faces of a selected matrix element represent the fracture. The upstream finite element method was introduced by Noorishad (1982) [77] and Baca (1984) [78] to

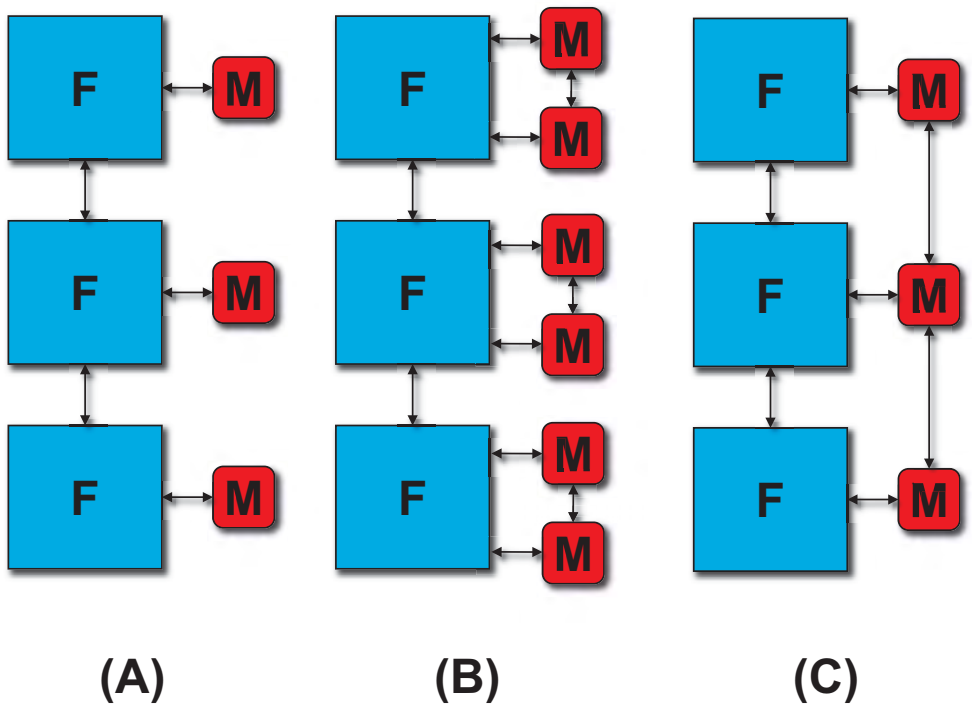

Figure 1.9: Connectivity of (A) dual porosity model, (B) subdomain model and (C) dual porosity/dual permeability model in 1-D domain

avoid the numerical oscillations that ocuured in simulating the convective dominated flow. A discrete fracture model for multiphase flow was developed by Bourbiaux (1999) [71] based on a finite volume method, and a joint-element method was applied to represent the fracture networks in his work.

In addition to the finite element based discrete fracture model, various finite difference-based discrete fracture models have also been developed. For example, Karimi-Fard et al. (2001) [79] [80] applied two point flux approximations in the control volume finite difference based reservoir simulator and introduced a technique based on a " star-delta " to eliminate control volumes at the fracture intersection, which impacted the numerical stability and computational efficiency.

In 1999, Kim [81] first developed a finite element two-phase black oil model at the University of Utah. Karimi-Fard et al. [79] applied the same method to develop a two-

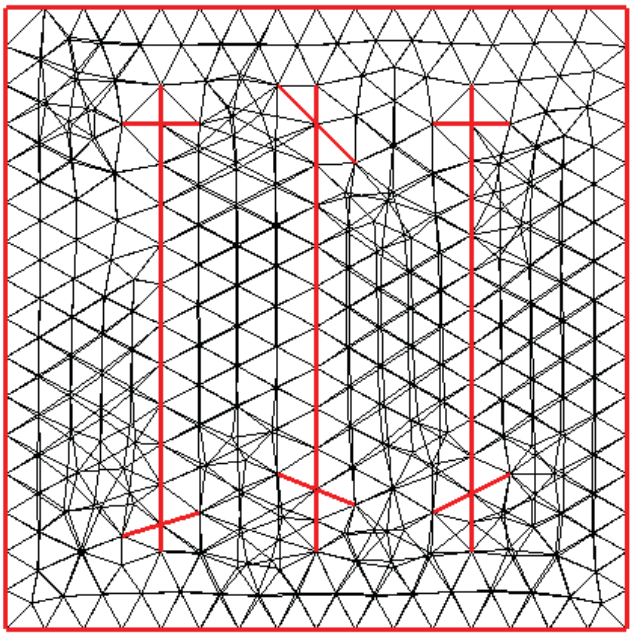

Figure 1.10: Finite element mesh for discrete fracture model, fracture is represented by a line in 2-D

phase black oil model using implicit pressure-explicit saturation (IMPES) method instead of the original the fully implicit method in Kim's work. Yang (2003) [82] and Fu (2007) [83] [84] developed a new control-volume finite element method (CVFEM) based discrete fracture model for two-phase, two-dimensional and three-phase, three-dimensional block oil simulation. Huang (2009) [85] extended the functionality of the simulator to address thermal compositional problems. Gu [86] added a reactive transport model to simulate the co_2 sequestration in geological formations.

Monteagudo et al. [87] improved the discrete network model by introducing a cross flow equilibrium concept between fracture and matrix: $\Phi_{p,m} = \Phi_{p,f}$ and suggested a variable substitution scheme to avoid singular situation. Some other works were published on treatments to reduce CPU time and memory usage, such as hybrid meshes [88], and some works are dedicated to higher-order accurate representations of the flux terms [89].

The coupling between geomechanics in a discrete network fracture model is similar to the coupling between single porosity model and geomechanics. Because the matrix and fracture are models as the same continua, it is easy to add the geomechanical effect into the calculation. Furthermore, the discrete fracture model can use finite element method, which is also applied in most geomechanical models. Hence, it would save a huge amount of computational effort by sharing discretization information.

A geomechanical model is coupled with the discrete fracture network model at the University of Utah. This coupling method can represent a complex fracture network in the real reservoir, and it is integrated with the traditional finite element model which reduces the computational complexity by avoiding massive mapping effort and information sharing.

1.5 Previous Work of the Research Group

The research group at the University of Utah has contributed significantly to the DFN model and reservoir simulation. The Utah Finite Element Simulator (UFES) has been under developed for years with the continuous contribution from group members [82, 83, 90]. The Control Volume Finite Element (CVFE) discretization method was developed for reservoir simulation [84, 91], this method has the advantage to model unstructured fracture and complex fluid flow behavior in the reservoir. A transmissibility based finite volume method was also developed to integrate the UFES with other reservoir simulators. A 3-D black oil model and Compositional K value Thermal (CKT) model were developed to simulate conventional and unconventional oil and gas recovery. A geochemical reactive transport model was also introduced for modeling co_2 sequestration and EOR [86]. Modularization implementation was applied to the CKT model development [85]. A variety of simulations have been performed previously to evaluate the UFES and to show the advantages of DFN model in modeling conventional reservoir recovery processes. In summary, the UFES developed from previous research works was proved to be effective and accurate in modeling a conventional reservoir with complex fractures.

Based on all these previous works, a generalized reservoir simulator with geomechanics (Advanced Reactive Transport Simulator (ARTS)) was developed to model the unconventional oil and gas recovery process in this research. DFN is used as the default fracture representation method, and several submodels have been implemented in ARTS to improve the computational efficiency and to extend the capability.

1.6 Summary

Narr (2006) [92] stated that "all reservoirs should be considered fractured until proven otherwise". Modeling fractures in an accurate and effective manner is important in reservoir simulation especially in unconventional reservoir simulation. In this research work, a geomechanical model is integrated with a Discrete Fracture Network (DFN) reservoir simulation framework. The DFN fracture representation method has the advantage of modeling unstructured complex fracture networks. This reservoir model is also capable of

performing reservoir simulations with finite element or finite difference methods. There are three major objectives of the research:

First, a new framework that is capable of integrating a geomechanical model and multiple physical models has been developed. The Utah Finite Element Simulators (UFES) have been developed as DFN based reservoir simulators based on research continued over a number of years at the University of Utah. Applications such as water flooding, steam flooding and co_2 sequestration can be examined with different physical models (black oil, thermal, reactive transport) and discretization methods. A new reservoir simulation framework, ARTS (Advanced Reactive Transport Simulator) was developed based on UFES. ARTS is a generic reservoir simulation framework integrated with different physical models and discretization methods. Various models including geomechanical models are integrated. Modularization, generalization and compatibility are the governing principles for the ARTS framework.

Second, a geomechanical model was developed and fully integrated with ARTS. The geomechanical is integrated with various coupling schemes and constitutive relationships. Furthermore, other modules inside ARTS can be easily combined with this geomechanical model to perform a variety of reservoir simulations. It is also possible to integrate other submodels and new schemes in the geomechanical model with the designed generic implementation.

Third, a number of reservoir simulations were performed to understand the geomechanical effect on the unconventional oil and gas recovery processes. The input data will be derived from the field, or from some physical systems with known answers, to verify the capability and accuracy of the geomechanical model. Some simulations will be performed to learn the dynamic behavior of reservoirs with few fractures, and then the same methodology will be applied to a complex reservoir system with a number of natural and hydraulic fractures. In summary, an advanced reservoir simulation framework integrated with geomechanics is developed and various applications are performed using the ARTS framework.

In this dissertation, the second chapter discusses the development work of the latest ARTS framework. Then, the third chapter discusses the governing equations and numerical methods for solving the geomechanical and reservoir models, and the coupling schemes developed in this research are also discussed. The fourth chapter discusses the discretization methods applied in solving the coupled or decoupled equations introduced in Chapter 3. A

series of verification and validation studies are discussed in Chapter 5 to show the validity of the ARTS framework. ARTS has also been applied to study various real reservoir problems related to geomechanics like the "water block" in Chapter 6. Finally, a summary of this research work and some suggested further work are discussed in Chapter 7.

CHAPTER 2

ARTS FRAMEWORK

Reservoir simulation is the science of predicting the performance of subsurface oil, gas and other reservoirs, given their geologic characteristics. A number of different physical processes occur within the reservoir over its life time. In a conventional oil reservoir, pressure depletion, oil expansion and solution gas drive are the primary production mechanisms. As the reservoir pressure declines to cause uneconomical oil rates, water is injected in the secondary recovery process. In some reservoirs, carbon dioxide is injected in a tertiary process to recover additional oil. It is not uncommon to use different types of reservoir simulators to model the primary recovery, the water flooding, and the carbon dioxide enhanced oil recovery processes. Steam is typically injected for recovering heavy oils with high viscosities. Physical mechanisms relevant to the process are usually incorporated into the simulation model. For example, when steam is injected, the thermal simulation model requires the solution of the energy balance equation, while co_2 injection usually requires the use of an equation of state thermodynamic phase behavior model. Some of the important physical processes (shown for illustration, but not all inclusive) that would make up a given physical model are shown in Figure 2.1. The multiphase, thermodynamic and thermal components are needed to address the different physical processes identified. A geomechanical model maybe necessary for describing the dynamic changes in the reservoir geological properties during the production process. A modularized framework would provide the benefit of using only the features necessary for the solution of the relevant problem. A variety of discretization methods have also been used in the solution of subsurface multiphase flow problems. The finite difference technique is the most common, but the finite element method is necessary for the representation of complex geometries. Different approaches are used to represent and model fractures, which are already discussed in Chapter 1. A generalized reservoir simulator is needed to incorporate all models mentioned previously. Indeed, as more technologies are applied in the oil and gas industry, the reservoir simulator should

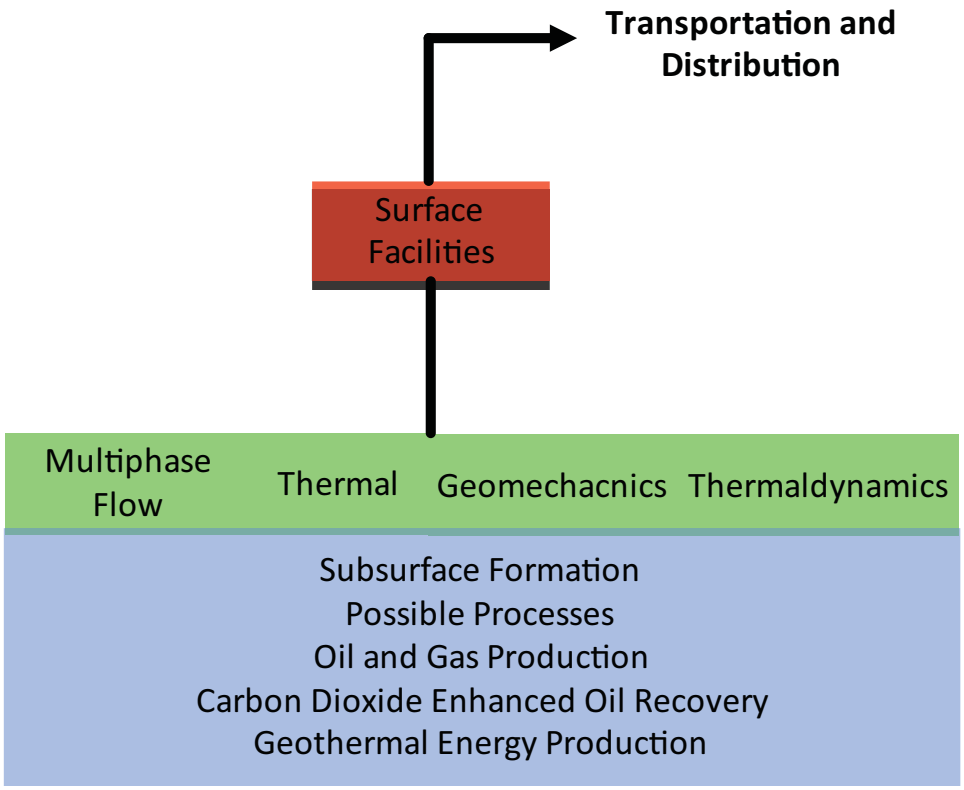

Figure 2.1: Example of physical processes involved in reservoir simulation.

have the capacity to integrate models more easily.

In order to achieve the goal of generalized reservoir simulation, Advanced Reactive Transport Simulator (ARTS) was developed. ARTS is a fully modularized frame work with various integrated models such as black oil model, compositional k value thermal model, reactive transport model, and geomechanical model. It is developed based on several years of research work in the University of Utah, and a DFN model is integrated in the frame work to represent complex natural or hydraulic fracture networks. A generic geomechanical model with different coupling schemes is also integrated in ARTS to learn unconventional oil and gas reservoirs.

2.1 Framework Structure

The structure of ARTS is designed to integrate a variety of physical and discretization models in one single framework. Indeed, it also has the capability to facilitate further development. Based on these requirements for designing the framework, the mathematical representations of an oil and gas reservoir have be generalized and then modularized in ARTS. The generalization is performed with respect to the governing equations in the

reservoir simulation. Several terms in the equation are identified to be implemented into a generic structure in the framework and these can be reused in different models. Some common numerical methods are also implemented into a generic structure to improve the efficiency. The modularization is performed with respect to the reservoir physical model (as well as geomechanical model) and domain discretization method. Various discretization schemes basically divide the subsurface into numerous, small but finite volumes in order to solve the governing equations. The selection of domain discretization method changes the way in which spatial operators and related properties (volume, depth from a datum, thickness, and the cross sectional area between control volumes) are computed. Choice of a specific domain discretization method to achieve accurate representation may depend on the specific geology of the system. Furthermore, different physical models are needed for various oil and gas recovery processes, and a geomechanical model may be important in specific reservoirs. In order to take all these models into account, ARTS has a structure that has a generic module in the higher level, with integrated modularized models in the lower level. The details of how to achieve generalization and modularization are discussed in the following sections.

2.1.1 Generalized Mass and Energy Conservation Equations

In a reservoir system, the material balance equations, energy balance equations and force balance equations describe the physical system. All these equations are essentially nonlinear partial differential equations and can be solved by using specific discretization method and physical model. In order to solve these equations in ARTS, the equations have been generalized first.

Generally speaking, the balance or conservation relationship is a scalar equation (except force). A common equation can be used to describe all of the mass conservation relationships.

If C is any scalar quantity per unit volume, the conservation of this property C is expressed by:

$$\iiint_V (\frac{\partial C}{\partial t} + Q_{source,sink})dV + \oint_A (\nabla \cdot (\vec{F}_{convective} + \vec{F}_{diffusive})dA = 0 \qquad (2.1)$$

where V is the volume and A is the surface area of any finite volume. The corresponding discrete form of Equation 2.1:

$$\Delta V(\frac{\partial C}{\partial t} + Q_{source,sink}) + \sum_{j=1}^{N_j}(\vec{F}_{convective} + \vec{F}_{diffusive})\Delta A_j = 0 \tag{2.2}$$

The equation shown above is equivalent to $R = R_{Acc} + R_{Flow} = 0$. Then the equation is divided into two terms, the flow term and the accumulation term.

The accumulation term can be calculated from the volume information of a control volume and the physical properties of the system. As shown in the equation 2.2: $R_{Acc} = \Delta V(\frac{\partial C}{\partial t} + Q_{source,sink})$, the only discretization related information is ΔV, all other terms are independent of discretization method. For the flow term, it is complex to calculate, but with further decoupling, it can be simplified.

In R_{Flow}, the convective and diffusive fluxes can be computed using the following equations:

$$\vec{F}_{convective} = C\vec{v} \tag{2.3}$$

$$\vec{F}_{diffusive} = \bar{\bar{D}}\rho\nabla(\frac{C}{\rho}) \tag{2.4}$$

where $\bar{\bar{D}}$ is the diffusivity of the property of interest, v is the velocity and ρ is the density.

In multiphase flow, volumetric flux $\vec{v}$ for phase p can be computed by the Darcy flow equation.

$$\vec{v_p} = \bar{\bar{K}}\frac{k_{rp}}{\nu_p}(\nabla p_p + \bar{\gamma_p}\nabla z) \tag{2.5}$$

where $\bar{\bar{K}}$ is the absolute permeability tensor, k_{rp} is the relative permeability, ν_p is the viscosity. Therefore, the convective flow term in the finite volume across the surface A_J can be generalized as:

$$\vec{F} \cdot \vec{A_j} = \zeta\bar{\bar{\tau}}\nabla\Phi^* \cdot A_j \tag{2.6}$$

where ζ is any arbitrary scalar volumetric property, $\bar{\bar{\tau}}$ and Φ^* are the tensor property (like permeability) and the potential of the flow respectively. For instance, in convective flux calculation, $\zeta = \frac{k_{rp}}{\nu_p}$, $\bar{\bar{\tau}} = \bar{\bar{K}}$, and the potential term is p or z. In a N_v nodes finite

element domain, Φ^* can be expressed by [83]:

$$\Phi^*(\vec{r}) = \sum_{i=1}^{N_v} \alpha_i(\vec{r})\Phi_i^* \tag{2.7}$$

Then Eq.(2.6) can be expressed as:

$$\vec{F} \cdot \vec{A_j} = \zeta \bar{\bar{\tau}} \sum_{i=1}^{N_v} \nabla\alpha_i(\vec{r})\Phi_i^* \cdot A_j = \zeta \sum_{i=1}^{N_v} T_{i,j}\Phi_i \tag{2.8}$$

where $T_{i,j}$ is the transmissivity coefficient, which is determined by domain discretization. The summation term in the above equation indicates the contributions of the potentials from a set of nodes that have flow across A_J. As a result, the following computations are only related to the discretization method:

1. The volume of the finite volume
2. The transmissivities between connected finite volumes
3. The depth or elevation of the finite volume (to compute gravitational potential)
4. The numbering index (identity) and the connectivity (graph) of finite volumes

Then the above four items can be separated from the governing equation system and treated independently. In addition, the scheme also applies to the finite difference method with a few minor modifications to the calculation of the transmissivity terms.

The scalar property C in the generalized governing equation is determined by the physical model applied to this reservoir system. For instance, in the conventional black oil model [84], the scalar property C can be described as $\frac{\Phi S_p}{B_p}$ for phase p; in compositional model, the scalar property C could be either mass density or molar density $\Phi\rho_v S_v x_{v,i}$; in energy conservation equation, the scalar property C is the energy per unit volume $\dot{U}_p\Phi\rho_p S_p + \dot{U}_r(1-\Phi)$. Also, various models can be applied to calculate the saturation, density and porosity in the physical model. All these lead to a considerable amount of individual models for representing the scalar property C. Indeed, all the computation needed for the model describing C can be accomplished with a little, or without, the spatial information.

Besides the major governing equations, several constraint equations may be required to determine the correct relationship between variables such as volume constraint and phase

equilibrium constraint. These constraint equations also do not require spatial information and therefore they are basically independent of the discretization method. In a word, the mass and energy conservation equations can be generalized and then all terms in the generalized equations can be identified as two different groups based on the dependence on the discretization methods.

2.1.2 Generalized Force Conservation Equations

The force balance equations describe the mechanical behavior of a reservoir with a set of vector equations. The following generalized formulation can be used to represent the force balance in the reservoir:

$$\nabla \cdot \sigma + \vec{F} = 0 \tag{2.9}$$

By applying the Gaussian theory, equation 2.9 can be expressed in the following formation:

$$\iiint_V (\nabla \cdot \sigma + \vec{F}) dV = 0 \tag{2.10}$$

where σ represents the stress tensor, and $\vec{F}$ represents the external force load. The force balance equation can be divided into two parts by using the same method applying in the mass and energy conservation equations. The stress term can be expressed as the following formulation:

$$\sigma = D\epsilon \tag{2.11}$$

The coefficient matrix D is independent of discretization method, but the calculation of $\nabla\sigma$ is dependent on the discretization method used. After applying the same analysis for all terms in equation 2.10, all discretization method related terms are listed as follows:

1. The volume of a geomechanical control volume
2. The integration calculation
3. The stress gradient calculation

The terms listed above can be treated independently in respect to what models are applied to the stress, and a separated module can be implemented to calculate these terms. In addition, the module designed for calculating these terms can be reused to calculate the discretization related terms discussed in section 2.1.1. Other terms that are independent of discretization method can be calculated in another module. All terms in the force balance equations can be divided into two groups using the same methods discussed in section 2.1.1. After the generalization of the governing equations in a reservoir simulation, two "independent" groups of terms in the generalized equations are identified. This is the basic modularization structure of ARTS, and it will be discussed in the following section.

2.1.3 Modularization

Based on the analysis in the previous sections, two basic modules have been designed and implemented in ARTS. An independent module called DM (Discretization Method), which was related only to spatial information of the reservoir, calculates all the discretization method dependent terms in the governing equations. Another module called PM (Physical Model) calculates all the other terms in the governing equations. For example, the volume information and spacial derivatives are calculate in DM, the viscosity and relative permeability are calculate in the PM. The PM and DM modules are the high level structure of the ARTS, a variety of submodels are implemented in each module. In the latest version of ARTS, three major DM modules and several PM modules are implemented. Indeed, several other modules served as the utility purpose are implemented such as XML for data I/O. The basic flow chart of the simulation is shown in Figure 2.2. In DM, Finite Difference (SFD), Control Volume Finite Element (CVFE) and Finite Volume (FVM) are implemented. In PM, BO (Black Oil model), CKT (Compositional K-value Thermal model) and CKT-RT (CKT model with Reactive Transport) are implemented, and each module has several submodules to model different physical systems.

The structure of ARTS is a like a "tree" with two major branches and numerous small branches. PM and DM are the two major branches and other submodels with in them are those small branches. Other needed models can be added to this open structure either as a major branches or as a small branches underneath other models. The higher level models serve as the communication pathway between different lower level models. This design also minimizes the amount of information transported through different models as only the key properties are transported. The information is shared between models that are underneath the same higher level models through a public data I/O module design.

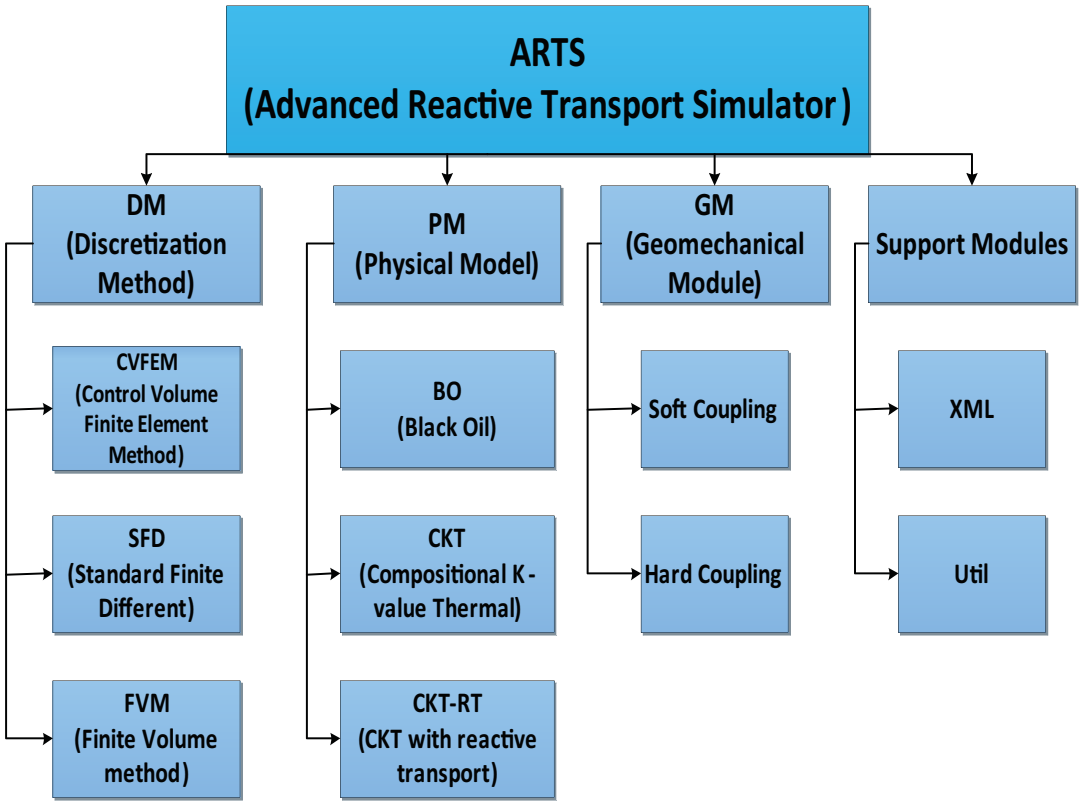

Figure 2.2: Flow chart of ARTS

For example, a problem needs to be solved with finite difference method and black oil model. The solving procedure includes the communication between modules SFD and BO, and the only pathway of this transportation is the SFD-DM-PM-BO route. Information transported in this case is only the pressure and the discretization information (gradient calculation results), other information needed in the calculation is calculated locally inside each module. If black oil module and reactive transport module need the oil property information, they get it directly from public available PM data structure, the same method applied to the information sharing between submodels of DM. This unique information transportation design and the "tree" structure can be represented by Figure 2.3.

ARTS provides a "plug in and use" environment for coupling different discretization and physical models through the "tree" structure. Different application programs can be derived in ARTS, some examples are CVFEBO (three-phase black oil simulator with control volume finite element), SDFBO (three-phase black oil simulator with finite difference, CVFECKT (compositional K value thermal model with control volume finite element), etc. More applications would be developed as potential models integrated, such as geomechanics. Now

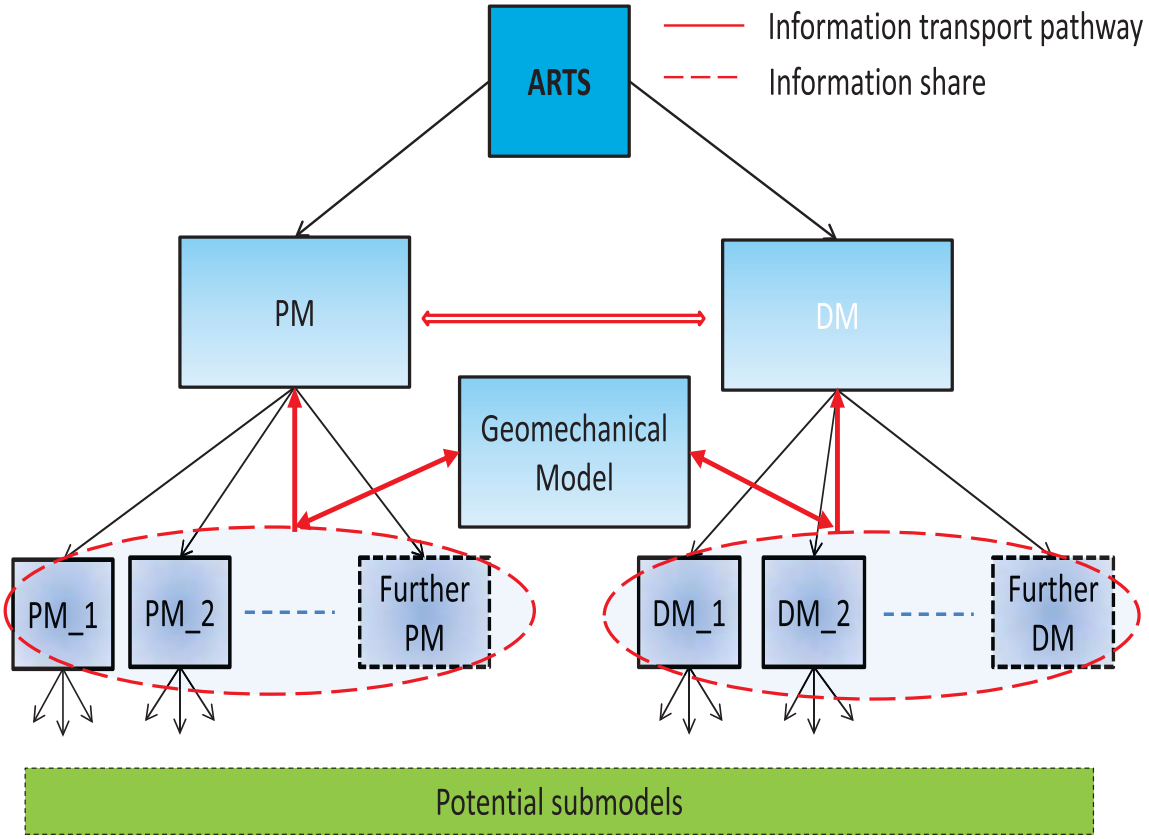

Figure 2.3: Information transport pathway and "tree" structure of ARTS

each application program in ARTS has the option to include geomechanics or not, and this doubles the number of programs.

A generalized Finite Volume Method is introduced in ARTS, which requires only the transmissivity information. This feature enables the simulator to interface with other commercial simulators. For instance, ARTS can obtain geometry related information from a commercial program and run a specific physical model with that information. This allows ARTS to couple with sophisticated geological packages.

In order to illustrate the procedure of how to solve the generalized equation in the modularized framework, the following shows how to apply a single phase black oil model (neglect the source term and diffusive term for convenience) and finite difference method to a reservoir with 100 control volumes through the modularization process discussed above. In this situation, 100 equations of mass conservation need to be solved at least. The modularized computation procedure can be applied to this specific case in the following steps:

1. Rewrite the governing equation into decoupled form:

$$\Delta V(\frac{\partial}{\partial t}(\frac{\Phi S_g}{B_g})) + \sum_{j=1}^{N_j}(\vec{F}_{Convective,g})\Delta A_j = 0$$

$$\vec{F}_{Convective,g} = \bar{\bar{K}}\frac{k_{rg}}{B_g\nu_g}(\Delta p_g + \gamma_g \Delta z)$$

2. Classify each term in the equation as DM or PM:
   ΔV,ΔA,$\Delta P_g + \gamma_g \Delta Z$ should be in the DM category. Other terms belong to the PM category.

3. Calculate each term in different modules:
   Calculating terms listed in the second step with the property data provided by different modules.

4. Apply the Newton method to the governing equation and then write it into matrix form for all control volumes.

$$\begin{pmatrix} -\frac{\partial R_1}{\partial v_1} & -\frac{\partial R_1}{\partial v_2} & \cdots & -\frac{\partial R_1}{\partial v_{100}} \\ -\frac{\partial R_2}{\partial v_1} & -\frac{\partial R_2}{\partial v_2} & \cdots & -\frac{\partial R_2}{\partial v_{100}} \\ -\frac{\partial R_3}{\partial v_1} & -\frac{\partial R_3}{\partial v_2} & \cdots & -\frac{\partial R_3}{\partial v_{100}} \\ \vdots & \vdots & \vdots & \vdots \\ -\frac{\partial R_{100}}{\partial v_1} & -\frac{\partial R_{100}}{\partial v_2} & \cdots & -\frac{\partial R_{100}}{\partial v_{100}} \end{pmatrix} \times \begin{pmatrix} \partial v_1 \\ \partial v_2 \\ \partial v_3 \\ \vdots \\ \partial v_{100} \end{pmatrix} = \begin{pmatrix} R_1 \\ R_2 \\ R_3 \\ \vdots \\ R_{100} \end{pmatrix}$$

2.1.4 Geomechanical Module Design

The geomechanical module is designed to be partially dependent on PM and DM. This design makes it easy for information sharing between geomechanical modules and other modules. As discussed in the previous sections, the term $\nabla \cdot \sigma$ is divided into two parts; one part is the calculation of ∇ operator, another part is the calculation of the stress. DM is in charge of dealing with the first part and the second part is calculated in PM. The whole term is finally assembled and calculated in PM.

Multiple coupling schemes and constitutive relationships have also been integrated in the geomechanical model in ARTS, hence different models can be applied based to simulate the diversified real reservoirs. Two different major modules, which are soft coupling and hard coupling, are implemented to control the coupling process in ARTS. Each coupling scheme has various submodels integrated, such as two way coupling scheme and iterative coupling

scheme in the hard coupling module. The communication between geomechanical modules and other modules mainly follows the communication pathway discussed in section 2.1.4. But, the geomechanical module also directly communicates with the submodels inside DM or PM (as shown in the dashed line in Figure 2.4). The purpose of this structure is to make the geomechanical model compatible with any existing or future potential submodels built in PM and DM.

2.1.5 Integration of Different Modules

The integration of different models is done during the compile time, and SCONS [93] is used in ARTS to achieve this goal. In the compiling process, a module in PM and a module in DM need to be selected by specific compiler, then a final program is built. Various of the final programs are available after this process, and the amount of final programs can be doubled if geomechanical models are also involved. Figure 2.5 shows the procedure of integration. For example, shale gas production process needs to be simulated in ARTS, and the two phase black oil model with geomechanics is applied to model the complex fracture networks in that reservoir. In this case, CVFE is chosen to be the discretization method and two-phase black oil model is chosen to be the physical model. Indeed, the geomechanical model is also coupled in the simulation. After all modules have been selected, a "driver"

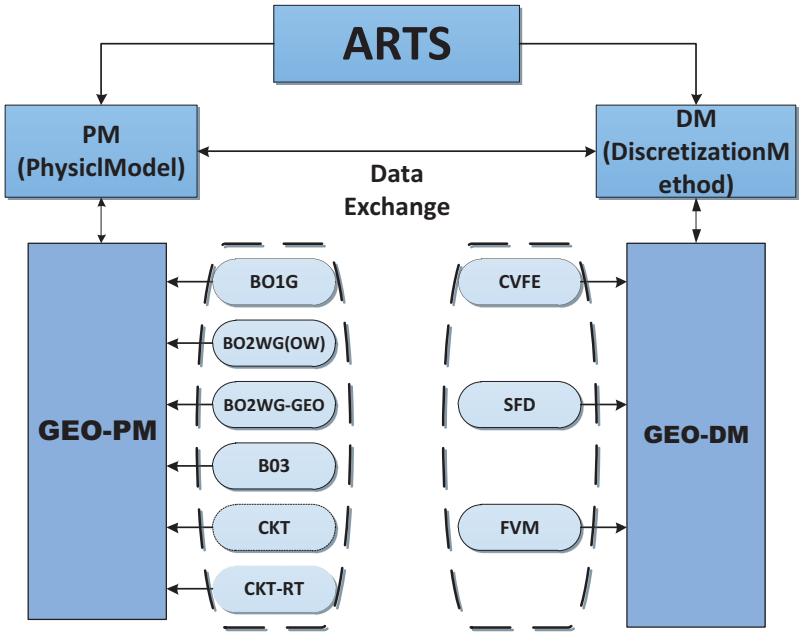

Figure 2.4: Flow chart of ARTS with geomechnaical module

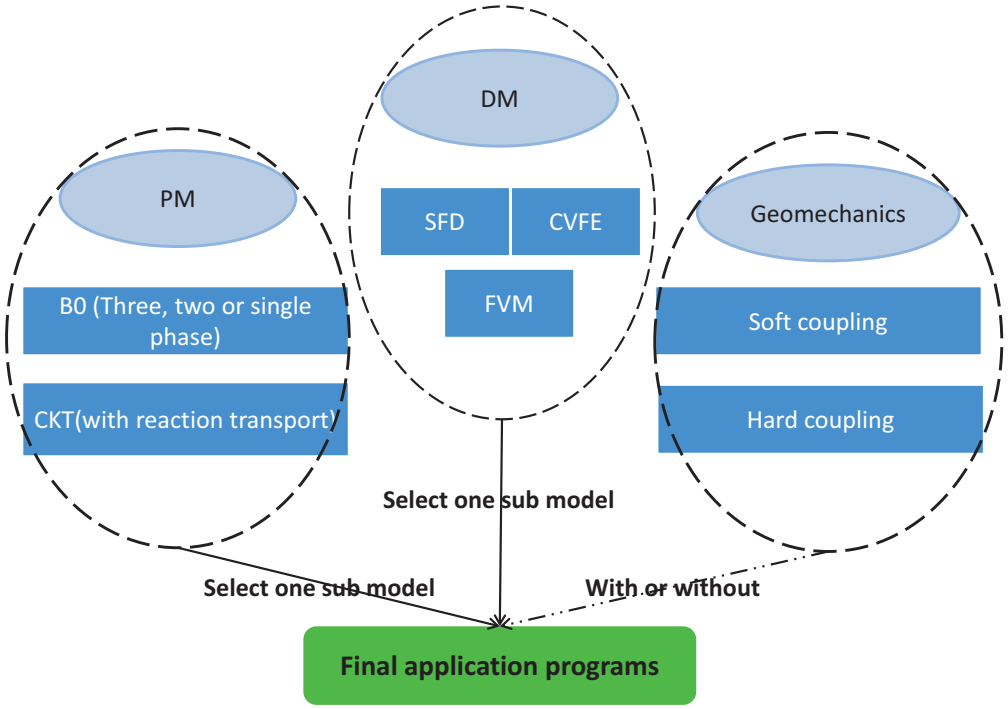

Figure 2.5: Flow chart of assembling an application program in ARTS

is implemented to generate the executable file for this particular application. The "driver" is just a few lines of code to call the selected modules. The whole process of building a new application in ARTS is fast if the modules needed already exist. If more models are needed in the future, it can be implemented by using the generic structure in ARTS and would work with other models properly. New application programs can be built following the same procedure with the help of SCONS.

2.2 Implementation of ARTS

C++ programming language, which is the best suited for general purpose programming, is applied to implement ARTS framework. The generalization and modularization design of ARTS fits the idea of object oriented program in C++. In the implementation, PM and DM in ARTS are the high level classes (base class) and the submodels are the lower level classes (derived class) and inherit some generic data structure from PM and DM. Virtual function has been used heavily in ARTS to achieve the goal of "one interface, multiple methods" [94]. For example the calculation of the accumulation terms is different in various submodels, but there is only one function (virtual function) implemented in PM or DM.

The reason for this is that specific methods of calculation accumulation terms are defined in the derived class and only one interface needs to be implemented in the base class. The geomechanical module is implemented in the same way.

In the PM module, several base classes is implemented. These classes are in charge of computing the spatial information independent terms and then assembling the final discrete governing equations, hence the solver can solve the linear system. Several important classes of PM and their major functionality are listed below:

1. PhysicalModel: main driver of the simulator, controls the whole process of the simulation
2. LineSource: calculate the source and sink term
3. Rock: calculate the rock properties like porosity
4. Fluid: calculate fluid properties like viscosity and volumetric factor
5. RockFluid: calculate the relative permeability term
6. NumericalMethod: interface for linear solver packages
7. State: store the basic variable values like pressure and saturation
8. ControlVolume: assemble the linear system
9. TimestepControl: control the time step for the simulation

The detail implementations of functions in each class listed above are varied in different inherited classes. For instance, the calculation of oil viscosity in thermal model is different from that in Black oil model, but these two functions are all derived from the fluid class in PM.

In the DM module, the base class is in charge of reading the basic geometry information and calculating the terms directly related to the discretization method. All the information calculated in DM will be passed to PM for the final assembling. DM also receives updated PM information if the base variables like pressure changes after calculation. The basic classes in DM are listed below:

1. DiscretizationMethod: read the geometry information and store it for further calculation

2. Element: calculate the spatial derivative terms

3. ControlVolume: calculate the volume and pass the derivative term to PM

4. LineSource: calculate the well index and the pressure drop

5. Object: handle the connection information between blocks

Several DM modules are also implemented in detail based on the classes listed above. The method applied is still virtual function and class inheritance in C++. In order to share information more easily between DM and PM, some classes such as control volume are designed to be public in PM and DM. The fracture representation methods built in DM have some unique functions instead of specific implementation of virtual functions in the based class. Otherwise, the basic implementation methods applied in DM are the same with PM. Figure 2.6 illustrates the implementation of a three-phase black oil model with CVFE as the discretization method.

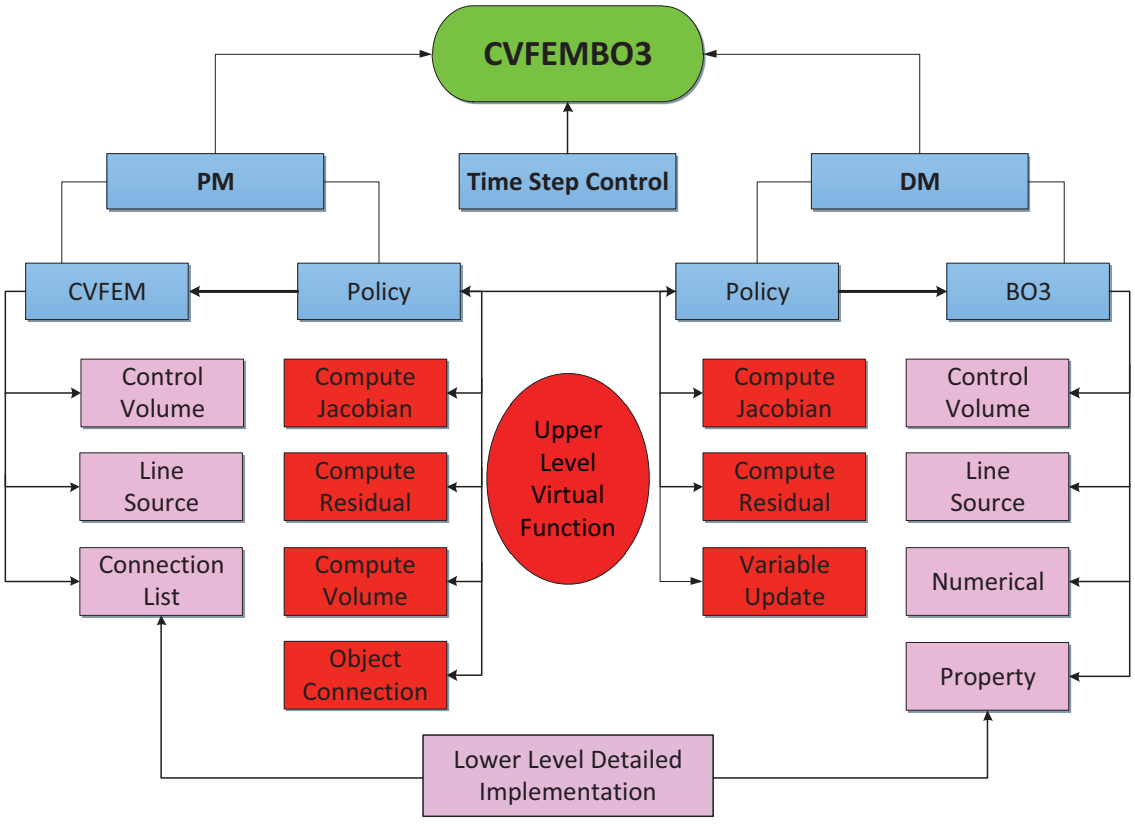

Figure 2.6: Flow chart of three-phase black oil model implementation

The geomechanical model is implemented in DM and PM as a friend class, it can directly use the information of PM and DM. The fracture representation method applied in geomechanical model is discrete fracture network, so most of the functions in DM can be reused. The control volume is created as a clone of control volume in PM and DM, all the information calculated in geomechanical model will be directly known by DM or PM. The controlling component of geomechanical coupling is implemented in PM. It is in charge of how and when the geomechanical model is communicated with PM or DM. Virtual functions and inheritance are also used to enhance the adaptability of geomechanical model.

The goal of developing a generalized reservoir simulation framework with specific applications has been reached through the generalization of governing equations and modularization design of ARTS. Object oriented programming, polymorphism and inheritance in C++ programming are heavily applied in ARTS to achieve the generalization and modularization. In this research, ARTS is developed with a generalized framework and further development can be easily done to add more potential functionality.

CHAPTER 3

GEOMECHANICAL MODEL

The mathematical formulations of the geomechanical model and how to solve it are discussed in this chapter. A classic finite element method is applied to solve the geomechanical equations, and various stress models like poroelastic and thermoelasticity are used. In order to couple geomechanics with other models, the soft and hard coupling schemes are used and these details are also discussed. With the model developed in this research, the geomechanical module is integrated in reservoir simulations and various field observations like subsidence, water loss and unexpected production decline or increase can be addressed.

3.1 Governing Equation

The governing equation system of ARTS includes two parts: one is the governing equation for the conventional reservoir model, and the other part is the governing equation for the geomechanical model.

3.1.1 Governing Equation of Geomechanical Model

The governing equations for the geomechanical model are based on force balance or momentum balance. Several assumptions are introduced first:

1. Infinitesimal strain theory:

$$\|\vec{u}\| \leq 1 \text{ and } \|\Delta u\| \leq 1$$

   (the norm of displacement and the displacement gradient are small compared to unity)

2. The solid velocity and acceleration is negligibly small.

3. The solid particle is impressible.

The first assumption allows the geometric linearization of the finite strain tensor. The material derivative is the same with the partial derivative based on the second assumption,

and the acceleration term is neglected in the momentum balance equation. Based on the third assumption, the density of the solid is a constant, even though properties of rocks are changing during the deformation process. With all these assumptions, the governing equation of geomechanical model can be described in the following form, in a representative elementary volume (REV):

$$\nabla \cdot \sigma + \vec{F} = 0 \tag{3.1}$$

where σ is a tensor which represents stresses (symmetric): $\sigma = \begin{bmatrix} \sigma_{x,x} & \sigma_{x,y} & \sigma_{x,z} \\ \sigma_{y,x} & \sigma_{y,y} & \sigma_{y,z} \\ \sigma_{z,x} & \sigma_{z,y} & \sigma_{z,z} \end{bmatrix}$.

If gravity is the only external force, then equation 3.1 is the same as equation 1.7 which is Biot consolidation equation. The full expression of the equation above is:

$$\begin{aligned} \frac{\partial \sigma_{xx}}{\partial x} + \frac{\partial \sigma_{yx}}{\partial y} + \frac{\partial \sigma_{zx}}{\partial z} + F_x = 0 \\ \frac{\partial \sigma_{xy}}{\partial x} + \frac{\partial \sigma_{yy}}{\partial y} + \frac{\partial \sigma_{zy}}{\partial z} + F_y = 0 \\ \frac{\partial \sigma_{xz}}{\partial x} + \frac{\partial \sigma_{yz}}{\partial y} + \frac{\partial \sigma_{zz}}{\partial z} + F_z = 0 \end{aligned} \tag{3.2}$$

Biot's effective stress model can be used to calculate the stress:

$$\sigma = \sigma' - \alpha \delta_{i,j} P_{avg} \tag{3.3}$$

where σ' is the effective stress,and P is the average pore pressure in the reservoir. In the saturation weighted form P_{avg} is:

$$P_{avg} = \sum_{p=1}^{n} S_p P_p \tag{3.4}$$

If gravity is assumed to be the only external force, equation 3.1 can be described by the

following:

$$\nabla \cdot (\sigma' - \alpha \delta_{i,j} P) + \rho_{avg} \vec{b} = 0 \tag{3.5}$$

The average reservoir density ρ_{avg} is defined as:

$$\rho = (1 - \phi^*)\rho_s + \phi^* \rho_f \tag{3.6}$$

where ρ_s is solid density in the reservoir (rock density). ρ_f is the fluid density in the reservoir. Saturation weighted fluid density may be applied to multiphase flow in the reservoir.

Different constitutive laws such as linear elasticity and poroelasticity can be applied to the stress term. The poroelasticity model reflects the stress response to the fluid flow movement, and it is accurate enough for modeling the stress change in the reservoir due to pore pressure variation. In this research, a linear poroelastic model is employed:

$$\sigma_{i,j} = 2G\varepsilon_{i,j} + 2G\frac{\nu}{1 - 2\nu}\varepsilon_{k,k}\delta_{i,j} - \alpha p \delta_{i,j} \tag{3.7}$$

where G is the shear modulus, ν is the Possion's ratio. The strain $\varepsilon_{i,j}$ is defined as:

$$\varepsilon_{ij} = \frac{1}{2}(\frac{\partial u_i}{x_j} + \frac{\partial u_j}{x_i}) \tag{3.8}$$

A linear thermal stress model is also applied in ARTS to couple with the thermal reservoir model. The linear thermoporoelasticity model can be expressed as the following formulation:

$$\sigma_{i,j} = \sigma^{'} - \alpha p \delta_{i,j} - 3\beta K_b T \tag{3.9}$$

where β is the linear thermal expansion coefficient. It describes how the solid deforms due to temperature change. The effective stress $\sigma^{'}$ can be expressed in poroelastic formulation (equation 3.7). In ARTS, the incremental formulation of equation 3.7 and 3.9 are used to facilitate the coupling process.

The geomechanics governing equation set uses vector variables. Deformation vector is usually the primary variable. The theory is based on a 3-D consolidation model, and

different stress models are implemented in the research. Indeed, the governing equations for geomechanics are expressed in various formulation to gain efficiency in different coupling schemes.

3.1.2 Governing Equations of Reservoir Model

In ARTS framework, various reservoir models are integrated. Isotherm and thermal models are the two major categories of phyisical models implemented in ARTS and the geomechanical model is designed for both of them.

In the latest version of the framework, the isotherm model includes single phase, two-phase and three-phase black oil models. The thermal model includes the CKT model and reactive transport model. The governing equation for black oil model is the material balance equation, and it can be described in the following formulation:

$$\nabla \cdot (\bar{\bar{\mathbf{K}}} \frac{kr_p}{B_p \mu_p} \nabla \varphi_p) = \frac{\partial}{\partial t}(\phi \frac{S_p}{B_p}) + q_p \tag{3.10}$$

where $\bar{\bar{\mathbf{K}}}$ is the absolute permeability tensor, kr_p is the relative permeability, S_p is the saturation, B_p is the volumetric factor, q_l is the source or the sink term, φ_p is the potential term. The fluid potential term can be described by the following equation:

$$\varphi_p = P + \gamma_p Z \tag{3.11}$$

Various models can be applied to the source and sink term. The well model for production and injection is also integrated into this term, and will be discussed later.

The governing equations for thermal model are the mass balance equation and the energy balance equation. For a system consisting of N_p phases, N_f fluid phases, N_c components, N_{req} chemical equilibrium reactions, and N_r kinetics control chemical reactions, the mass conservation equation for component i can be described as:

$$\begin{aligned} \frac{\partial \sum_{p=1}^{N_p}(\phi S_p \rho_p x_{p,i})}{\partial t} &= -\nabla \cdot (\sum_{p=1}^{N_f} x_{p,i} \rho_p \vec{v_p}) + \sum_{req=1}^{N_{req}} s_{req,i} \mathcal{R}_{req} \\ &+ \sum_{r=1}^{N_r} s_{r,i} \mathcal{R}_r + \sum_{p=1}^{N_f} x_{p,i} Q_p \end{aligned} \tag{3.12}$$

where $\vec{v}_p$ is computed by the following equation:

$$\vec{v}_p = \bar{\bar{\mathbf{K}}} \frac{kr_p}{\mu_p} \left(\nabla P_p + \gamma_p \nabla z\right) \tag{3.13}$$

$\mathcal{R}_{req}$ represents the chemical equilibrium reaction rate and $\mathcal{R}_r$ is the kinetics control chemical reaction rate. Aqueous phase reactions are assumed to reach equilibrium instantly, and the rates will be eliminated from the governing equations. The source or sink term $\sum_{p=1}^{Nf} x_{p,i} Q_p$ is attributed to wells or aquifers.

The energy balance equation is:

$$\frac{\partial (U_p + U_{rock})}{\partial t} = \nabla \cdot \bar{\bar{\mathbf{K}}}_{\mathbf{c}} \nabla T - \nabla \cdot (\sum_{p=1}^{Nf} \hat{H}_p \rho_p \vec{v}_p) + Q_e + Q_{loss} \tag{3.14}$$

where U_p and U_{rock} can be written as:

$$U_p = \sum_{p=1}^{Np} \phi S_p \rho_p \hat{U}_p \tag{3.15}$$

$$U_{rock} = (1-\phi) \bar{U}_{rock} \tag{3.16}$$

All the essential governing equations in the ARTS framework are discussed above. Several other constrain equations are needed to solve the system mathematically. These equations are listed below:

1. Saturation constrain: sum of all phase saturations is equal to one.

$$\sum_{p=1}^{Np} S_p - 1 = 0 \tag{3.17}$$

2. Molar fraction constraint: sum of mole fractions for all components in a phase is equal to one.

$$\sum_{i=1}^{Nc} x_{p,i} - 1 = 0 \tag{3.18}$$

3. N_e thermodynamic equilibrium constraint equations

$$\begin{aligned} R_{K_k} &= K_{p1-p2,i} \cdot x_{p2,i} - x_{p1,i} \\ p1, p2 &\in [1, N_p] \\ i &\in [1, N_c] \\ k &\in [1, N_e] \end{aligned} \tag{3.19}$$

The fast reaction is assumed to be in equilibrium in ARTS to improve the stability of the simulator.

$$R_{K_k} = f_{gas,i} - f_{aqu,i} \tag{3.20}$$

The fugacity $f_{gas,i}$ is calculated from the Peng-Robinson Equation of state. The fugacity $f_{aqu,i}$ of gaseous components soluble in aqueous phase is calculated using Henry's law as:

$$f_{gas,i} = x_{aqu,i} H_i \tag{3.21}$$

where Henry's law constant Hi is a function of temperature, pressure, and salinity.

The thermodynamics equilibrium constant $K_{gas-aqu,i}$ is calculated as:

$$K_{gas-aqu,i} = \frac{H_i}{\gamma_{gas,i} P} \tag{3.22}$$

The number of thermodynamic equilibrium constraints is determined by the number of equilibrium pairs in the component-phase matrix of the input file.

4. N_{req} chemical equilibrium constraint equations

$$R_{req} = \prod_{i=1}^{N_c} a_i^{s_{req,i}} - K_{req} \tag{3.23}$$

The activities a_i are related to the morality of m_i for component i ($mole/kgH_2O$) as follows:

$$a_i = \gamma_i m_i \tag{3.24}$$

With all the mathematical formulations listed above, the system can be solved with certain numerical methods. The geomechanical model can also be coupled to the reservoir model by using various coupling schemes and methods. All these methods are discussed in the following sections.

3.2 Numerical Methods

In this section, the numerical algorithms used to solve the governing equations are discussed. Control Volume Finite Element (CVFE), Finite Difference (FD) and Finite Volume Method (FVM) can be used as discretization methods in ARTS for the black oil and thermal model. Newton's method is used for solving the nonlinear algebraic equations. In order to couple geomechanics, several specific coupling schemes are also developed in ARTS.

3.2.1 Representative Element Volume

In a discretization scheme, the governing equations are applied over representative elementary volumes. The governing equation integrated over all the REVs is written as

follows:

$$\int_V (\nabla \cdot (\sigma' - \alpha \delta_{i,j} P) + \rho_{avg} \vec{b}) dV = 0 \tag{3.25}$$

The traction term $\vec{t}$ is defined as a surface force per unit area on the external surface of an REV. This traction term is obtained when the divergence theory is applied to equation 3.25. The incremental form of the governing equation is valid with the assumption of linear stress models.

Further evaluation of the integrated formulation of the governing equation requires appropriate matrix formulation. The stress tensor is represented as a vector format for convenience.

The total stress tensor σ can be formulated in to a 6×1 vector format $\vec{\sigma}$ by merging the symmetric off diagonal part:

$$\vec{\sigma} = \begin{bmatrix} \sigma_{xx} & \sigma_{yy} & \sigma_{zz} & \sigma_{xy} & \sigma_{yz} & \sigma_{zx} \end{bmatrix}^T \tag{3.26}$$

If we define:$\vec{\varepsilon} = \begin{bmatrix} \varepsilon_{xx} & \varepsilon_{yy} & \varepsilon_{zz} & \varepsilon_{xy} & \varepsilon_{yz} & \varepsilon_{zx} \end{bmatrix}^T$ and $\vec{m} = \begin{bmatrix} 1 & 1 & 1 & 0 & 0 & 0 \end{bmatrix}^T$ then the stress vector can be simplified further by applying the effective stress law:

$$\vec{\sigma} = D\vec{\varepsilon} - \alpha \vec{m} P \tag{3.27}$$

where D is the coefficient matrix of the stress-strain relationship. The choice of the D matrix depends on the stress model used. A linear poroelastical stress model with matrix D_l can be used, for example. This equation can also represent the thermal stress effect (linear or nonlinear) in practical thermal recovery processes by incorporating the thermal stress coefficient matrix D_T. The thermal stress model can be expressed in the following form:

$$\vec{\sigma} = D_T \vec{\varepsilon_T} + D\vec{\varepsilon} - \alpha \vec{m} P \tag{3.28}$$

In ARTS, an independent submodule is designed for switching the D matrix to provide a platform for considering other geomechanical effects (thermal stress, stress change due to

reaction) in the future. This module is also capable of incorporating nonlinear and other complex models.

3.2.2 Virtual Work Formulation of Geomechanical Model

Virtual work theory in computational mechanics can be applied for geomechanical computations. The solution of the virtual work formulation is the exact solution of the original equation theoretically. Based on this, the geomechanical governing equation is transformed to a virtual work formulation.

A general virtual work formulation can be derived for the geomechanical model: (The body force is neglected for convenience since it is only gravity force in most cases):

$$\int_{\Omega} \delta\vec{\varepsilon}^{T} \Delta\sigma' d\Omega - \alpha \int_{\Omega} \delta\vec{\varepsilon}^{T} \Delta p d\Omega - \int_{\Gamma_\sigma} \delta\vec{u}^{T} \Delta\vec{t} d\Gamma = 0 \tag{3.29}$$

where Γ_{sigma} is the surface of the arbitrary volume Ω. Substituting equation 3.27 in equation 3.29 and applying the basis function from FEM; the following is obtained:

$$(\int_{\Omega} B^{T} D B d\Omega)(\Delta\vec{u}) - \alpha(\int_{\Omega} B^{T} \vec{m} N d\Omega)(\Delta p) - \int_{\Gamma_\sigma} \delta\vec{u}^{T} \Delta\vec{t} d\Gamma = 0 \tag{3.30}$$

where u is the deformation vector inside the volume Ω. It can be written in the FEM type of formulation with the basis function N_i as the following (how to calculate N_i is discussed in chapter 4):

$$\vec{u} = \begin{bmatrix} N_1 & 0 & 0 & N_2 & 0 & 0 & N_3 & 0 & 0 & \dots \\ 0 & N_1 & 0 & 0 & N_2 & 0 & 0 & N_3 & 0 & \dots \\ 0 & 0 & N_1 & 0 & 0 & N_2 & 0 & 0 & N_3 & \dots \end{bmatrix} \begin{bmatrix} u_1 \\ v_1 \\ w_1 \\ u_2 \\ v_2 \\ w_2 \\ u_3 \\ v_3 \\ w_3 \\ \vdots \end{bmatrix} = N\vec{u^e} \tag{3.31}$$

B is the divergence matrix manipulator defined as: $B = [B_1, B_2, B_3, \dots, B_i]$. Each compo-

nent B_i is a matrix:

$$B_i = \begin{bmatrix} \frac{\partial N_i}{\partial x} & 0 & 0 \\ 0 & \frac{\partial N_i}{\partial y} & 0 \\ 0 & 0 & \frac{\partial N_i}{\partial z} \\ \frac{\partial N_i}{\partial y} & \frac{\partial N_i}{\partial x} & 0 \\ 0 & \frac{\partial N_i}{\partial z} & \frac{\partial N_i}{\partial y} \\ \frac{\partial N_i}{\partial z} & 0 & \frac{\partial N_i}{\partial x} \end{bmatrix} \tag{3.32}$$

Then the strain vector can be written in the following formulation:

$$\vec{\varepsilon} = \begin{bmatrix} \frac{\partial}{\partial x} & 0 & 0 \\ 0 & \frac{\partial}{\partial y} & 0 \\ 0 & 0 & \frac{\partial}{\partial z} \\ \frac{\partial}{\partial y} & \frac{\partial}{\partial x} & 0 \\ 0 & \frac{\partial}{\partial z} & \frac{\partial}{\partial y} \\ \frac{\partial}{\partial z} & 0 & \frac{\partial}{\partial x} \end{bmatrix} \begin{bmatrix} N_1 & 0 & 0 & N_2 & 0 & 0 & N_3 & 0 & 0 & \dots \\ 0 & N_1 & 0 & 0 & N_2 & 0 & 0 & N_3 & 0 & \dots \\ 0 & 0 & N_1 & 0 & 0 & N_2 & 0 & 0 & N_3 & \dots \end{bmatrix} (\vec{u^e}) = B(\vec{u^e}) \tag{3.33}$$

If we substitute equation 3.31 in equation 3.30 and express Δp in the FEM formulation, a linear system is formed: $A\Delta\vec{u^e} = \Delta B$. The linear system can be solved for the deformation vector by using appropriate linear solvers.

3.2.3 The Galerkin Method

The Galerkin method is widely used in FEM type numerical models. The geomechanical model can be simplified with the divergence theorem and the application of the Galerkin method. In order to demonstrate this procedure, the stress is defined as $\underline{\underline{\sigma}}$ and the external force is defined as $\underline{b}$. The original governing equation 3.1 can be written as:

$$\nabla\underline{\underline{\sigma}} + \underline{b} = 0 \tag{3.34}$$

By multiplying a "constant" displacement vector on both sides of the equation 3.34:

$$\vec{u}(\nabla\underline{\underline{\sigma}} + \underline{b}) = 0 \tag{3.35}$$

Rewriting the first term in equation 3.35 by applying the rule of integration, $\vec{u}\nabla\underline{\underline{\sigma}} = \nabla(\vec{u}\underline{\underline{\sigma}}) - \underline{\underline{\sigma}}\nabla\vec{u}$ is obtained. Integrating over the entire volume of one element (REV), the

following integration formulation can be derived:

$$\int_V (\nabla(\vec{u}\underline{\underline{\sigma}}) - \underline{\underline{\sigma}}\nabla\vec{u} + \vec{u}b)dV = 0 \tag{3.36}$$

Then we can apply the Gaussian-Green theory to the term $\int_V \nabla(\vec{u}\underline{\underline{\sigma}})dV$. Equation 3.36 can be written as the following (S is the surface area of the REV):

$$\oint_S \vec{u}\underline{\underline{\sigma}}\vec{n}dS - \int_V \underline{\underline{\sigma}}\nabla\vec{u}dV + \int_V \vec{u}bdV = 0 \tag{3.37}$$

Notice that $\underline{\underline{\sigma}}\nabla\vec{u}$ can be written as $\vec{u}S^T\vec{\sigma}$. where S^T is a 3×6 matrix:

$$S^T = \begin{bmatrix} \frac{\partial}{\partial x} & 0 & 0 & \frac{\partial}{\partial y} & 0 & \frac{\partial}{\partial z} \\ 0 & \frac{\partial}{\partial y} & 0 & \frac{\partial}{\partial x} & \frac{\partial}{\partial z} & 0 \\ 0 & 0 & \frac{\partial}{\partial z} & 0 & \frac{\partial}{\partial y} & \frac{\partial}{\partial x} \end{bmatrix} \tag{3.38}$$

Then equation 3.37 can be rewritten as:

$$\oint_S \vec{u}\underline{\underline{\sigma}}\vec{n}dS - \int_V \vec{u}S^T\underline{\underline{\sigma}}dV + \int_V \vec{u}bdV = 0 \tag{3.39}$$

If the "constant" displacement vector $\vec{u}$ is divided from both sides and the Galerkin weighted residual method is applied in equation 3.39 (basis function N^T is the weighting factor); the following is obtained:

$$\oint_S N^T\vec{t}dS - \int_V B^T\underline{\underline{\sigma}}dV + \int_V N^T\vec{b}dV = 0 \tag{3.40}$$

where $B^T = N^T S^T$ and u^e is the displacement for each node. Then the effective stress relationship and stress model can be applied to equation 3.40:

$$\oint_S N^T\vec{t} - \int_V B^T DBu^e + \int_V B^T\alpha\vec{m}\vec{p} + \int_V N^T\vec{b} = 0 \tag{3.41}$$

Finally, $\vec{t}$, $\vec{p}$, can be expressed in the FEM formulation and equation 3.41 can be written

as the final discrete formulation:

$$\oint_S N^T N t^e - \int_V B^T D B u^e + \int_V B^T \alpha \vec{m} N p^e + \int_V N^T N b^e = 0 \tag{3.42}$$

Equation 3.42 is constructed for just one REV. Similarly, the entire equation system can be assembled through the element by element assembling process. Based on the choice of basis function and algorithm, the calculation of each term in equation 3.42 may be different.

The surface traction term is calculated only at the boundary. The traction terms for two connected element are cancelled out in the assembling procedure. If B and D are assumed to be independent of the location, then terms related to B and D can be taken out of the volume integration term. For the calculation of the integration terms, certain types of Gaussian quadrature can be applied. Finally a linear system is constructed for the whole reservoir system, and the displacement of each node can be obtained from the geomechanical model with the correct set of initial and boundary conditions.

3.2.4 Boundary and Initial Conditions

Appropriate boundary and initial conditions are essential for solving the entire reservoir governing equation set. The initial condition module in the framework is to set initial values for pressure, saturation, displacement and other primary variables for the entire reservoir system. In addition, the initial stress field is crucial to the geomechanical model. The initial condition setting should follow some reference or practical measurement in the field. The traction term or displacement needs to be specified on the boundary. This is important for a reasonable result of the displacement. In ARTS, an individual class is used for the management of boundary conditions (degrees of freedom) under the geomechanical module.

There are generally two types of boundary conditions involved in the geomechanical formulation. One is called forced or geometric or essential boundary condition, and the other is called natural or free boundary condition. The natural boundary condition is already incorporated in the virtual formulation of geomechanical model when the traction term is calculated. The geometric boundary condition needs to be satisfied in the solving procedure. In the geomechanical model of ARTS, the stress or force condition is considered as the first type of boundary condition and the other conditions, like predefined deformation, is considered as the second type. The detail of how to incorporate these boundary conditions is discussed in the following sections.

Initially, the reservoir is assumed to be at the static state which means the force balance is valid. Hence, the initial deformation in the reservoir (u_0) is euqal to the deformation at the equilibrium conditon (u_eq). The boundary and initial conditions can be summarized in the following formulation (assuming Ω_r is the domain of a deformable reservoir, and Γ_s is the boundary of the domain):
The initial condition:

$$u = u_0 \text{ in } \Omega_r \tag{3.43}$$

If the incremental formulation is used, then the values of u_0 are not used in the simulation. The boundary condition:

$$\begin{aligned} u &= u_{bc} \text{ on } \Gamma_u \\ \sigma \cdot \vec{n} &= \vec{t} \quad \text{on } \Gamma_\sigma \end{aligned} \tag{3.44}$$

where $\Gamma_s = \Gamma_u + \Gamma_\sigma$, and Γ_u and Γ_σ represent the surfaces have fixed displacement boundary and fixed stress boundary. $\vec{n}$ is the unit normal vector of the boundary surface.

3.3 Geomechanical Coupling

After construction of the discrete formulations of the geomechanical model and the reservoir model, specific coupling schemes are to be employed to solve the entire coupled problem. In general, there are two types of coupling schemes in the research work: soft coupling and hard coupling. Soft coupling means the geomechanical model is not directly integrated and solved in the reservoir simulation framework. Hard coupling method integrates the geomechanical model in the reservoir simulator with a specific coupling scheme. Both methods are implemented in ARTS.

In addition to the coupling scheme, certain coupling parameters are needed as a connection between the two models. Usually, the geomechanical effect on the reservoir is due to the change of permeability and porosity. As a result, permeability and porosity introduce the geomechanical effect into the reservoir model. For the geomechanical model, the pore pressure and temperature change will influence the force balance and change the displacement field. So the pore pressure and temperature change in the reservoir have an impact on the geomechanical model.

3.3.1 Coupling Parameters

Porosity is related to the displacement or other geomechanical variables by performing the mass balance for the rock. The permeability is related to the geomechanical properties through the porosity permeability relationship. The continuity or mass balance equation for solid media in the reservoir is:

$$\frac{\partial \dot{\rho_s}}{\partial t} + \nabla(\dot{\rho_s} v_s) = 0 \tag{3.45}$$

where $\dot{\rho_s}$ is the real solid density, v_s is the solid velocity. Substituting $\dot{\rho_s} = \rho_s(1-\phi)$ and $\nabla v_s = \frac{d\varepsilon_v}{dt}$ in equation 3.45, the following equation can be derived:

$$\frac{\partial \rho_s(1-\phi)}{\partial t} + \nabla((1-\phi)v_s) = 0 \tag{3.46}$$

The above is integrated to relate porosity and strain (ϕ_0 is initial reservoir permeability):

$$\phi^* = 1 - (1-\phi_0)e^{-\varepsilon_v} \tag{3.47}$$

Equation 3.47 can be linearized by assuming a small strain:

$$\phi = (\frac{1-\phi_0}{1-\phi^*})\phi^* \tag{3.48}$$

Permeability can be related to the geomechanics factor with the following equation:

$$\frac{k}{k_0} = \frac{1 + \frac{\varepsilon_v}{\phi_0}}{1+\varepsilon_v} \tag{3.49}$$

where $\varepsilon_v = \frac{\delta V}{V} = \varepsilon_{xx} + \varepsilon_{yy} + \varepsilon_{zz}$, and k_0 is the initial permeability of the reservoir. Through these equations above, the impact of geomechanics is introduced into the reservoir model.

On the other hand, the pore pressure and saturation (temperature) change can influence the geomechanical force balance through the effective stress equation. The geomechanical model and the reservoir model are connected through these theoretical formulations. Based on the coupling parameters and the equations described above, different coupling schemes can be applied.

3.3.2 Soft Coupling

The geomechanical effect is implemented in reservoir simulation by using updated porosity and permeability fields. The permeabilities and porosities are assigned as functions of pressure and saturation, and are updated using an external geomechanical model. This information could come from field data or from real simulations. Take the geomechanical model with a poroelastic constitutive relationship as an example. The original permeability and porosity are described in the following equations:

$$\begin{aligned} k &= K_{org}(1 + DK) \\ \phi &= \phi_{org}(1 + Dphi) \end{aligned} \tag{3.50}$$

where K_{org} and ϕ_{org} are the original permeability and porosity calculated by the reservoir model, Dk and $Dphi$ are the parameters that represent the permeability and porosity increase related to the geomechanical model, and are obtained through external geomechanical packages.

A soft coupling scheme is developed based on the Itasca 3DEC geomechanical simulator in ARTS. The geomechanical software 3DEC provides the information of fracture aperture change versus the pore pressure. Then, a look-up table is introduced in ARTS for calculating the additional permeability and porosity (Dk and $Dphi$) changes based on the information provided by 3DEC. Cubic law [95, 96] is employed to perform the calculation of permeability change in the fracture. The same geometry is used in both simulations, and this is a restriction of this coupling scheme. The scheme costs a little more computational time compared with the uncoupled simulation, and the importance of geomechanical changes on the recovery processes can be understood in this manner. Figure 3.1 shows the coupling procedure of this method.

This method is just an approximation of the geomechanical effect in the reservoir model, as it assumes that the fracture aperture in the coupled system is similar to the result that comes from 3DEC. However, this is a fast study tool for understanding how the geomechanical model influences the reservoir behavior. This scheme is also adaptable to work with most reservoir models with little change in the source code. Some results of this method are discussed in Chapter 6.

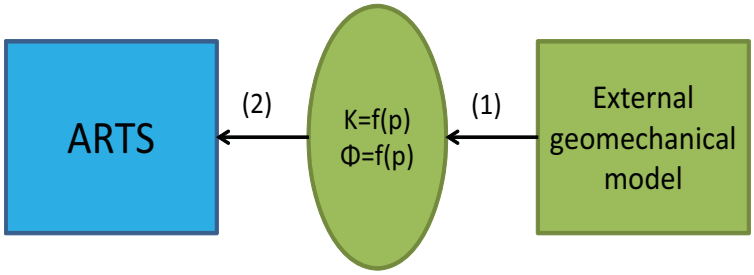

Figure 3.1: Soft coupling scheme in ARTS

3.3.3 Hard Coupling

If the geomechanical model is integrated in the reservoir simulator, it is called hard coupling. The geomechanical equation set and conventional reservoir simulation equation set are solved either "separately" or "together" depending on the complexity of the problem. In ARTS, an individual geomechanical module is integrated for performing the hard coupling scheme. The geomechanical module is divided into two parts in the framework. One part is coupled with DM and the other part is coupled with PM. Different hard coupling schemes such as iterative coupling are implemented. This method is designed to work with all potential reservoir models in ARTS with little modification in the source code of the reservoir model. The basic flow chart of this coupling scheme is described in Figure 3.2.

In order to perform different coupling schemes, the governing system of conventional reservoir simulation is modified to introduce the geomechanical variables. The original mass balance equation for the fluid flow in porous media in equation 3.10 can be written as:

$$-\nabla \cdot \frac{\vec{v_l}}{B_l} = \frac{\partial}{\partial t}(\phi^* \frac{S_l}{B_l}) + q_l \tag{3.51}$$

where v_l is the fluid velocity in the porous media. If the velocity of the rock is considered, the fluid velocity needs to be modified as the relative velocity with respect to the solid velocity:

$$\vec{v_{ls}} = \vec{v_l} - \vec{v_s} \tag{3.52}$$

Then equation 3.51 becomes:

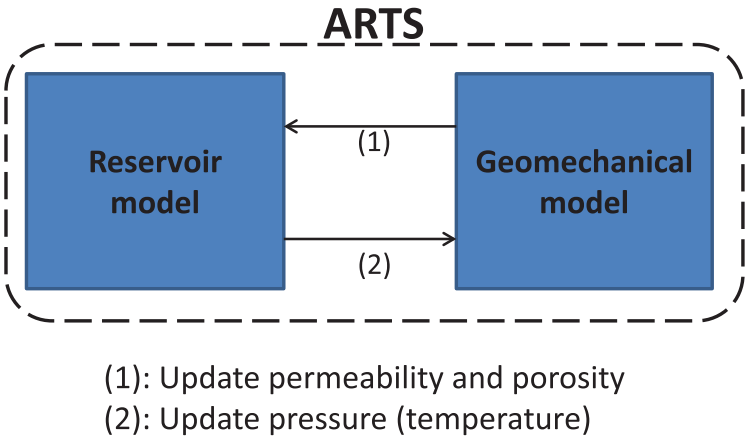

Figure 3.2: Basic flow chart of hard coupling scheme in ARTS

$$\begin{aligned} -\nabla \cdot \frac{\vec{v_l} - \vec{v_s}}{B_l} &= \frac{\partial}{\partial t}(\phi^* \frac{S_l}{B_l}) + q_l \\ -\nabla \cdot \frac{\vec{v_l}}{B_l} + \nabla \cdot \frac{\vec{v_s}}{B_l} &= \frac{\partial}{\partial t}(\phi^* \frac{S_l}{B_l}) + q_l \end{aligned} \tag{3.53}$$

The definition of solid velocity in the reservoir is:

$$\nabla \cdot \vec{v_s} = \nabla \cdot \frac{D\vec{u_s}}{Dt} = \frac{D(\nabla \cdot \vec{u_s})}{Dt} = \frac{D\varepsilon_v}{Dt} \tag{3.54}$$

By substituting equation 3.54 in equation 3.53, and by applying Darcy's law, the following equation is derived:

$$\nabla \cdot (\frac{\bar{\bar{\mathbf{K}}} k_{rl}}{B_l \mu_l} \nabla \varphi_l) + \frac{D}{Dt}(\frac{\varepsilon_v}{B_l}) = \frac{\partial}{\partial t}(\phi^* \frac{S_l}{B_l}) + q_l \tag{3.55}$$

The above equation is the modified mass balance equation of the black oil model, and it includes the geomechanical variables for the coupling with the geomechanical model. Another accumulation term is added to introduce the geomechanical effect. The modification of other models follows the same idea. If a solid continuity equation is applied, the following

assumption can be made: $\frac{D}{Dt}(\frac{\varepsilon_v}{B_l}) \approx \frac{\partial}{\partial t}(\frac{\varepsilon_v}{B_l})$. Then equation 3.55 can be written as:

$$\nabla \cdot (\frac{\bar{\bar{\mathbf{K}}} k_{rl}}{B_l \mu_l} \nabla \varphi_l) + \frac{\partial}{\partial t}(\frac{\varepsilon_v}{B_l}) = \frac{\partial}{\partial t}(\phi^* \frac{S_l}{B_l}) + q_l \tag{3.56}$$

The energy balance equation can apply the same method and the true porosity and the updated permeability can be used. The modified governing equations, together with the geomechanical governing equation, are basic to applying the hard coupling scheme.

3.4 Linear Solver

After Newton's method is applied, the reservoir models can be represented by a Jacobian system of the form:

$$-\vec{R} = \left[\frac{\partial R}{\partial Y}\right] \delta \vec{Y} \tag{3.57}$$

where $\vec{R}$ and $\vec{Y}$ are the residual and solution vector. $J = \dfrac{\partial R}{\partial Y}$ is the Jacobian matrix. The final form of the geomechanical model can be represented in the following formulation:

$$\vec{b} = K\vec{u} \tag{3.58}$$

where K is the global stiffness matrix, $\vec{b}$ is the global force load vector, and $\vec{u}$ is the deformation vector. Equations 3.57 and 3.58 can be solved either by using a direct solver or an iterative solver.

The direct method typically uses variations on Gaussian elimination. It is robust and reliable in most scenarios. Hence, it is widely implemented in many numerical packages like LAPACK [97]. A number of linear systems can be solved by this method with a reasonable computational effort.

There are a number of iterative methods for solving a linear equation. For example, Jacobi, Gauss-Seidel and SOR are called stationary methods and have been widely applied in many simulators. These methods are simple to derive and implement, but convergence is guaranteed only for a limited class of matrixes [98]. In modern simulators, Krylov space methods (for example, CG, BICG, GMRES, ORTHOMIN, BiCBSTAB, etc.) are widely implemented and applied. These methods work by forming a basis of the sequence of successive matrix times the initial residual (the Krylov sequence), and the approximations

to the solution are formed by minimizing the residual over the subspace formed. The convergence is somehow guaranteed, but it still depends on the size of the linear system [99].

For a linear system $\bar{\bar{A}}\vec{X} = \vec{B}$, the Krylov space at k^{th} iteration is defined as $\mathcal{K}^k = \mathbf{span}(\vec{B}, \bar{\bar{A}}\vec{B}^0, ..., \bar{\bar{A}}^{k-1}\vec{B}^0)$, where $B^0 = \bar{\bar{A}}\vec{B}^0 - \vec{B}$. Krylov subspace methods obtain the new solution by [100]:

$$\vec{X}_{k+1} = \vec{X}_k + \omega_k \vec{\mathrm{d}}_k \tag{3.59}$$

where ω_k is called the "step length" and $\vec{\mathrm{d}}_k$ is the "search direction." Different Krylov subspace algorithms have various ways of constructing these two parameters. In general, the number of iterations can be estimated by the following:

$$k \geq c\sqrt{\mathbf{cond}(\bar{\bar{\mathbf{A}}})} ln\frac{2}{\epsilon} \tag{3.60}$$

where **cond** is the condition number of the system, and ϵ is the tolerance of the iteration.

Gaussian elimination is applied in solving the CKT model. It is considered as a $\mathcal{O}(N^3)$ algorithm [101]. The number of iterations k is determined by the tolerance ϵ and a method-related constant c [102],

$$\mathrm{k} \geq \frac{-ln\epsilon}{\mathrm{c}} \tag{3.61}$$

Preconditioner is applied in solving the linear system. For example, GMRES is applied to solve the black oil governing equations in this research and a preconditioner that is generated by ILU factorization is applied. The method is proven to be effective and fast when applied to a number of case studies. Some preconditioners based on physics [103] have been applied to reservoir simulation, and have proven to be more effective than traditional methods.

Krylov subspace methods obtained from external libraries are used exclusively for solving the linear systems in this research. Two powerful numerical packages, Trilinos from Sandia

National Laboratory [104, 105], and PETSc from Argonne National Laboratory [106], are applied in ARTS. Only the linear solver parts of these two packages are used, and the parallel computational functions are built inside the solver. For instance, Aztec00 and KSPsolve have been used in ARTS, and MPICH2 [107] is applied to solve the linear system with parallel computation.

3.5 Solving Procedure

In order to solve the governing equations in a accurate and fast way, center solving procedure is designed in ARTS (Figure 3.3). First, before the solving procedure begins, the geomechanical model will or will not be initialized depend on the modeling requirements. After that, other reservoir models are initialized and the input information is taken in different modules. Then, various solving sequences can be applied depending on which models are used and which coupling scheme is applied. Once all the input information is transported to the framework, the calculation process starts.

During the calculation process, the whole system is written in the discrete formulation which will be discussed in Chapter 4. Newton's method is applied to linearize the system and then the global linear system is assembled. Finally, the linear system is solved by using the method discussed in section 3.4. Figure 3.3 shows the work flow of solving the governing equation system.

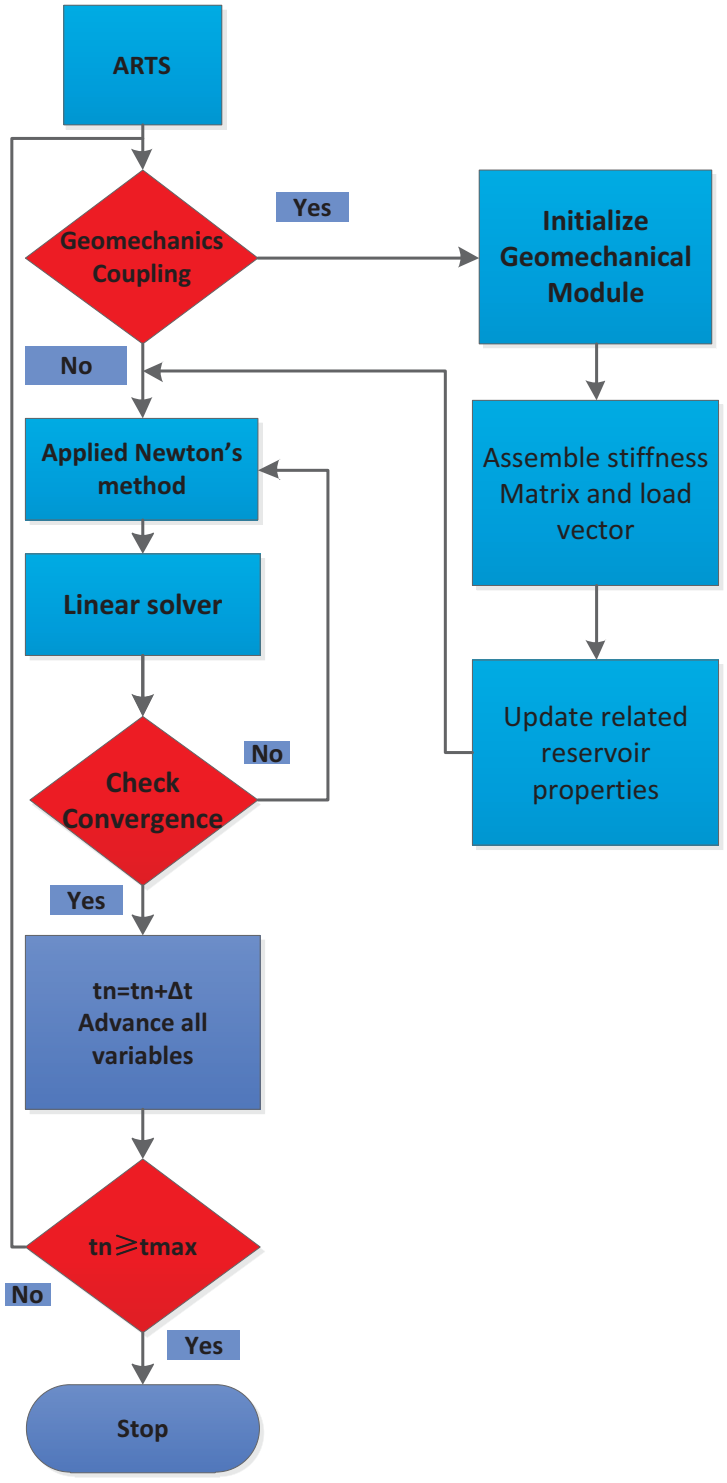

Figure 3.3: Basic flow chart of solving procedure in ARTS

CHAPTER 4

DISCRETIZATION METHOD

As mentioned in the last chapter, the partial differential equations need to be solved by using the discretization formulation. Different temporal and spatial discretization methods are applied in this research to achieve the goal of multiple purpoese reservior simulation. Regular first order method is applied to do temporal discretization. For spatial discretization, serveral different methods have been applied in ARTS:

1. Control Volume Finite Element Method (CVFEM)
2. Finite element method
3. Standard two-point finite difference method
4. Corner-pointer finite difference method

A general finite volume method is also applied [85, 86], and this method enables ARTS to work with arbitrary geometry input from other commercial simulators. In this chapter, the CVFE (Control Volume Finite Volume) discretization method and the concept of transmissibility is introduced first. The discrete fracture model associated with CVFE method is also discussed. Finally, other discrete methods used in ARTS are discussed in general.

4.1 Control Volume Finite Element Method

The CVFE method, which is developed by Yang and Yao [91], is implemented in ARTS framework. In 3-D, the reservoir domain is discretized into numerous tetrahedral elements. The tetrahedral elements represent the matrix, and the surface of the tetrahedron represents fractures. The concept of transmissibility is also introduced and defined in the framework.

In the CVFE discretization method, a tetrahedral element is divided into four parts: $\mathbb{CV}_1(\Omega_{E,1})$, $\mathbb{CV}_2(\Omega_{E,2})$, $\mathbb{CV}_3(\Omega_{E,3})$,and $\mathbb{CV}_4(\Omega_{E,4})$ (shown in Figure 4.1).

$$\sum_{i=1}^{4} \Omega_i = \Omega_E \tag{4.1}$$

Point o is the center point of the element. Within a tetrahedral element, $\mathbb{CV}_i(\Omega_{E,i})$ called a subcontrol volume of the control volume CV_i. The sum of all subcontrol volumes that surround the vertex i is called the control volume associates with the vertex i. Hence, each tetrahedron element is composed of four subcontrol volumes which belong to four different control volumes. The flux between each two subcontrol volumes is calculated using the general transmissibility, which is based on the finite volume method. The transmissibility can be generally expressed as:

$$T_{i,I,J} = \bar{\bar{\boldsymbol{k}}} \nabla \mathcal{N}_i \cdot \vec{n}_{I,J} A_{I,J} \tag{4.2}$$

where $\bar{\bar{\boldsymbol{k}}}$ is the permeability tensor, $\mathcal{N}_i$ is a discretization related parameter. The detail of

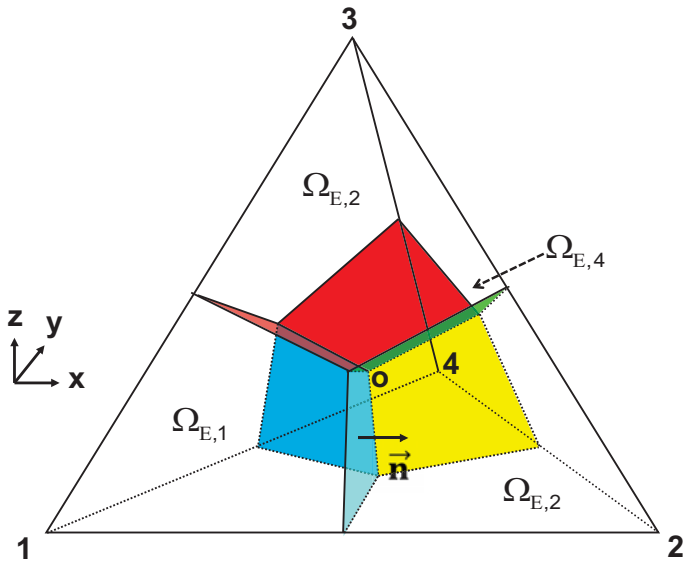

Figure 4.1: A schematic illustration of a tetrahedral element in CVFE method.

how to define and calculate the transmissibility for CVFE method is discussed in the next section.

4.1.1 Transmissibility Definition

The concept of transmissibility based on flow calculation [108, 109] has been developed in several reservoir simulators which used the finite difference method, such as Eclipse, CMG and Nexus. The transmissibility between two connected control volumes is computed in advance by using geometrical information, absolute permeability, and net to gross ratio of these two control volumes. After that, all transmissibilities and connection information is stored and passed to the simulator during the flux calculation. In ARTS, this concept is extended to model complex geometry with finite element discretization methods such as the CVFE with discrete fracture model. The flux of phase p between control volumes $\mathbb{CV}_I$ and $\mathbb{CV}_J$ can be expressed as:

$$F_{p,I,J} = m_p \vec{f} \cdot \vec{n_{I,J}} A_{I,J} \tag{4.3}$$

where $m_p = \dfrac{k_{rp}}{\mu_p}$ is the mobility term of phase p, $A_{I,J}$ is the surface area of boundary $\Gamma_{I,J}$, and $\vec{n_{I,J}}$ is the normal vector of $\Gamma_{I,J}$. If a linear basis or interpolation function is used for element Ω_E which contains N_v nodes for the finite element method, the potential (Φ) can be expressed by $\Phi = \sum_{i=1}^{N_V} \alpha_i \Phi_i$. This is also valid for modeling any finite region that contains two connected control volumes in the finite difference method. Hence, $\vec{f}$ can be expressed as:

$$\vec{f} = \bar{\bar{\boldsymbol{k}}} \nabla \Phi_i = \bar{\bar{\boldsymbol{k}}} \sum_{i=1}^{N_V} \nabla \alpha_i \Phi_i \tag{4.4}$$

The transmissibility $T_{i,I,J}$ between two finite volumes $\Omega_{E,I}$ and $\Omega_{E,J}$ is defined as:

$$T_{i,I,J} = \bar{\bar{\boldsymbol{k}}} \nabla \alpha_i \cdot \vec{n_{I,J}} A_{I,J} \tag{4.5}$$

Then the flux of phase p between finite volumes $\mathbb{CV}_I$ and $\mathbb{CV}_J$ can be expressed in the

following simplified formulation:

$$F_{P,I,J} = m_p \sum_{i=1}^{N_v} T_{i,I,J} \phi_{p,i} \tag{4.6}$$

$T_{i,I,J}$ in equation (4.6) only depends on discretization method, the geometry of the domain and absolute permeability. Therefore, it can be computed in advance and stored before the major reservoir simulation process. Different discretization methods can be implemented using this transmissibility concept and are discussed in the following sections.

4.1.2 Mobility Term and Upstream Weighting

In general, the flux of phase p is calculated using the equation 4.6 and the mobility term m_p is defined as:

$$m_p = \frac{k_{r,p}}{\mu_p} \tag{4.7}$$

where K_{rp} is the relative permeability of phase p. The mobility term that is not related to discretization method is calculated in PM.

Upstream weighting method was developed by Yang to keep the flux across the interface area between two subcontrol volumes continuous. This method also ensure the local mass balance in the system. The upstream condition can be decided by:

$$\begin{aligned} m_p &= m_{p,I} \quad \text{if} \quad \nabla\Phi \cdot \vec{n}_{I,J} A_{I,J} \geqslant 0 \\ m_p &= m_{p,J} \quad \text{if} \quad \nabla\Phi \cdot \vec{n}_{I,J} A_{I,J} \leqslant 0 \end{aligned} \tag{4.8}$$

This means if the flux term is form control volume I to J, all the properties used in flux calculation should come from the upstream control volume I.

4.1.3 Transmissibility Calculation

If certain discretization methods are used to obtain $\mathcal{N}$ and other parameters in the equation 4.2, the transmissibility term $T_{i,I,J}$ in CVFE method, can be expressed as:

$$T_{i,I,J} = \left(\begin{bmatrix} k_{xx} & k_{xy} & k_{xz} \\ k_{yx} & k_{yy} & k_{yz} \\ k_{zx} & k_{zy} & k_{zz} \end{bmatrix} \cdot \begin{Bmatrix} \frac{\partial \mathcal{N}_i}{\partial x} \\ \frac{\partial \mathcal{N}_i}{\partial y} \\ \frac{\partial \mathcal{N}_i}{\partial z} \end{Bmatrix} \right)^T \cdot \begin{Bmatrix} n_x \\ n_y \\ n_z \end{Bmatrix} A_{I,J} \tag{4.9}$$

All the parameters listed in equation 4.9 can be calculated based on finite element discretization method. This is introduced in section 4.2.

4.1.4 Fracture Model

As discussed in Chapter 1, three methods, single porosity model, dual porosity model and discrete fracture model, are commonly used for fracture modeling in reservoir simulation [110]. The single porosity model represents fracture in an explicit way and no special formulation is needed for calculating the flux term, to or from the fracture. In the dual porosity model, the fracture is treated differently and has its own porosity and permeability. The detail of this model is already discussed in Chapter 1, and the flux term can also be calculated using the transmissibility concept by the following equation in a finite difference method:

$$\begin{aligned} F_{p,I,J} &= m_p(T_{i,I,J}\Phi_{p,i} + T_{j,I,J}\Phi_{p,j}) \\ T_{j,I,J} &= -T_{i,I,J} \end{aligned} \tag{4.10}$$

where $\Phi_{p,i}$ is the potential term of phase p in control volume I.

In order to calculate the flux term between fracture and matrix, a special transmissibility is defined. Several methods have been used to derive this special transmissibility such as the Warren and Root formulation (equation 4.11), and the Gilman and Kazemi formulation (4.12).

$$T_{M,F} = \frac{20}{3} k_m \left(\left(\frac{1}{L_x} + \frac{1}{L_y} + \frac{1}{L_z} \right)^2 \right) V_{matrix} \tag{4.11}$$

$$T_{M,F} = 4k_m \left(\frac{1}{L_x^2} + \frac{1}{L_y^2} + \frac{1}{L_z^2} \right) V_{matrix} \tag{4.12}$$

where k_m is the permeability of the matrix and V_{matrix} is the total matrix volume. L_x, L_y, and L_z are the fracture spacings in x, y, and z directions.

The single porosity and dual fracture models are not directly coupled in ARTS in this research due to the limitation of modeling complex fracture geometry. Instead, the discretization fracture model with CVFE method is the default fracture model in ARTS.

As discussed in Chapter 1, the discrete fracture model is based on the concept of cross-flow equilibrium between the fluid in the fractured node and the fluid in the matrix node connected to the fracture. The dimensionality of fractures is reduced from n to $n-1$ in this model. The discrete fracture model offers several advantages:

1. It greatly reduces the complexity of the geometry and hence the computational time
2. It models the fracture impact on fluid flow explicitly
3. No shape function is needed to calculate fluid flow between fracture and matrix

The discrete fracture model can be applied in both the Finite Difference and Finite Element methods. In ARTS, the discrete fracture model is coupled with CVFE method to model complex fracture networks existing in reservoirs. There are several ways to represent fractures in the CVFE method based on discrete fracture models such as Fu's method and Monteagudo's method.

For a reservoir domain $\Omega = \Omega_m + \Omega_f$, the matrix formation is discretized by tetrahedrons and the fracture network is represented by triangle elements along the faces of the tetrahedral matrix elements. Figure 4.2 illustrates three common methods to represent fractures in a discrete fracture model.

- **Fu's method:**

  The fracture representation method in Figure 4.2a, was introduced by Fu et al. (2007) [83]. The basis of this method is property sharing between matrix and fracture at the fracture nodes (A, B and C in Figure 4.2a). This means the fracture nodes will have the same properties with corresponding matrix nodes. However, a different rock and rock-fluid property may be applied for the fracture, like relative permeability curve, capillary pressure curve or absolute permeability. In this research, the fractures have no storage and only provide the flow channels for reservoir fluids. Hence, an additional flow term is introduced into the mass conservation equations to represent the fluid flow contributed by fractures.

- **Monteagudo's method**

  The fracture representation method in Figure 4.2b was first introduced by Monteagudo

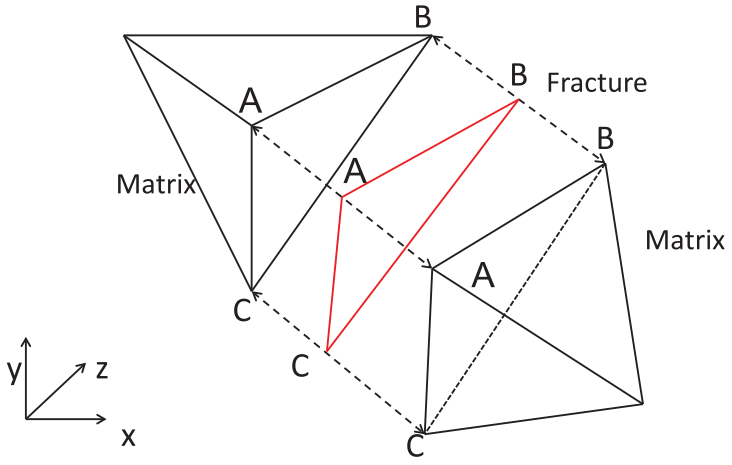

(a) Discrete fracture representation method 1

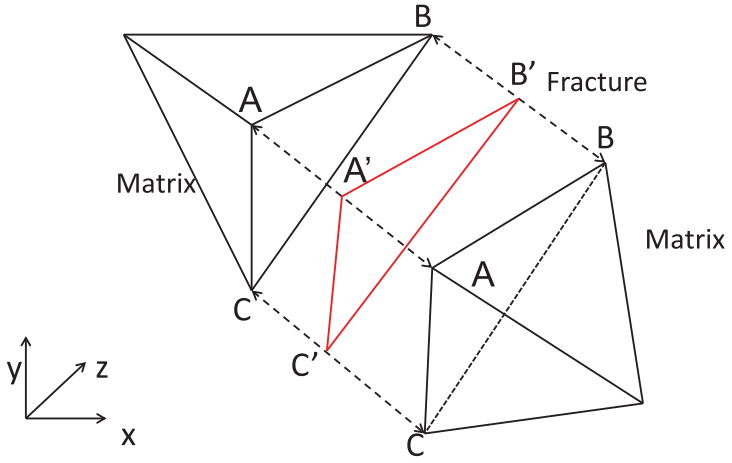

(b) Discrete fracture representation method 2

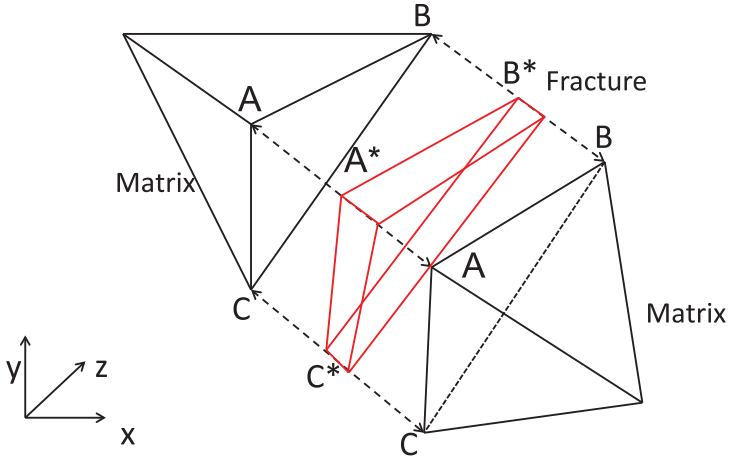

(c) Discrete fracture representation method 3

Figure 4.2: Possible representations of fractures in CVFEM-based discrete fracture models

et al. (2007) [111]. In this method, the nodes represent when the fracture element is separated from the corresponding matrix nodes, and two sets of different properties are assigned to the matrix and fracture. Some models were developed to relate to the pressures and saturations between fracture and the corresponding matrix. This method is somehow similar to the dual porosity model as the fracture and matrix are modeled differently. The cross-flow equilibrium concept is introduced to calculate the flow term between the matrix and fractures. However, this method is not implemented with compositional models yet.

- **Combined method**

  The fracture representation method in Figure 4.2c is to combine the first and the second methods. The fracture nodes and corresponding matrix nodes share properties, but the fracture also works as a storage of gas and oil, besides an additional fluid flow channel. An additional accumulation term is needed to add in the mass balance equation in this method.

4.1.5 Transmissibility of Fractures

The fracture is modeled as a 2-D triangular element in CVFEM based discrete fracture model as shown in Figure 4.3, the fracture flow term can be expressed in following equation:

$$F^f_{I,J} = m^f_p \sum_{i=1}^{3} T^f_{i,I,J} \Phi_i \tag{4.13}$$

and the fracture transmissibility $T^f_{i,I,J}$ can be calculated by:

$$T^f_{i,I,J} = \bar{\bar{\boldsymbol{k}}}_f \nabla \alpha^f_i \cdot \vec{n}^f_{I,J} A^f_{I,J} \tag{4.14}$$

where $\vec{n}^f_{I,J}$ is the normal vector and $A^f_{I,J}$ is the area of the fracture element. Certain interpolation models can be applied to calculate these terms; the detail of the calculation is discussed in section 4.2. Equation 4.14 can be expressed in matrix form:

$$T^f_{i,I,J} = \left(\begin{bmatrix} k^f_{xx} & k^f_{xy} \\ k^f_{yx} & k^f_{yy} \end{bmatrix} \cdot \begin{Bmatrix} \dfrac{\partial \mathcal{N}^f_i}{\partial x} \\ \dfrac{\partial \mathcal{N}^f_i}{\partial y} \end{Bmatrix} \right)^{\mathbf{T}} \cdot \begin{Bmatrix} n_{x'} \\ n_{y'} \end{Bmatrix} w L_{I,J} \tag{4.15}$$

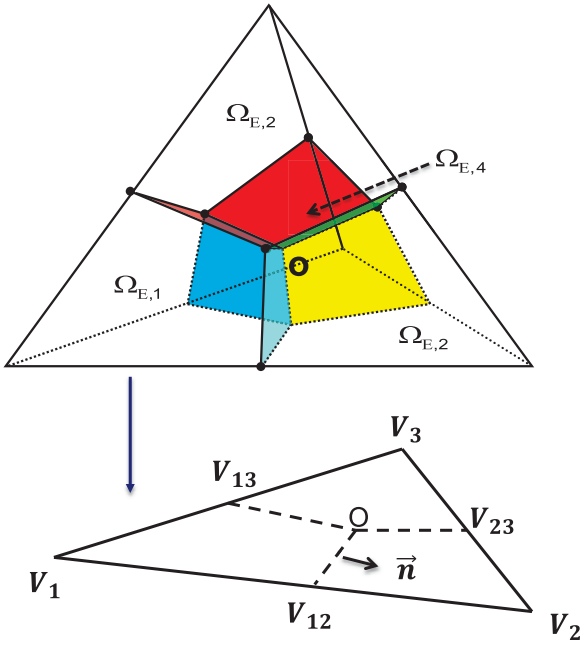

Figure 4.3: A fracture element shown as the side of a matrix tetrahedral element

w is the width or aperture of the fracture and $L_{I,J}$ is the length of the interface between two finite volumes $\Omega_{E,I}$ and $\Omega_{E,J}$.

4.2 Finite Element Method

The finite element method is the base to calculate the gradient of flux term in the reservior model and it is also used in the geomechanical model to calculate the stiffness matrix. The basic idea of finite element method is to find the solution of a complicated problem by replacing it with a simpler one, and the simpler problem is constructed by applying interpolation model [112, 113]. After that, all terms (include derivative terms) existed in the mathematical formulation of the problem can be calculated and the approximate solution can be found.

In ARTS, the same idea is applied and the interpolation models for both reservoir and geomechanical models are based on a tetrahedron or a triangle element. The detail of how to apply finite element in ARTS is discussed in following subsections.

4.2.1 Interpolation Model

First, the interpolation model of a tetrahedron element is introduced. This is the base of calculate $\mathcal{N}_i$ term in the flux calculation of CVFE and the basis function N_i in the

geomechanical model (equation 3.31).

If $\vec{r} = (x, y, z)$ represents the location of a point within a tetrahedral element, the field variable Φ which is a function of $\vec{r}$ can be represented through the combination of nodal variable values and some coefficients in the following equation [114, 115]:

$$\Phi(\vec{r}) = \sum_{i=1}^{4} \alpha_i(\vec{r}_i)\,\Phi_i \tag{4.16}$$

where α_i is called the interpolation function or shape function. Φ_i is the nodal variable value at points 1, 2, 3, and 4 in Figure 4.4 and point $\vec{r}_i$ has the global coordinate (x_i, y_i, z_i).

There are different interpolation methods to calculate $\alpha_i(\vec{r}_i)$. In this research, the interpolation model can be derived by the natural coordinate method or the direct method.

In the natural coordinate method, the tetrahedron element is divided into four subvolumes. Let X be a point located inside the tetrahedral finite element Ω_E with the coordination (x, y, z). Ω_E can be divided into four subvolumes by drawing the lines between the vertices and point X, as shown in Figure 4.4.

The natural coordinates are defined as $\mathcal{N}_i = \dfrac{V_i}{V_{\Omega_E}}$, which is actually the volume fraction. Hence, the sum of all volume fractions is equal to 1:

$$1 = \mathcal{N}_1 + \mathcal{N}_2 + \mathcal{N}_3 + \mathcal{N}_4 \tag{4.17}$$

The property Φ at any point within a tetrahedral element can be rewritten as:

$$\Phi(\vec{r}) = \sum_{i=1}^{4} \mathcal{N}_i(\vec{r}_i)\,\Phi_i \tag{4.18}$$

There are two important features of natural coordinates:

1. The coordinates (x, y, z) are related to the volume fraction by the following relationships:

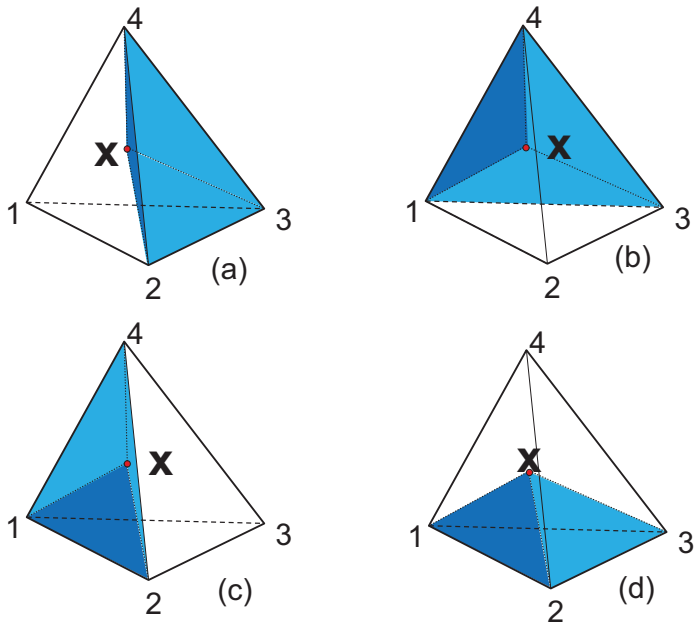

Figure 4.4: The expression of subvolumes within a tetrahedron: (a)$V_1 = V_{X234}$, (b)$V_2 = V_{X134}$, (c)$V_3 = V_{X124}$, (d)$V_4 = V_{X123}$

$$\begin{aligned} x &= \mathcal{N}_1 x_1 + \mathcal{N}_2 x_2 + \mathcal{N}_3 x_3 + \mathcal{N}_4 x_4 \\ y &= \mathcal{N}_1 y_1 + \mathcal{N}_2 y_2 + \mathcal{N}_3 y_3 + \mathcal{N}_4 y_4 \\ z &= \mathcal{N}_1 z_1 + \mathcal{N}_2 z_2 + \mathcal{N}_3 z_3 + \mathcal{N}_4 z_4 \end{aligned} \tag{4.19}$$

2. $\Phi = \Phi_i$ when X is located on the i vertex.

In the direct method, equation 4.16 is expressed in a linear algebra formulation and then the coefficients can be solved:

$$\begin{aligned} \Phi_1 &= \alpha_1 + \alpha_2 x_1 + \alpha_3 y_1 + \alpha_4 z_1 \\ \Phi_2 &= \alpha_1 + \alpha_2 x_2 + \alpha_3 y_2 + \alpha_4 z_2 \\ \Phi_3 &= \alpha_1 + \alpha_2 x_3 + \alpha_3 y_3 + \alpha_4 z_3 \\ \Phi_4 &= \alpha_1 + \alpha_2 x_4 + \alpha_3 y_4 + \alpha_4 z_4 \end{aligned} \tag{4.20}$$

After solving equation 4.20, α_i can be obtained:

$$\begin{aligned}
\alpha_1 &= \frac{1}{6V}(a_1\Phi_1 + a_2\Phi_2 + a_3\Phi_3 + a_4\Phi_4) \\
\alpha_2 &= \frac{1}{6V}(b_1\Phi_1 + b_2\Phi_2 + b_3\Phi_3 + b_4\Phi_4) \\
\alpha_3 &= \frac{1}{6V}(c_1\Phi_1 + c_2\Phi_2 + c_3\Phi_3 + c_4\Phi_4) \\
\alpha_4 &= \frac{1}{6V}(d_1\Phi_1 + d_2\Phi_2 + d_3\Phi_3 + d_4\Phi_4)
\end{aligned} \tag{4.21}$$

where V is the volume of the tetrahedral element, and can be calculated by:

$$V = \begin{vmatrix} 1 & x_1 & y_1 & z_1 \\ 1 & x_2 & y_2 & z_2 \\ 1 & x_3 & y_3 & z_3 \\ 1 & x_4 & y_4 & z_4 \end{vmatrix} \tag{4.22}$$

The coefficients a, b, c and d can be calculated by the following equations:

$$a_1 = \begin{vmatrix} x_2 & y_2 & z_2 \\ x_3 & y_3 & z_3 \\ x_4 & y_4 & z_4 \end{vmatrix} \tag{4.23}$$

$$b_1 = -\begin{vmatrix} 1 & y_2 & z_2 \\ 1 & y_3 & z_3 \\ 1 & y_4 & z_4 \end{vmatrix} \tag{4.24}$$

$$c_1 = -\begin{vmatrix} x_2 & 1 & z_2 \\ x_3 & 1 & z_3 \\ x_4 & 1 & z_4 \end{vmatrix} \tag{4.25}$$

$$d_1 = -\begin{vmatrix} x_2 & y_2 & 1 \\ x_3 & y_3 & 1 \\ x_4 & y_4 & 1 \end{vmatrix} \tag{4.26}$$

Other constants can be calculated using the same equation set (4.23 to 4.26) but with cyclic interchange of the subscripts in the order 4, 3, 2, 1. The signs of determinants in equations 4.23 to 4.26 are to be reversed when calculating a_2, b_2, c_2, d_2 and a_4, b_4, c_4, d_4. If the calculated α_i is substituted into equation 4.20:

$$\Phi(x, y, z) = \mathcal{N}_1\Phi_1 + \mathcal{N}_2\Phi_2 + \mathcal{N}_3\Phi_3 + \mathcal{N}_4\Phi_4 = \bar{\bar{\mathcal{N}}}\vec{\phi^{(e)}} \tag{4.27}$$

Equation 4.27 is similar to equation 4.18 but with different derivation methods.

For triangular elements, the same method discussed above can be applied. The triangle domain can also be divided into three subdomains (4.5).

As shown in Figure 4.5, the total area of three triangles is equal to the triangle element. If we define $L_i = \frac{A_i}{A}$, then the following equation is derived:

$$\sum_{i=1}^{3} L_i = L_1 + L_2 + L_3 = 1 \tag{4.28}$$

The term L_i is actually $\mathcal{N}_i$ in the tetrahedron based finite element interpolation model, hence the term $\mathcal{N}_i$ is also used in the triangle based interpolation model. A linear system can be derived if the relationship between natural and cartesian coordinates is applied:

$$\begin{Bmatrix} 1 \\ x \\ y \end{Bmatrix} = \begin{bmatrix} 1 & 1 & 1 \\ x_1 & x_2 & x_3 \\ y_1 & y_2 & y_3 \end{bmatrix} \begin{Bmatrix} \mathcal{N}_1 \\ \mathcal{N}_2 \\ \mathcal{N}_3 \end{Bmatrix} \tag{4.29}$$

If equation 4.29 is solved, then the shape function $\mathcal{N}_i$ for a triangular element can be calculated as:

$$\begin{Bmatrix} \mathcal{N}_1 \\ \mathcal{N}_2 \\ \mathcal{N}_3 \end{Bmatrix} = \frac{1}{2A} \begin{bmatrix} (x_2y_3 - x_3y_2) & (y_2 - y_3) & (x_3 - x_2) \\ (x_3y_1 - x_1y_3) & (y_3 - y_1) & (x_1 - x_3) \\ (x_1y_2 - x_2y_1) & (y_1 - y_2) & (x_2 - x_1) \end{bmatrix} \begin{Bmatrix} 1 \\ x \\ y \end{Bmatrix} \tag{4.30}$$

where A is the area of the triangle 1, 2, 3, and it can be calculated as:

$$A = \frac{1}{2} \begin{vmatrix} 1 & x_1 & y_1 \\ 1 & x_2 & y_2 \\ 1 & x_3 & y_3 \end{vmatrix} \tag{4.31}$$

A transformation to convert the coordinates of the nodes from 3-D (x, y, z) to 2-D (x', y') is required for the calculation of normal vector and area A ($\vec{n}^f_{I,J}$ and $A^f_{I,J}$ in equation 4.14). Figure 4.6 shows the process of transformation. After the transformation, the new coordinates (x_i', y_i') will be used in equation 4.29 to 4.31.

All the derivative terms in the calculation of fracture or matrix transmissibilities can be derived based on the finite element representation discussed above.

4.2.2 Calculation of Derivative Terms

Equation 4.19 can be expressed as:

$$\vec{X} = \bar{\bar{\mathbf{C}}} \cdot \vec{\mathcal{N}} \tag{4.32}$$

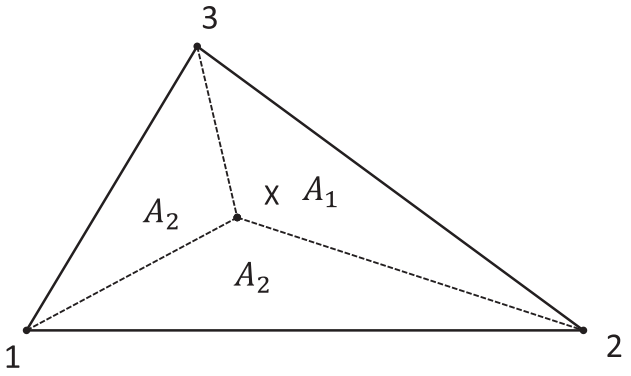

Figure 4.5: Triangular element in finite element method

where $\vec{X} = [x, y, z, 1]^T$, $\bar{\bar{\mathbf{C}}} = \begin{bmatrix} x_1 & x_2 & x_3 & x_4 \\ y_1 & y_2 & y_3 & y_4 \\ z_1 & z_2 & z_3 & z_4 \\ 1 & 1 & 1 & 1 \end{bmatrix}$, and $\vec{\mathcal{N}} = [\mathcal{N}_1, \mathcal{N}_2, \mathcal{N}_3, \mathcal{N}_4]^T$.

Then $\mathcal{N}$ can be derived by solving equation 4.32:

$$\vec{\mathcal{N}} = \bar{\bar{\mathbf{C}}}^{-1} \cdot \begin{bmatrix} x \\ y \\ z \\ 1 \end{bmatrix} \tag{4.33}$$

Hence, $\nabla\mathcal{N}_i$ can be calculated by:

$$\nabla\vec{\mathcal{N}} = \bar{\bar{\mathbf{C}}}^{-1} \cdot \begin{Bmatrix} \nabla x \\ \nabla y \\ \nabla z \\ \nabla 1 \end{Bmatrix} = \bar{\bar{\mathbf{C}}}^{-1} \cdot \begin{bmatrix} 1 & 0 & 0 \\ 0 & 1 & 0 \\ 0 & 0 & 1 \\ 0 & 0 & 0 \end{bmatrix} \tag{4.34}$$

The term $\mathcal{N}$ is already obtained when solving coefficients α in the second method of deriving the interpolation model. With the calculated $\mathcal{N}_i$, the derivative of the field variable $\Phi_{\vec{r}}$ can be obtained:

$$\nabla\Phi\left(\vec{r}\right) = \sum_{i=1}^{4} \nabla\mathcal{N}_i\left(\vec{r}_i\right)\Phi_i \tag{4.35}$$

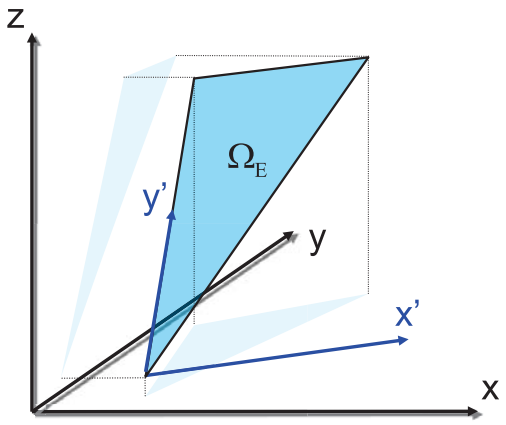

Figure 4.6: Transformation of 3-D fracture element into 2-D.

The derivative of Φ depends on all four nodal field variables and the interpolation functions. The calculation of the gradient of $\mathcal{N}$ can be derived from equation 4.21.

For a triangular element, the same method is used to derive the gradient term. The derivative of the shape function of fracture element is:

$$\nabla\vec{\mathcal{N}} = \begin{bmatrix} x'_1 & x'_2 & x'_3 \\ y'_1 & y'_2 & y'_3 \\ 1 & 1 & 1 \end{bmatrix}^{-1} \cdot \begin{Bmatrix} \nabla x' \\ \nabla y' \\ \nabla 1 \end{Bmatrix} \tag{4.36}$$

By applying equation 4.31, the $\nabla\vec{\mathcal{N}}$ can be rewritten as:

$$\nabla\vec{\mathcal{N}} = \begin{bmatrix} x'_1 & x'_2 & x'_3 \\ y'_1 & y'_2 & y'_3 \\ 1 & 1 & 1 \end{bmatrix}^{-1} \cdot \begin{bmatrix} 1 & 0 \\ 0 & 1 \\ 0 & 0 \end{bmatrix} \tag{4.37}$$

Then the derivative term for a property Φ_f in the fracture element can be expressed as:

$$\nabla\Phi_f\left(\vec{r}\right) = \sum_{i=1}^{3} \nabla\mathcal{N}_i\left(\vec{r}_i\right)\Phi_{f_i} \tag{4.38}$$

All the derivative terms in matrix or fracture transmissibility calculation are derived above, but some geometrical properties like interface area are also needed to calculate the transmissibility.

4.2.3 Geometric Property Calculation

As shown in equation 4.9, the geometrical properties are also needed in calculating the transmissibility and the flux term. For example, in a tetrahedral element, $\vec{n}$ and $A_{I,J}$ are required for the calculation of the flux between two control volumes $\Omega_{E,I}$ and $\Omega_{E,J}$. Figure 4.7 shows a tetrahedron element and some of the geometrical properties that need to be calculated. Point O is the center point of the tetrahedron. Point $V_{face_{I,J,K}}$ is the center point of the triangle I, J, K which is the external surface of a tetrahedron element. Point $V_{edge_{I,J}}$ is the center point of the edge I, J in a triangle surface. The corner point of the tetrahedron is defined as V_I.

In order to obtain the interface area and corresponding normal vector, all the coordinates of these special points should be calculated. In a tetrahedron, the coordinates of the center point O are calculated using the following formulation:

$$\nu_o = \frac{\sum_{i=1}^{4} \nu_{V_i}}{4} \tag{4.39}$$

where $\nu \equiv x, y, z$, and it is also used in equation 4.40. The coordinates of the center points of a triangle and an edge can be calculated as:

$$\nu_{V,face} = \frac{\sum_{i=1}^{3} \nu_{V_i}}{3} \tag{4.40}$$

$$\nu_{V,edge} = \frac{\sum_{i=1}^{2} \nu_{V_i}}{2}$$

The normal vector of the plane shown $\vec{n}$ in Figure 4.7 is obtained by:

$$\vec{n} = \frac{\overrightarrow{V_{edge12}V_{V_3}} \times \overrightarrow{V_{edge12}V_{V_4}}}{\|\overrightarrow{V_{edge12}V_{V_3}} \times \overrightarrow{V_{edge12}V_{V_4}}\|} \tag{4.41}$$

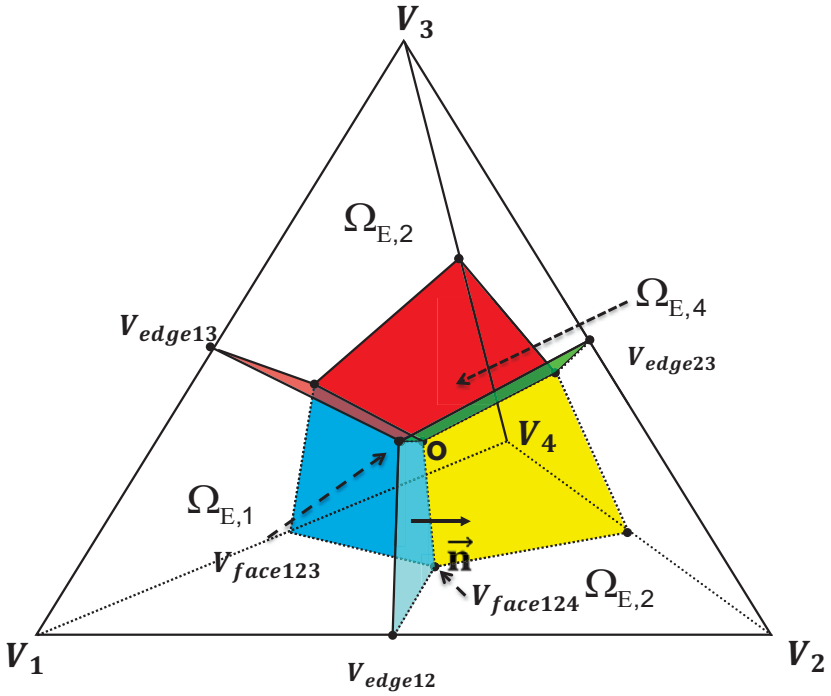

Figure 4.7: Illustration of some geometrical properties in a tetrahedron element in CVFE method

While the interface area $A_{I,J}$ corresponding to vector $\vec{n}$ in Figure 4.7 can be calculated as:

$$A_{I,J} = \frac{1}{12} \| \overrightarrow{V_{edge12} V_{V_3}} \times \overrightarrow{V_{edge12} V_{V_4}} \| \tag{4.42}$$

the geometric properties in a triangle element shown in Figure 4.3 can be calculated by:

$$\begin{aligned} \nu'_{V_O} &= \frac{\sum_{i=1}^{3} \nu'_{V_i}}{3} \\ \nu'_{V_{i,j}} &= \frac{\nu'_{V_i} + \nu'_{V_j}}{2} \\ \vec{n} &= \frac{\overrightarrow{V_{O' V'_{i,j}}}}{\| \overrightarrow{V_{O' V'_{i,j}}} \|} \end{aligned} \tag{4.43}$$

where ν' is the new coordinate after coordinate transformation, the subscripts are also applied in calculating the normal vector $\vec{n}$ to indicate that the new coordinates are used. With all the derivative terms and geometrical properties, the transmissibilities of a tetrahedron or a triangle element can be calculated. Hence, the governing equations can be written into discretization formulations.

4.3 Finite Volume Method

The finite volume method developed in the framework is to connect the framework with external geometrical information to perform reservoir simulation. In order to achieve this goal, two types of information (volumes and transmissibilities of the finite volumes in a reservoir) are passed into ARTS from other software. As discussed above, these types of information can be computed in advance and used in the flow simulation later. Therefore, the general finite element method is created to read and store volume and transmissibility information from external software and perform reservoir simulations.

Figure 4.8 shows the general geometric that can be handled by finite volume method. In a finite region Ω_E, two connected parts $\Omega_{E,I} \in CV_I$ and $\Omega_{E,J} \in CV_J$ share a common boundary $\Gamma_{I,J} = \Omega_{E,I} \cap \Omega_{E,J}$. The flux between these two finite volumes can also be calculated using equation 4.2.

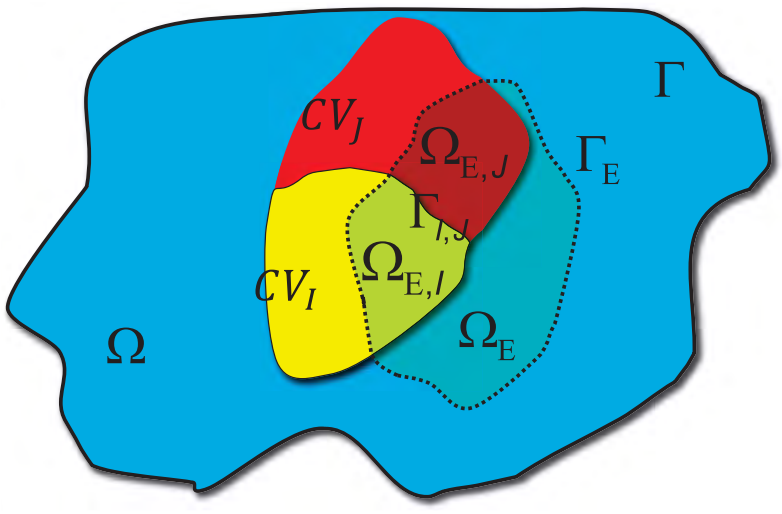

Figure 4.8: Illustration of a finite volume domain

4.4 Finite Difference Method

Finite difference method is also applied in ARTS. In this method, the reservoir is divided into numerous blocks and all the reservoir properties are assigned in the center point of the block. Each block is defined as a finite volume, and the combination of all the finite volumes is the finite region.

Two kinds of finite difference methods are generally used, one is the standard finite element method, the other is the corner point finite difference method. In the standard finite difference method, the whole reservoir is divided into numerous rectangle blocks and the geometric information can be defined by the center point of the block. In the corner point finite difference method, the whole reservoir is divided into numerous irregular rectangle blocks and the geometric information is defined by the corner points in each block. All these methods are discussed in detail.

4.4.1 Standard Finite Difference Method

For the standard finite difference method, all finite volumes are rectangle blocks, and the primary variables are block-based. The volume is computed as $\Delta V_{\mathbb{CV}} = DxDyDz$. In Figure 4.9, the transmissibility $T_{i,i,j}$ between two x-direction connected control volumes i and j are calculated as:

$$\begin{aligned} T_{i,i,j} &= \frac{A_{i,j}D_{i,j}}{B_{i,j}} \\ A_{i,j} &= \frac{Dx_iDy_iDz_i + Dx_jDy_jDz_j}{Dx_i + Dx_j} \\ D_{i,j} &= \frac{(Dx_i + Dx_j)^2}{(Dx_i + Dx_j)^2 + 4(D_i - D_j)^2} \\ B_{i,j} &= 0.5(\frac{Dx_i}{k_{x,i}} + \frac{Dx_j}{k_{x,j}}) \end{aligned} \tag{4.44}$$

The flux of phase p can be calculated using the transmissibility formulation:

$$\begin{aligned} F_{p,i,j} &= m_p(T_{i,i,j}\Phi_{p,i} + T_{j,i,j}\Phi_{p,j}) \\ T_{j,i,j} &= -T_{i,i,j} \end{aligned} \tag{4.45}$$

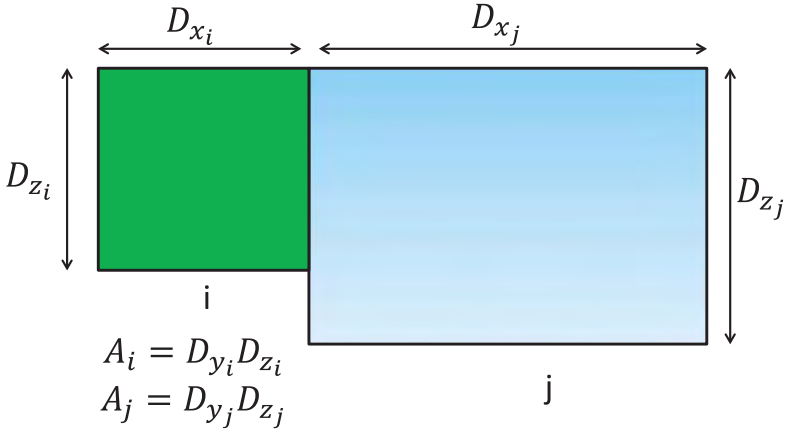

Figure 4.9: Illustration of the transmissibility calculation in the standard finite difference method

4.4.2 Corner Point Method

For the complex reservoir model, the coarsening corner point grid mesh is a good approach to reduce the number of gridblocks. The primary variables are still block-based as in the standard finite difference method. However, the finite volume is defined by the location of eight corner points. The volume of the grid block is very complex. The grid block can be divided into 6 tetrahedrons. Each tetrahedron has four vertices, $a = (a_1, a_2, a_3)$, $b = (b_1, b_2, b_3)$, $c = (c_1, c_2, c_3)$, and $d = (d_1, d_2, d_3)$, and the volume is equal to $\frac{1}{6} \mid |det(a-b, b-c, c-d)| \mid$.

In Figure 4.10, the transmissibility $T_{i,i,j}$ between two connected finite volumes in x direction$block_i$ and $block_j$ is calculated as

$$\begin{aligned} T_{i,i,j} &= \frac{1}{\frac{1}{T_i} + \frac{1}{T_j}} \\ T_i &= k_{x,i} \frac{A_{x,i,j} Dx_i + A_{y,i,j} Dy_i + A_{z,i,j} Dz_i}{Dx_i^2 + Dy_i^2 + Dz_i^2} \\ T_j &= k_{x,i} \frac{A_{x,i,j} Dx_j + A_{y,i,j} Dy_j + A_{z,i,j} Dz_j}{Dx_j^2 + Dy_j^2 + Dz_j^2} \end{aligned} \tag{4.46}$$

where $A_{x,i,j}$, $A_{y,i,j}$, and $A_{z,i,j}$ are the projections of interface area between the control volume i and j. D_j is the distance between the center of the block and interface. Dx_j, Dy_j, and Dz_j are the projections of D_j in x,y and z directions.

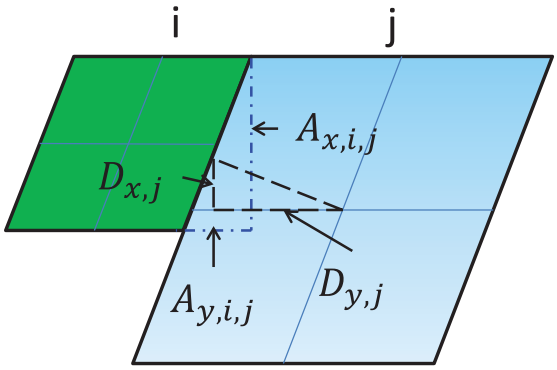

Figure 4.10: Schematic illustration of the transmissibility calculation in the corner point method

The same form is applied to calculate the flux of phase p as in the standard finite difference method.

$$\begin{aligned} F_{p,i,j} &= m_p(T_{i,i,j}\Phi_{p,i} + T_{j,i,j}\Phi_{p,j}) \\ T_{j,i,j} &= -T_{i,i,j} \end{aligned} \tag{4.47}$$

Thus, both structured and unstructured meshes can be implemented for the finite difference method in this model.

4.5 Well Model

Line source is implemented in ARTS. In this model, the well is discretized as a series of point sources in the reservoir domain (Figure 4.11). The production or injection rate of a well can be expressed as:

$$q_{well,p} = WI\lambda_p(P_{well,p} - P_{cv,p}) \tag{4.48}$$

where WI is the well index, λ_p is the mobility term of phase p, $P_{well,p}$ is the pressure in the well of phase p, $P_{cv,p}$ is the pressure of phase p in the control volume connected with the well. The calculation of the well index (WI) in equation (4.48) is related to the discretization method. Peaceman [116] developed a classic well model and the well index can be calculated

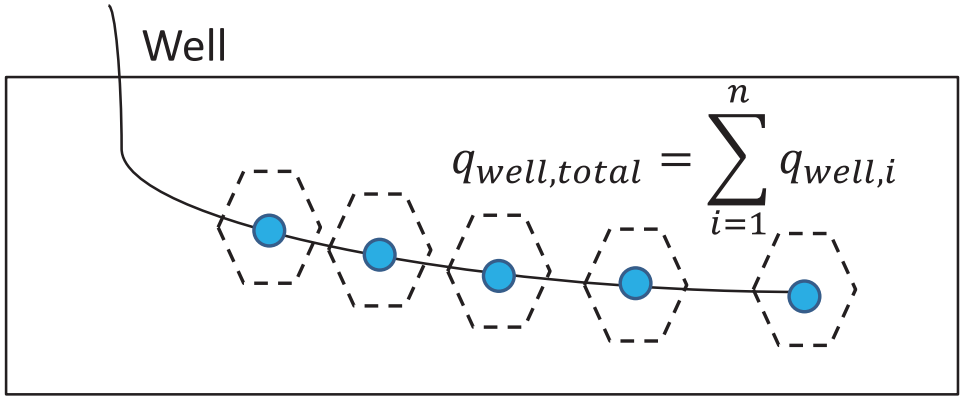

Figure 4.11: Illustration of line source well in ARTS

as:

$$WI_I = \left(\frac{2\pi h K_{wb} f_h f}{\ln \frac{r_{eff}}{r_{wb}} + \mathrm{s}} \right)_I \tag{4.49}$$

where h is the length of the well segment, K_{wb} is the permeability perpendicular to the well, f_h is the interval length factor, f is the well fraction, r_{wb} is the well bore radius, s is the skin factor and r_{eff} is the effective radius r_{eff}. Among all parameters listed above, the effective radius is related to discretization methods. In a finite difference method with cartesian grid (Figure 4.12), it can be calculated by:

$$r_{eff} = \frac{2}{\sqrt{\pi}} \frac{\sqrt{\sqrt{k_{yy}/k_{xx}}\Delta x^2 + \sqrt{k_{xx}/k_{yy}}\Delta y^2}}{(k_{yy}/k_{xx})^{1/4} + (k_{xx}/k_{yy})^{1/4}} \tag{4.50}$$

Figure 4.12 shows some of the parameters in calculating the effective radius in a 2-D CVFE model. It can be obtained by:

$$r_{eff} = \left(\frac{A_{cv}}{\pi} \right)^{1/2} \tag{4.51}$$

For the 3-D CVFE model, the calculation of r_{eff} is related to the volume of the corresponding control volume and the length of the well segment in that control volume [117]. It can

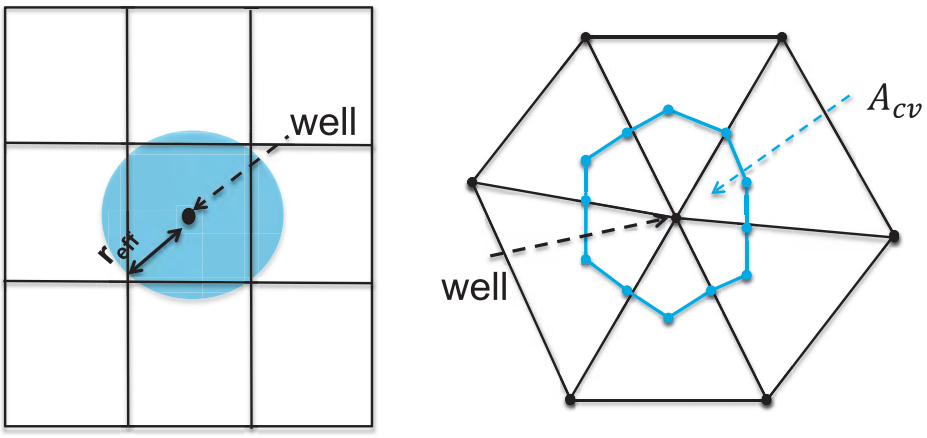

Figure 4.12: Illustration of well index calculation for 2-D finite difference method and CVFE method

be obtained by:

$$r_{eff} = \left(\frac{V_{cv}}{\pi L_{wb}}\right)^{1/2} \tag{4.52}$$

where L_{wb} is the length of well segment within the control volume, V_{cv} is the volume of the control volume.

CHAPTER 5

VERIFICATION OF THE FRAMEWORK

A numerical framework needs to be verified and validated before it can be applied to solve some scientific or real field problems. In this process, the accuracy and stability of the framework are checked to see if these meet the specifications of the original design. There are various verification and validation methods, like analytical solution method, and index method, which are widely used in the industry. These methods are also applied in this research.

In order to validate and verify the ARTS framework, several studies have been done. Since several submodels have been validated and verified in previous work [82, 83, 85, 86], the verification studies discussed in this chapter are focused on the geomechanical part. It is hard to obtain real field data, hence most studies in this chapter come from the literature and other widely used commercial software. Several verification and validation case studies are discussed in this chapter, and the result shows the agreement between ARTS and other software or analytical solutions.

5.1 1-D Consolidation Problem

The first verification case is a 1-D consolidation problem with linear poroelasticity. The analytical solution to this problem is provided by Jaeger et al. (2007) [118]. This is actually a 1-D Terzaghi problem [28, 119], in which a layer of porous media was subjected to a normal external load at the surface. Analytical solutions of this problem have been derived from the original research work done by Terzaghi in 1923, but the original solution was restricted to the problem where the vertical strain is small. To extend the limitation of the problem, several researches [120, 121, 122] have modified the original formulations.

A fluid filled poroelastic layer of soil extending from the surface $z = 0$ down to the depth $z = h$ is under a normal traction load p at time $t = 0$ on the upper surface. The analytical solutions of pore pressure and vertical displacement can be derived if the linearized theory is applied.

The initial pore pressure and initial vertical displacement can be calculated by:

$$\begin{aligned} P_p^0 &= \frac{\alpha M}{\lambda + 2G + \alpha^2 M} P \\ w^0 &= \frac{P}{\lambda + 2G + \alpha^2 M}(z - h) \end{aligned} \tag{5.1}$$

where λ is the Lame's first parameter, P_p^0 is the initial pore pressure, w^0 is the initial vertical displacement, and M is the Biot modulus which can defined as:

$$M = \frac{BK}{\alpha(1 - \alpha B)} \tag{5.2}$$

where K is the bulk modulus, B is the Skempton coefficient which is equal to one when the fluid is assumed to be incompressible.

In this case, the initial strain (ϵ_{xx} and ϵ_{yy}) in the horizontal direction is assumed to be zero. By applying the force balance equation and the initial conditions, the evolution of the pore pressure and vertical displacement can be derived. The pore pressure can be calculated by:

$$P_p(z,t) = \frac{\alpha M P}{\lambda + 2G + \alpha^2 M} \sum_{n=1,3,\cdots}^{\infty} \frac{4}{n\pi} sin\left(\frac{n\pi z}{2h}\right) exp\left(\frac{-n^2\pi^2 kt}{4\mu S h^2}\right) \tag{5.3}$$

where k is the permeability and μ is the viscosity, S is the storage factor defined as:

$$S = \frac{1}{M} + \frac{\alpha^2}{K + 4G/3} \tag{5.4}$$

The steady state time for this system to reach equilibrium can be expressed as:

$$t_{eq} \approx \frac{20\mu S h^2}{\pi^2 k} \approx \frac{2\mu S h^2}{k} \tag{5.5}$$

The dimensionless pore pressure can be calculated as:

$$\frac{P_p(z,t)}{P_p^0} = 1 - \sum_{n=0}^{\infty}(-1)^n \left\{ \text{erfc}\left[\frac{2nh + z}{(4kt/\mu S)^{\frac{1}{2}}}\right] + \text{erfc}\left[\frac{2(n+1)h - z}{(4kt/\mu S)^{\frac{1}{2}}}\right] \right\} \tag{5.6}$$

where erfc(x) is the coerror function and it can be calculated as [123]:

$$\text{erfc}(x) \equiv 1 - \text{erf}(x) = \frac{2}{\pi} \int_x^\infty e^{-\eta^2} d\eta \tag{5.7}$$

The vertical displacement can be calculated as:

$$w(z,t) = \frac{P}{\lambda + 2G} \left[(z-h) + C_e \sum_{n=1,3,\cdots}^{\infty} \frac{8}{n^2\pi^2} cos\left(\frac{n\pi z}{2h}\right) exp\left(\frac{-n^2\pi^2 kt}{4\mu S h^2}\right) \right] \tag{5.8}$$

where C_e is a coefficient defined as:

$$C_e = \frac{\alpha^2 M h}{\lambda + 2G + \alpha^2 M} \tag{5.9}$$

The upper surface vertical displacement can be calculated as:

$$w(0,t) = \frac{-Ph}{\lambda + 2G} \left[1 - \sum_{n=1,3,\cdots}^{\infty} \frac{8}{n^2\pi^2} exp\left(\frac{-n^2\pi^2(\lambda + 2G)kt}{4\mu h^2}\right) \right] \tag{5.10}$$

The ARTS framework is used to solve this problem and the result is compared with the analytical solution, some of the important properties used in the simulation are listed in Table 5.1. In this verification study, the fluid is assumed to be incompressible and the strain in the horizontal direction is enforced to be zero in the simulation. A source term is applied to simulate the drained condition.

Results of this case study are summarized in Figures 5.1 and 5.2. The pore pressure and vertical displacement obtained from ARTS match closely with the analytical solution. This excellent agreement shows the validity of the simulation result of ARTS, and hence we can conclude that ARTS solves the governing system correctly. The evolution of the soil's displacement with respect to the initial surface pressure load is clearly shown in this case study. Initially, the rock deforms elastically when the excess pore pressure is introduced in the rock. After some time, the pore pressure will relax back to the initial state, but the deformation still propagates downward in the rock. This whole process is a typical consolidation process with a drained condition.

Table 5.1: Summary of important properties of 1-D consolidation case

Discretization method	CVFE
Geometry information	
L_x, L_y, L_z (ft)	1,1,300
Number of fractures	0
Rock property	
ϕ	0.20
Pore compressibility $\left(\frac{1}{PSI}\right)$	2.2e-6
Permeability (mD)	150.0
Biot coefficient	0.60
Shear modulus (PSI)	8.7e5
Lame's parameter (PSI)	5.8e5
Fluid property	
Water viscosity (cp)	1.0
Initial conditions	
$P\,(PSI)$	15.0
S_w	0.3

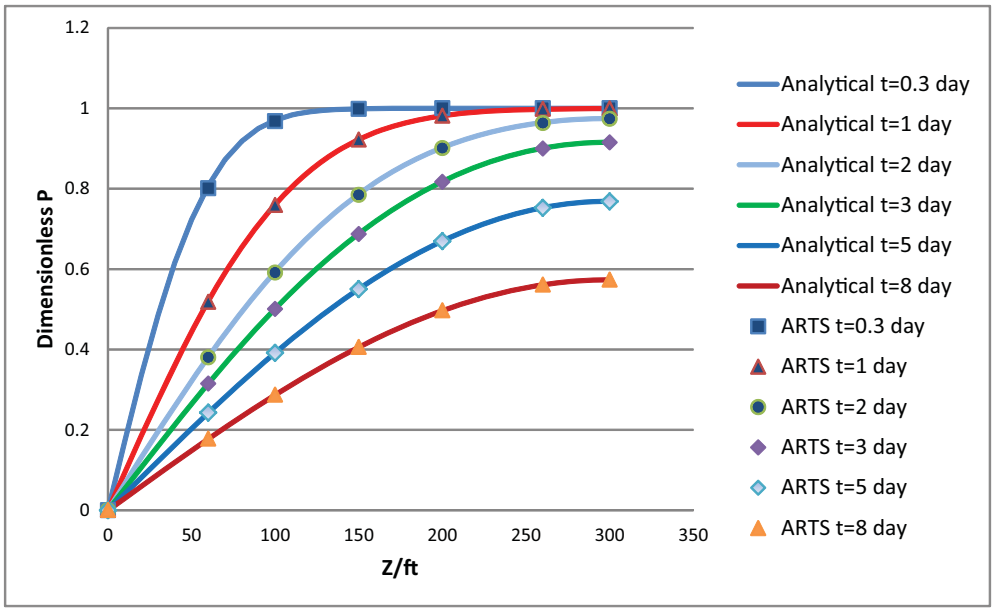

Figure 5.1: Comparison of pressure for 1-D consolidation

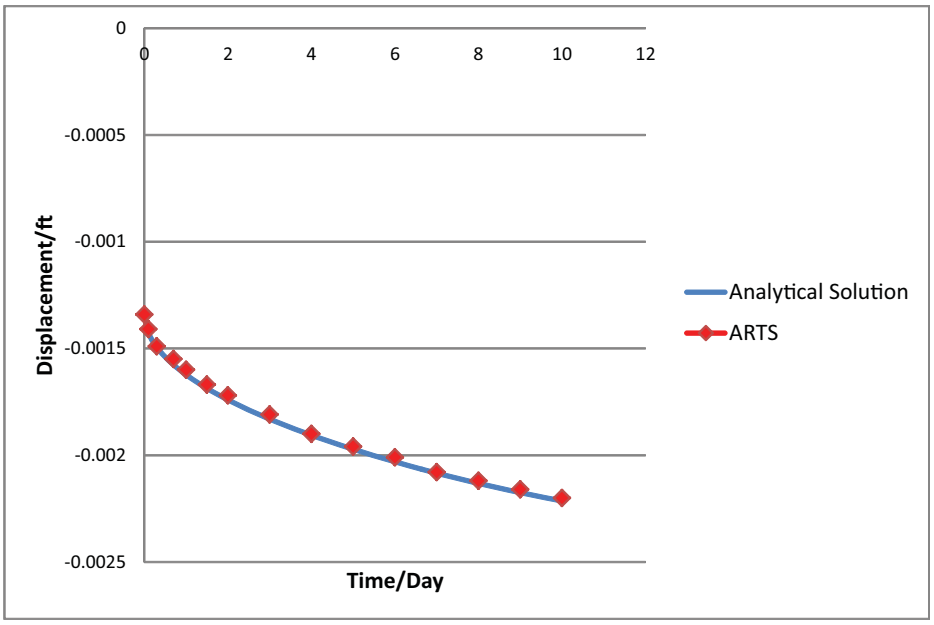

Figure 5.2: Comparison of displacement for 1-D consolidation

The purpose of this case study is to prove the validity of ARTS in solving the 1-D coupled problem, and the result is excellent. In this simple 1-D problem, the consolidation process and the trend of the displacement changes with respect to pressure depletion are clearly illustrated. But, the governing equation for the 1-D problem is a simplified version of the governing equations which ARTS solves, hence a 2-D problem is studied in the following section to provide more evidence of the validity of ARTS.

5.2 2-D Problem

The second verification case study is a 2-D rock under pressure load. This problem comes from the reversion of Mandel's problem. Mandel (1953) [124] presented one of the first solutions for the three dimensional consolidation of Biot's problem which demonstrates the nonmonotonic pore pressure effect. The effect of Poission's ratio on the magnitude of pore pressure development and dissipation was illustrated by later research which is based on Mandel's original research [125]. The nonmonotonic pressure effect has been referred to as the Mandel-Cryer effect [126, 127, 128]. The physical phenomenon has been confirmed in the field as the Noordbergum effect [129]. Hence, the solution of Mandel's problem has been used as a benchmark problem for testing the validity of numerical code for poroelasticity [130, 131]. In this research, Mandel's problem is also used as a verification case study but with some modifications to simplify the original problem.

The original Mandel problem involves an infinitely long rectangular specimen, sandwiched at the top and the bottom by two rigid plates with no friction [132]. Figure 5.3 shows the basic geometry of Mandel's problem.

The specimen contains incompressible solid saturated single phase fluid. The initial pore pressure is p_0. The lateral sides are free from normal and shear stress, and the top and bottom of the specimen have an external force load which is $2F$ per unit thickness at time $t = 0^+$. The lateral boundary surfaces S_1 and S_2 perpendicular to x direction are traction free and exposed to the surrounding environment, which also has the pressure p_0. According to the Skempton effect [133], a pressure rise will be observed inside the specimen as the force starts to be applied on the boundary. Drainage will occur at the side surfaces, and pressure dissipation will also happen. The pressure depletion will later propagate to the inner region of the specimen. Once the pressure rise vanishes, the drainage will stop. This is a fairly simple physical process, but obtaining the analytical solution is not easy.

The original solution provided by Mandel only includes pore pressure. Then, Abousleiman et al. (1996) [132] revisited the problem and extended the solution to compressible fluids and skeletons, and the material behavior was generalized from isotropy to transverse isotropy. Indeed, the complete solutions of stress, displacement and pore pressure are provided [134, 135, 136].

For the particular verification problem, the rock media is assumed to be isotropic, and the original solution is modified to meet this assumption. The modified analytical solutions of this problem are listed in equations 5.11 to 5.14. The displacement in x direction can be calculated by:

$$\begin{aligned} u_x = \quad & \left[\frac{F\nu}{2Ga} - \frac{F\nu_u}{Ga}\sum_{i=1}^{\infty}\frac{sin\beta_i cos\beta_i}{\beta_i - sin\beta_i cos\beta_i} exp\left(\frac{-\beta_i^2 ct}{a^2}\right)\right] x \\ & + \frac{F}{G}\sum_{i=1}^{\infty}\frac{sin\beta_i cos\beta_i}{\beta_i - sin\beta_i cos\beta_i} sin\frac{\beta_i x}{a} exp\left(\frac{-\beta_i^2 ct}{a^2}\right) \end{aligned} \tag{5.11}$$

the displacement in y direction can be expressed as:

$$u_y = \left[-\frac{F(1-\nu)}{2Ga} + \frac{F(1-\nu)}{Ga}\sum_{i=1}^{\infty}\frac{sin\beta_i cos\beta_i}{\beta_i - sin\beta_i cos\beta_i} exp\left(\frac{-\beta_i^2 ct}{a^2}\right)\right] y \tag{5.12}$$

the pore pressure can be calculated by:

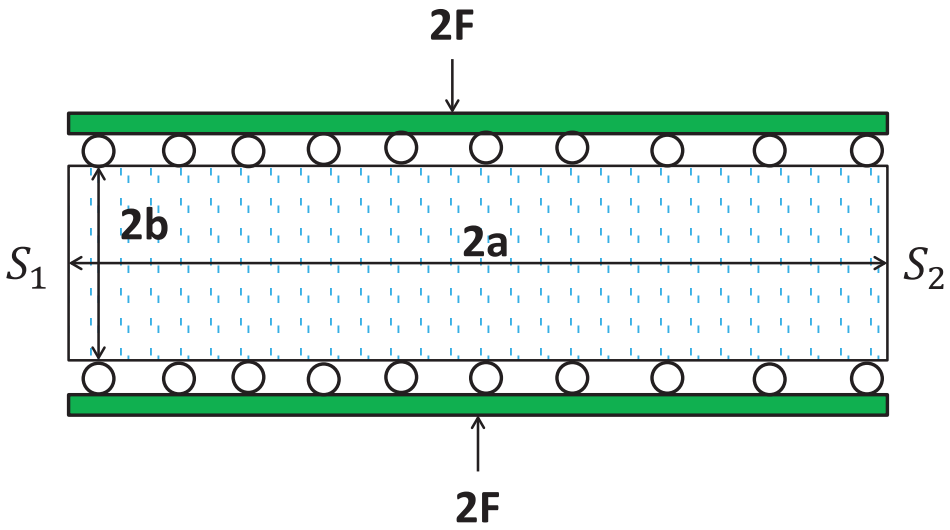

Figure 5.3: Original geometry of Mandel's problem

$$p = \frac{2FB(1+\nu_u)}{3a}\sum_{i=1}^{\infty}\frac{sin\beta_i cos\beta_i}{\beta_i - sin\beta_i cos\beta_i}\left(cos\frac{\beta_i x}{a} - cos\beta_i\right)exp\left(\frac{-\beta_i^2 ct}{a^2}\right) \tag{5.13}$$

the stress in y direction can be calculated by:

$$\begin{aligned}\sigma_{yy} = \quad & -\frac{F}{a} - \frac{2F(\nu_u-\nu)}{a(1-\nu)}\sum_{i=1}^{\infty}\frac{sin\beta_i cos\beta_i}{\beta_i - sin\beta_i cos\beta_i}cos\frac{\beta_i x}{a}exp\left(\frac{-\beta_i^2 ct}{a^2}\right) \\ & +\frac{2F}{a}\sum_{i=1}^{\infty}\frac{sin\beta_i cos\beta_i}{\beta_i - sin\beta_i cos\beta_i}exp\left(\frac{-\beta_i^2 ct}{a^2}\right)\end{aligned} \tag{5.14}$$

the stress in x direction and the shear stress are eliminated by the problem setting:

$$\sigma_{xx} = \sigma_{xy} = 0 \tag{5.15}$$

β_i is a coefficient defined as:

$$tan\beta_i = \frac{1-\nu}{\nu_u - \nu}\beta_i \tag{5.16}$$

In the above equations, G is the shear modulus, B is the Skempton pore pressure coefficient, c is the diffusivity coefficient, v_u is the undrained Poisson's ratio. These coefficients can be

related to some basic mechanical parameters such as Young's modulus E and Poission's ratio ν by the following equations [137]:

$$\begin{aligned} G &= \frac{E}{2(1+\nu)} \\ B &= 1 - \frac{\phi K(K_s - K_f)}{K_f(K_s - K) + \phi K(K_s - K_f)} \\ \nu_u &= \frac{3\nu + B(1-2\nu)(1-\frac{K}{K_s})}{3 - B(1-2\nu)(1-\frac{K}{K_s})} \\ c &= \frac{2\mathcal{K}B^2G(1-\nu)(1+\nu_u)^2}{9\mu_f(1-\nu_u)(\nu_u-\nu)} \end{aligned} \tag{5.17}$$

where K is the bulk modulus of the skeleton, K_s is the bulk modulus of the solid, K_f is the bulk modulus of the fluid in the pore space. If the fluid in the pore space and the solid skeleton are assumed to be incompressible ($K_f = 0$ and $K_s = 0$), then equation 5.17 can be rewrite as:

$$\begin{aligned} B &= 1 \\ \nu_u &= 0.5 \\ c &= \frac{2\mathcal{K}G(1-\nu)}{\mu_f(1-2\nu)} \end{aligned} \tag{5.18}$$

In order to study the 2-D problem in ARTS, the geometry of the Mandel's problem has been modified. The geometry of the domain studied and some of the boundary conditions used in the simulation are illustrated in Figure 5.4. The study area shown in Figure 5.4 has a width of 330 ft and a height of 33 ft. The bottom and left boundaries are confined in the horizontal and vertical direction. The top boundary has a load $P0$ and a source term is applied at the right boundary to simulate the drained condition. The shear stress terms are enforced to be zero by adjusting the coefficient matrix. The fluid saturated in the domain is assumed to be incompressible and has the viscosity of water at room temperature; hence the parameters listed in equation 5.18 can be applied. Some of the important parameters and properties used in this case study are listed in Table 5.2.

As illustrated above, the physical phenomenons observed in this case are governed by the Skempton effect and results are displayed in Figure 5.5 and 5.6. From the comparison of

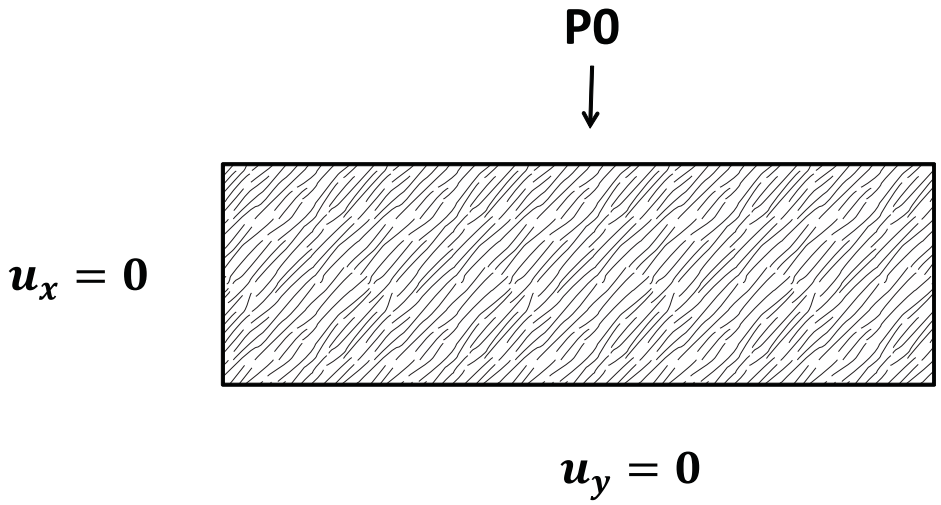

Figure 5.4: Geometry of the 2-D verification problem

Table 5.2: Summary of important properties of 2-D verification problem

Discretization method	CVFE
Geometry information	
L_x, L_y, L_z (ft)	330,33,200
Number of fractures	0
Rock property	
ϕ	0.20
Pore compressibility $\left(\frac{1}{PSI}\right)$	0
Permeability (mD)	150.0
Biot coefficient	1
Young's modulus (PSI)	1.45e6
Shear modulus (PSI)	6e5
Possion's ratio	0.2
Surface P_0 (PSI)	1.45e4
Fluid property	
Water viscosity (cp)	1.0
Initial conditions	
S_g	0.0
S_w	1.0

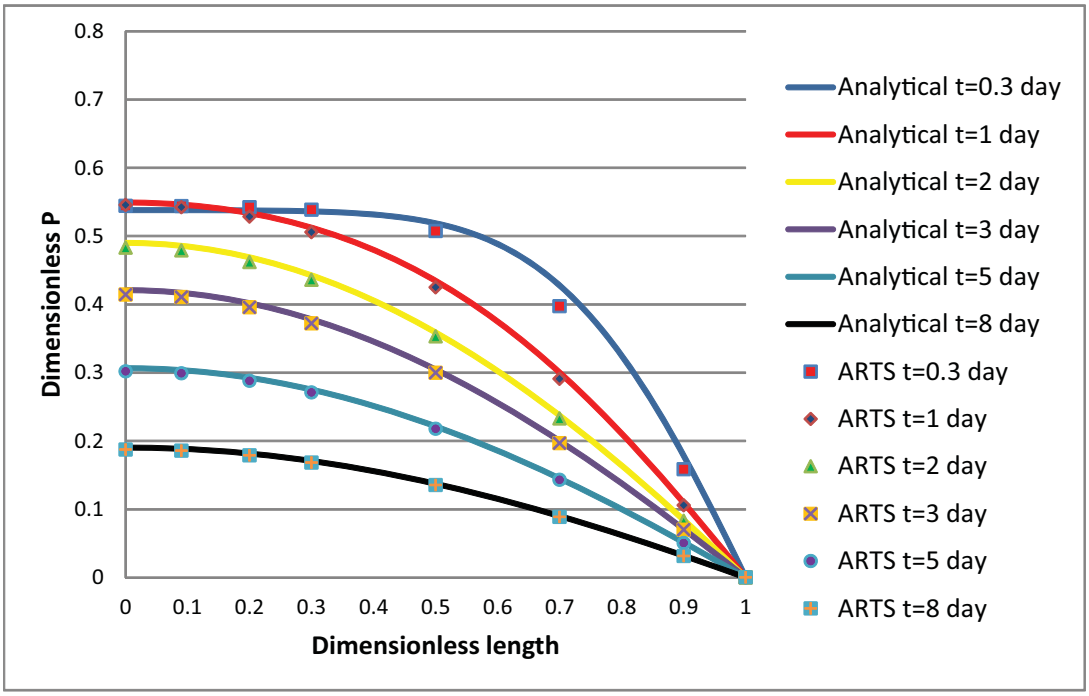

Figure 5.5: Comparison of pressure for 2-D problem

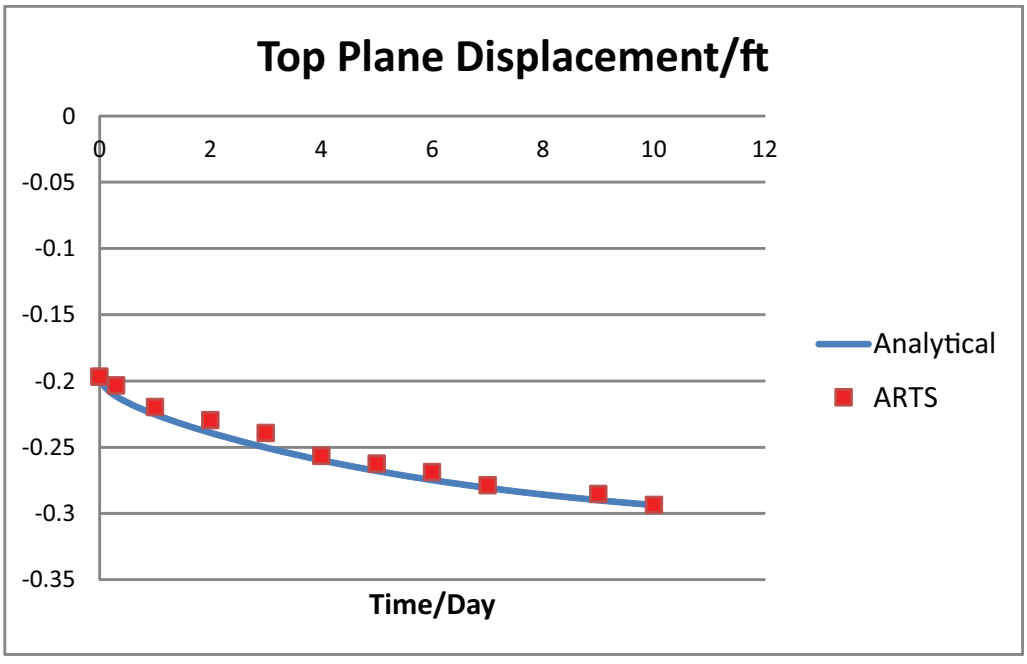

Figure 5.6: Comparison of displacement for 2-D problem

dimensionless pressure $\frac{P}{2FL_x}$ and the vertical displacement, an excellent agreement between the analytical solution and ARTS simulation can be observed. This confirms the validity of ARTS and proves that the simulation results from ARTS are the correct solution of the governing equations in this case. In this case, the governing equations are in 2-D and the flow equation is just the continuity equation with Darcy's law. It is not exactly the same with the equations solved in ARTS, but we can still obtain excellent results with some assumptions. A 3-D analytical solution is needed to fully verify ARTS, however a 3-D analytical solution for this type of problem is not well established.

In summary, the two case studies discussed prove the validity of ARTS and verify the numerical results with the analytical solution. Although the problem solved in ARTS is 3-D, these verification studies are enough for the conclusion that ARTS solves the governing equation correctly. The agreement with analytical solution shows the validity of ARTS in solving certain types of equations, but the goal of developing ARTS is for solving real field problems. Hence, another case study is discussed in the next section to compare ARTS with the commercial software which is widely used in the oil and gas industry.

5.3 Benchmark with STARS

As discussed in the previous section, verification with commercial software is necessary to verify ARTS framework. This is also called index method for verifying and validating a computational code. In this case study, the reservoir simulator, STARS from the Computer Modeling Group (CMG), is used for verification purposes with ARTS.

STARS is a widely used compositional reservoir simulator in the oil and gas industry. A geomechanical model has been integrated in recent years [138, 139]. However, there is no industry standard for geomechanical reservoir simulations as a result of some unsolved difficulties involved in coupling geomechanics with reservoir simulation, such as running speed and adaptability. The comparison of ARTS and STARS is just to show the agreement between these two simulators and that ARTS has the potential to be applied in solving real field problems.

The reservoir model in STARS has a K value based compositional model with a geomechanical model that has nonlinear elasticity and plasticity models. Some parameters are adjusted in STARS to enforce the linear poroelasticity model, which is used in ARTS. Indeed, the black oil simulation data is converted to a data set which meets the requirements of a K value thermal model, some important properties are listed in Table 5.3.

Table 5.3: Summary of important properties of benchmark study with STARS

Discretization method	CVFE
Geometry information	
L_x, L_y, $L_z\,(ft)$	2200,2200,200
Number of fractures	0
Rock property	
ϕ	0.25
Initial $k\,(mD)$ for matrix	100.0
Initial depth (ft)	4010.0
Pore compressibility $\left(\frac{1}{PSI}\right)$	3.0e-6
Biot coefficient	1.0
Young's modulus (PSI)	1e4
Possion's ratio (PSI)	0.3
Rock fluid data	
$Pc_{gw}\,(PSI)$	0
S_w	0.2,0.3,0.4,0.5,0.65,0.7,0.8,0.9,1.0
kr_g	0.0,0.07,0.15,0.24,0.33,0.65,0.83,1.0
kr_w	1.0,0.8,0.6,0.46,0.34,0.1,0.022,0.0
Initial conditions	
$P\,(PSI)$	3010.0
S_w	1.0
Well conditions	
Production	BHP control(PSI) 500
Well location	middle of the reservoir

This case study models a reservoir with a relatively soft rock in the production process with the coupling of geomechanics and reservoir simulation. The comparisons of pressure, subsidence, and the production rate are discussed. From these results, we can see a reasonable agreement between ARTS and STARS. This proves the validity of ARTS again, and shows the potential of applying ARTS in real field problems.

The block at the center of the top surface is chosen to be the check area for comparing pressure, subsidence, volumetric change in this case study. Figure 5.7 shows the comparison of pore pressure at the check area. The results from STARS and ARTS match closely and the maximum difference between ARTS and STARS is around 9%. The trend of the pressure change is the same for both simulators and it clearly shows the pressure depletion procedure after production begins. During the 300-day study period, the pressure declines as the fluid is producing from the reservoir. The reason for choosing a relatively short time in this case is to ensure the volumetric change is small and the linear poroelasticity model is used. The close match of pressures verifies the coupling scheme applied in ARTS solves the coupled system correctly. Although the match is not prefect, it is still enough to show the validity of pressure calculation in the coupled model in ARTS. The coupling scheme used is iterative coupling in STARS, and the same kind of coupling scheme is applied in ARTS.

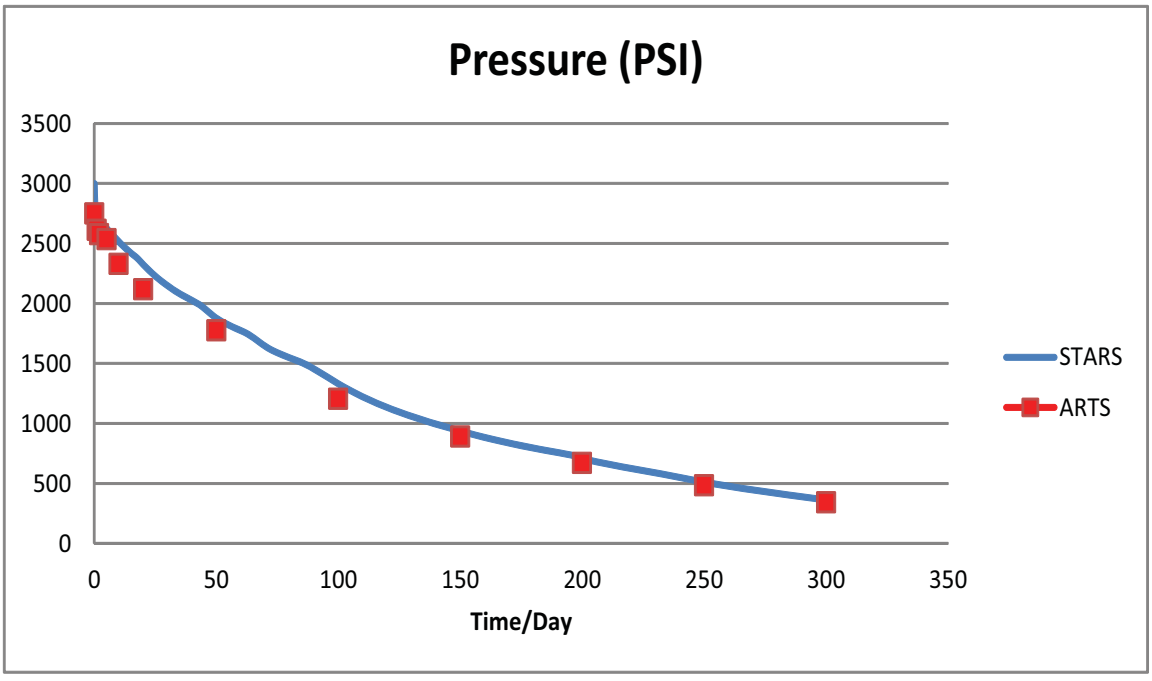

Figure 5.7: Comparison of pressure at the check area at the top of the reservoir

Figure 5.8 shows the subsidence of the check area in the reservoir. Again, agreement between ARTS and STARS is shown. The reservoir has a trend to move downwards after the production begins and the pressure starts to decline. This trend is displayed from the results from both simulators. The results for subsidence between ARTS and STARS are close but not perfectly close as shown in Figure 5.8. One possible reason is the difference for stress modeling. In ARTS, a linear poroelasticity model is applied, but an elastic plastic model is used in STARS. Although some parameters have been set to enforce the linear elasticity in STARS, the stress models in these two simulators are not the same. Despite the difference for stress models, the physical phenomenon modeled in these two simulators are the same and similar mechanical response of rocks during the production process are observed. This proves the validity of ARTS in calculating the geomechanical property change caused by pressure depletion.

Figure 5.9 and 5.10 show the comparisons of volumetric change and production rate. Again, an agreement is shown between ARTS and STARS. In STARS, the compressible force is defined as positive and sign conversion is made in ARTS to reflect this change. The volume of rock at the check area shrinks as the production begins. Both the results of ARTS and STARS capture this trend, which has a huge impact on the reservoir simulation. The agreements seen in the volumetric change and production rate show that ARTS solves the coupled system correctly.

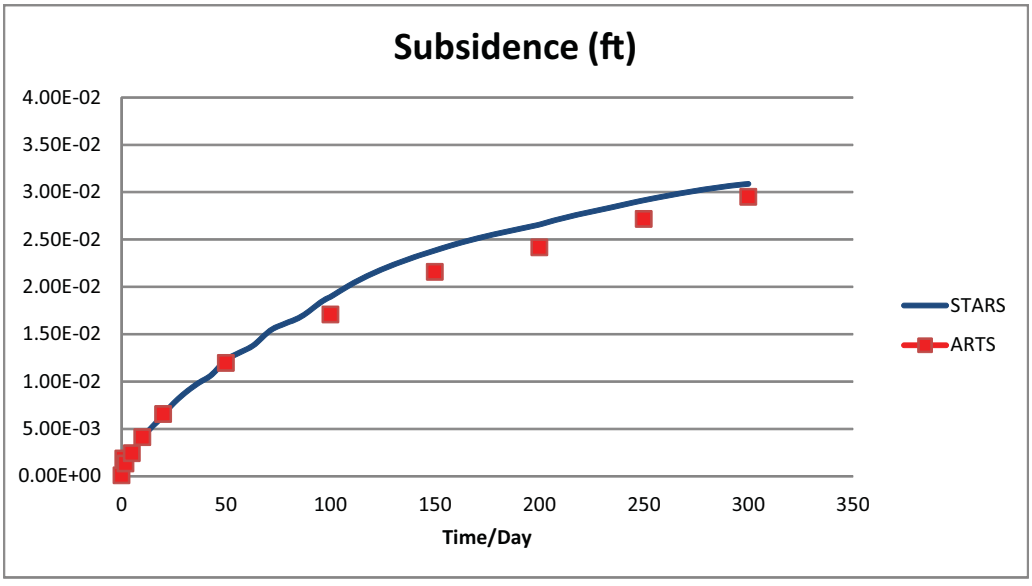

Figure 5.8: Comparison of subsidence at the check area at the top of the reservoir

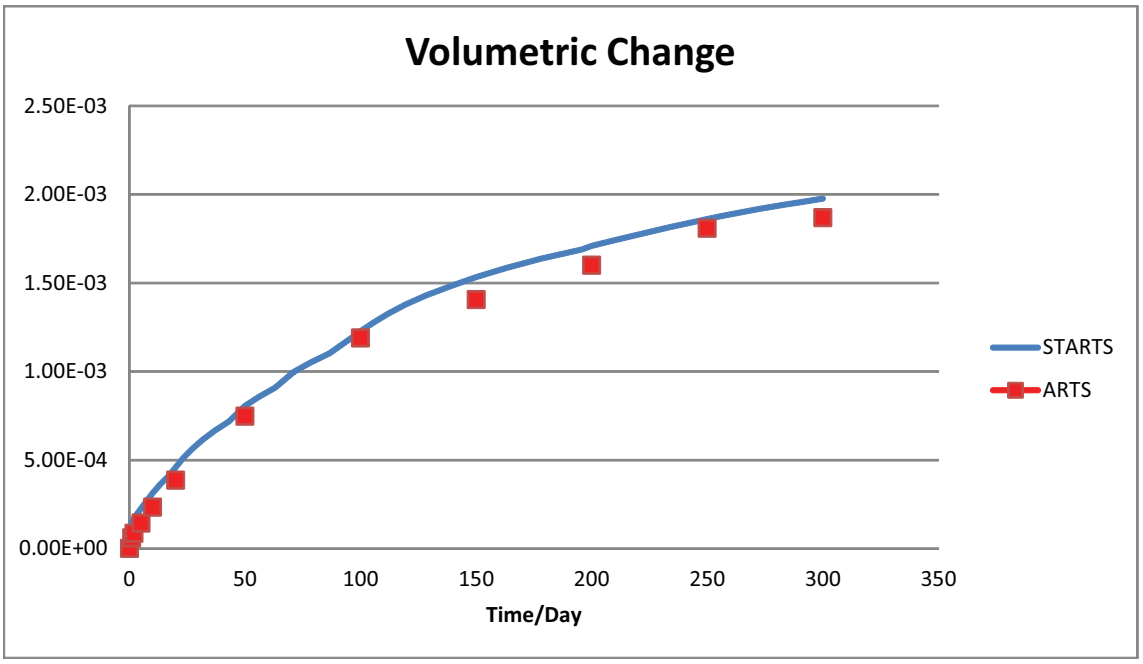

Figure 5.9: Comparison of volmetric change at the check area at the top of the reservoir

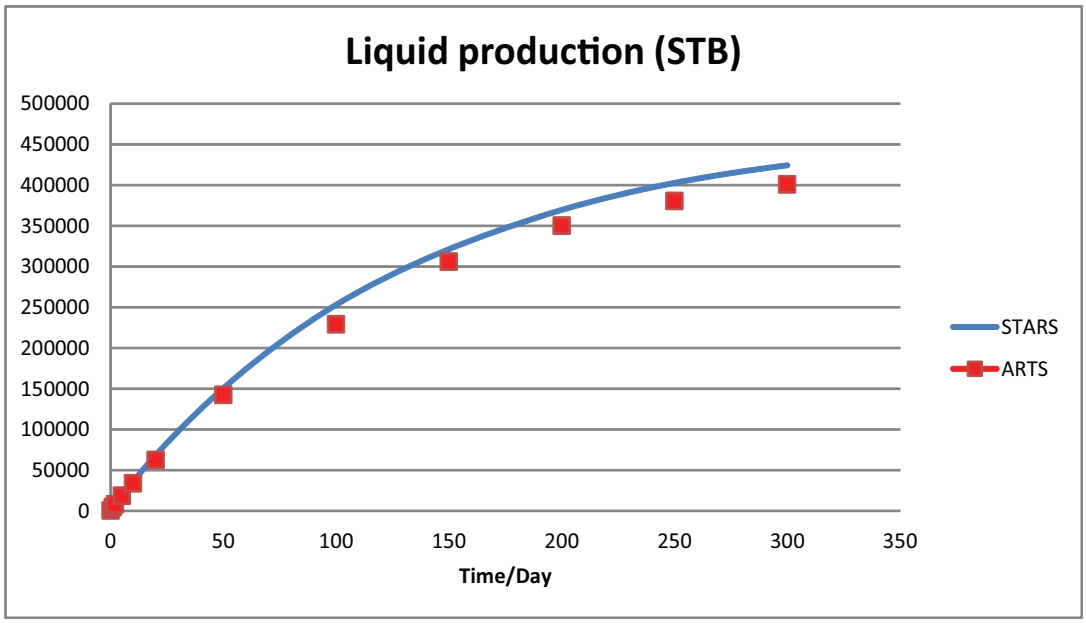

Figure 5.10: Comparison of liquid production at the check area at the top of the reservoir

Overall, the verification results between ARTS and STARS are reasonable and it shows the validity of ARTS in solving the coupled system. After a series of case studies from 1-D, 2-D, and benchmark, the conclusion can be drawn that ARTS solves the governing equations of the coupled system correctly. This is a remarkable result and shows that ARTS can be applied to solve real field problems. In order to verify and validate ARTS in a more rigorous way, validation with field data is needed. However, the case studies discussed in this chapter are enough to show the validity of ARTS as a research tool that can be safely applied to study some real field problems.

CHAPTER 6

APPLICATIONS AND PERFORMANCE EVALUATION

This chapter discusses some of the applications studied by the simulator developed in this research. The geomechanical effect is studied through these applications, and the capability of ARTS in performing reservoirs simulation with coupled geomechanics is shown.

6.1 Soft Coupling

Soft coupling scheme is created to extend the capability of ARTS in working with other geomechanical simulators. In this research, 3DEC is used as the external geomechanical simulator for obtaining geomechanical properties, then all these properties are passed to ARTS to perform reservoir simulation. In this way, the geomechanical effect is integrated in the flow simulation and the work flow of this particular scheme is showed in Figure 6.1.

In this application, the geometry of the reservoir and fractures comes from real field data with some simplifications. Initially, thousands of natural fractures were generated, but only 16 major fractures are considered in this case. Figure 6.2 shows the geometry of the reservoir. Some of the major properties are listed in Table 6.1.

The reservoir geometry and fracture location in ARTS simulation are the same with those in 3DEC simulation, and this guarantees the consistency of the geomechanical properties information between these two simulators. Three sets of simulations are studied based on the geomechanical information provided by 3DEC. The first simulation is performed without geomechanical coupling (no coupling). The second simulation (coupled case 1) is performed with identical look-up table input information based on the major fracture's aperture change from 3DEC. The third simulation (coupled case 2) is performed with various look-up tables for individual fracture set. The first simulation is designed as a reference case study, and the second simulation is designed to be the upper limit of the geomechanical impact as the geomechanical information from the fracture with the largest aperture change is used. The third simulation is set up to reflect the reality of the 3DEC simulation.

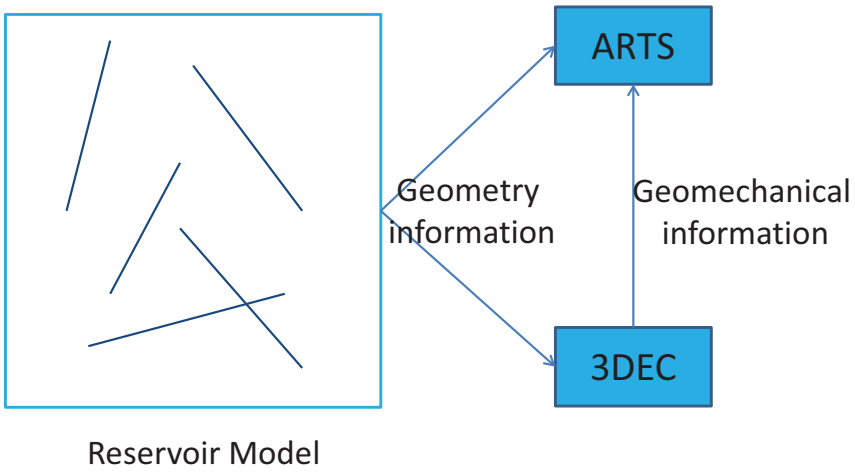

Figure 6.1: Work flow of soft coupling with 3DEC and ARTS

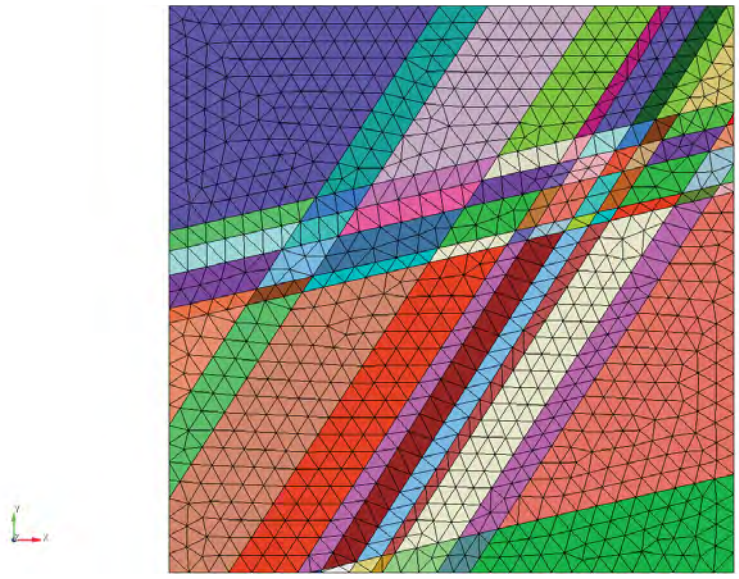

Figure 6.2: Geometry of soft coupling case study

Table 6.1: Summary of important properties of soft coupling case studies

Discretization method	CVFE	
Geometry information		
L_x, L_y, $L_z\,(ft)$	820,820,132	
Number of fractures	16	
Number of elements	40612	
Rock property		
ϕ	0.30	
Initial $k\,(mD)$ for matrix	0.001	
Initial $k\,(mD)$ for fracture	10.0	
Rock fluid data		
S_w	0.2,0.3,0.4,0.5,0.6,0.7,0.8,0.9,1.0	
kr_g	0.0,0.07,0.15,0.24,0.33,0.65,0.83,1.0	
kr_w	1.0,0.8,0.6,0.46,0.34,0.1,0.022,0.0	
Initial conditions		
$P\,(bar)$	3000.0	
S_w	0.3	
S_g	0.7	
Well conditions		
Production	BHP (PSI)	1800
Smart well	Maximum rate $(MSCF)$	2000
Well location (coordinates)	(96,49,-29)	(95,68,-26)

In Figure 6.3 and 6.4, the gas pressure and saturation distributions are displayed in a x-y plane view (no coupling). The impact of fracture network is seen in the results as the gas transport mainly happens near the fracture, and the fractures in the far field are not fully activated because the pressure depletion in that area is relatively small.

Figure 6.5 and 6.6 illustrate the gas pressure and saturation for the case (coupled case 1) in which an uniform table input is used. When comparing these figures with Figure 6.3 and 6.4, we can see the gas pressure depletion is faster and reaches more area in the reservoir if geomechanics is considered. As a result, more gas production is expected and will be discussed later. From the comparison of the pressure and saturation distribution, we can see that the geomechanical effect is an important factor for predicting production in the reservoir system with low permeability.

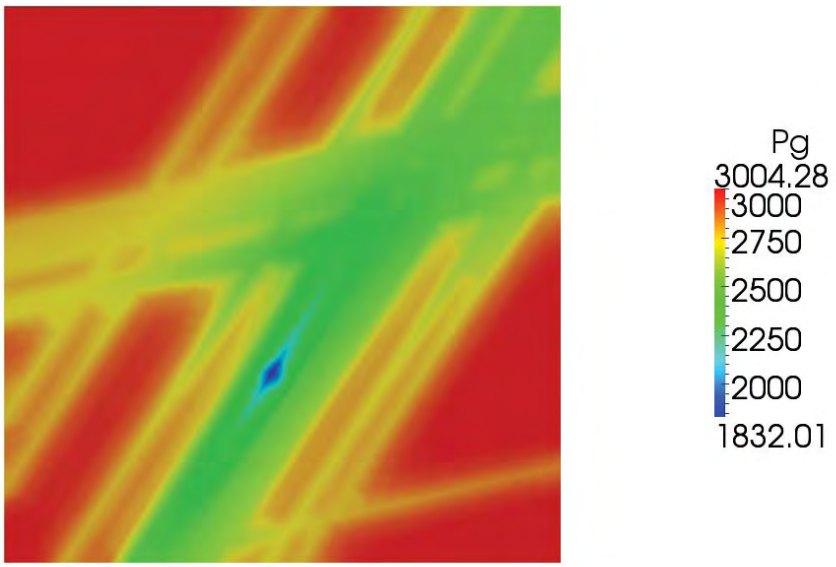

Figure 6.3: Gas pressure distribution at 1800 days for the case without geomechanical coupling

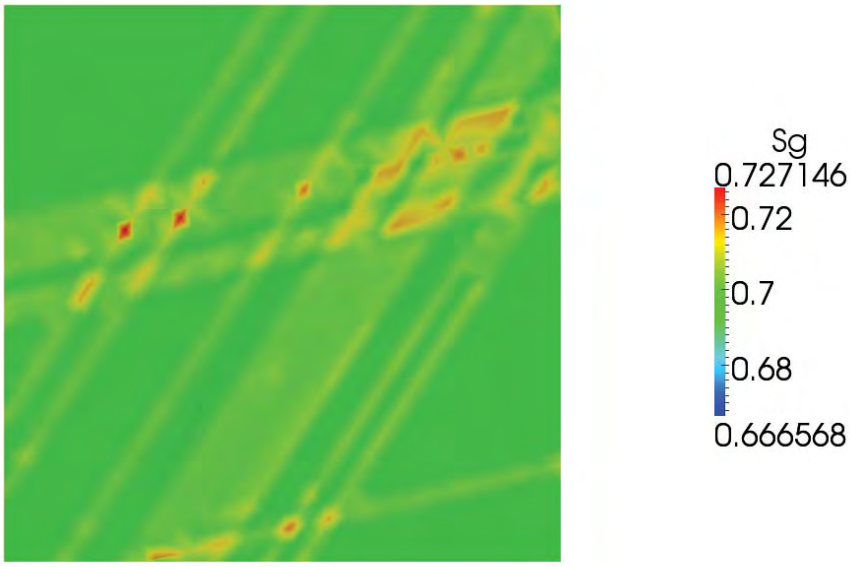

Figure 6.4: Gas saturation distribution at 1800 days for the case without geomechanical coupling

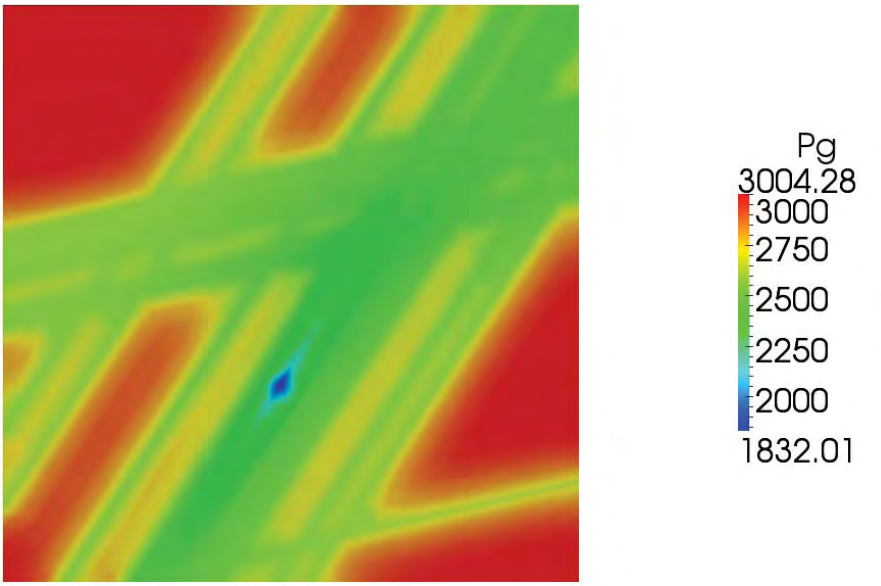

Figure 6.5: Gas pressure distribution at 1800 days for coupled case 1

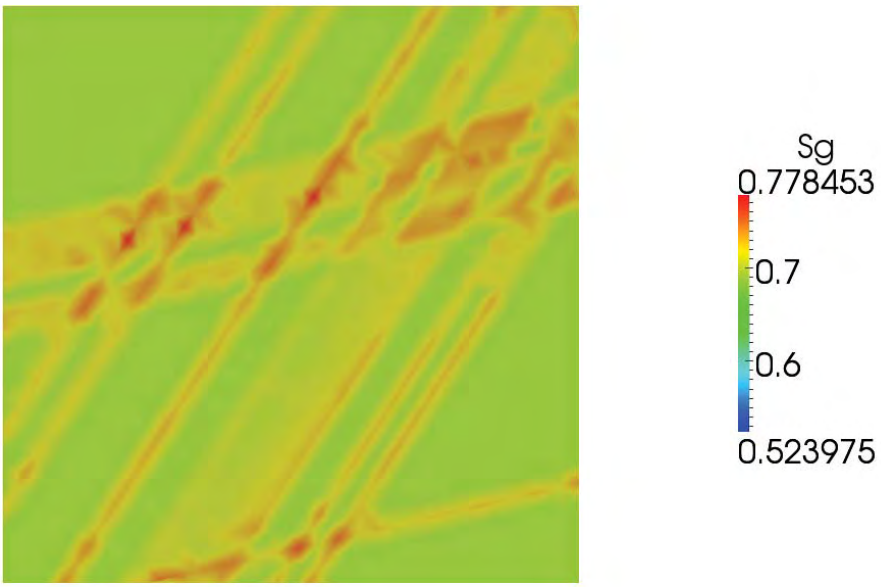

Figure 6.6: Gas saturation distribution at 1800 days for coupled case 1

In this particular case, the major conductivity path for the gas flow is the fractures, which have been modeled dynamically by using the input from 3DEC. The apertures of fractures are increasing due to the injection of hydraulic fracturing fluid in the geomechanical simulator (3DEC), and this information is integrated in the ARTS simulation by adjusting the fracture permeability. An uniform table that comes from the fracture that has the largest aperture (near the injection location in 3DEC) is applied to the whole reservoir. This brings a dramatic change to the reservoir simulation, which are shown in the gas pressure and saturation distributions. Overall, the geomechanical effect somehow enhances the gas production as the permeability increases.

Figure 6.7 and 6.8 demonstrate the gas pressure and saturation distributions for coupled case 2. In this case, various geomechanical inputs are applied to different fractures in the reservoir. In the 3DEC simulation, fractures have diverse apertures and some of the fractures in the far field have much less aperture than the major fractures near injection locations. These heterogeneous properties have been fully integrated in ARTS simulation in this case study. The gas flow is also enhanced as a result of geomechanical effect, but the enhancement is at a lower magnitude compared with coupled case 1. The less activated fractures in left corner of the reservoir (x-y plane view) are clearly showed in the gas pressure depletion figures. This case reflects the reality of the real field scenario, and less gas production than was produced in case 1 is expected.

Figure 6.9 and 6.10 clearly show the comparisons of gas production rates for these three case studies. Coupled case 1 has the largest cumulative rate, which is almost 25% more than the case without geomechanical coupling. The gas production from coupled case 2 is less than coupled case 1, but is still about 7% more than the case without geomechanical coupling. The instant rate shows the same trend, and it also shows the well control method changing as a result of smart well control module designed in ARTS.

In this application, the geomechanical effect is a key factor. Enhancement of gas production is observed from the comparisons of the three case studies. We can conclude that the increased permeability in the fractures is important for gas production, but this effect may differ as fractures have different mechanical responds to the hydraulic fracturing process.

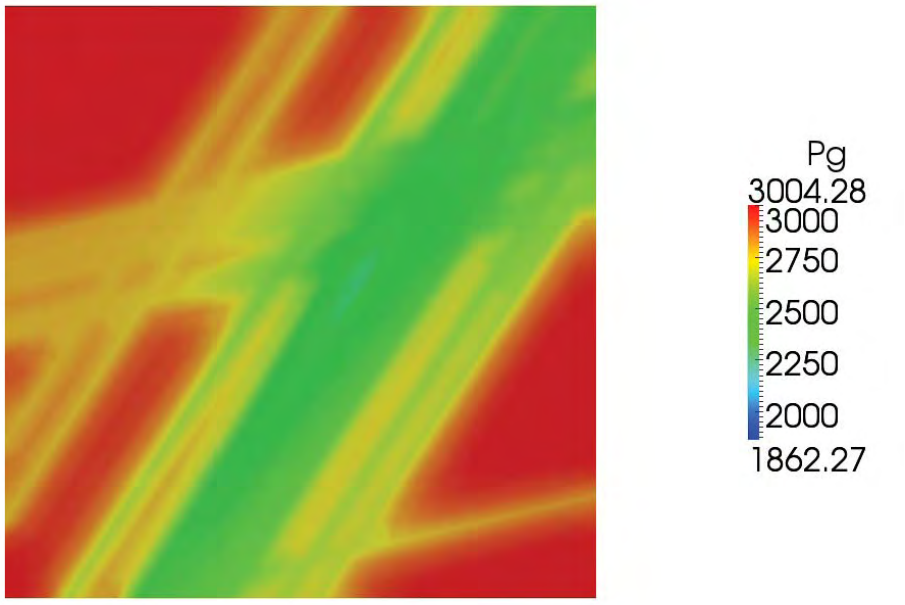

Figure 6.7: Gas pressure distribution at 1800 days for coupling case 2

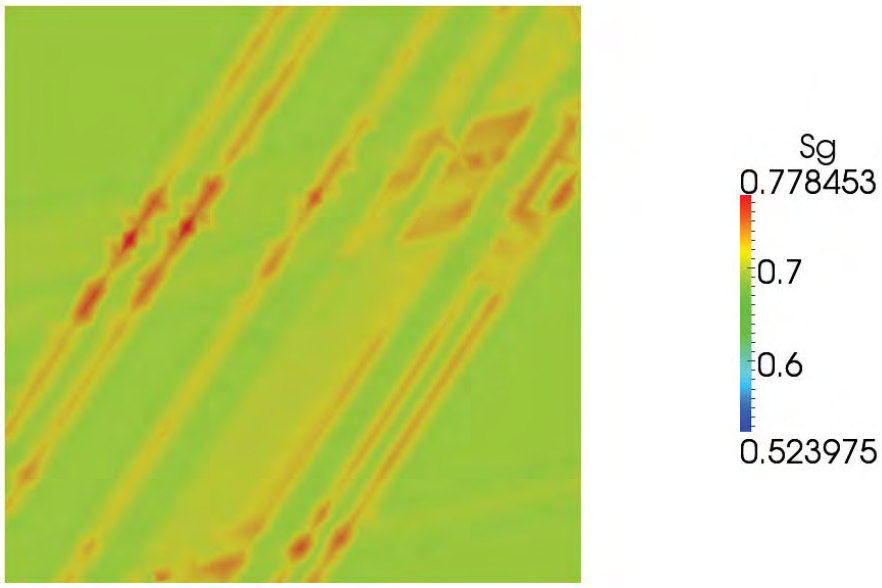

Figure 6.8: Gas saturation distribution at 1800 days for coupling case 2

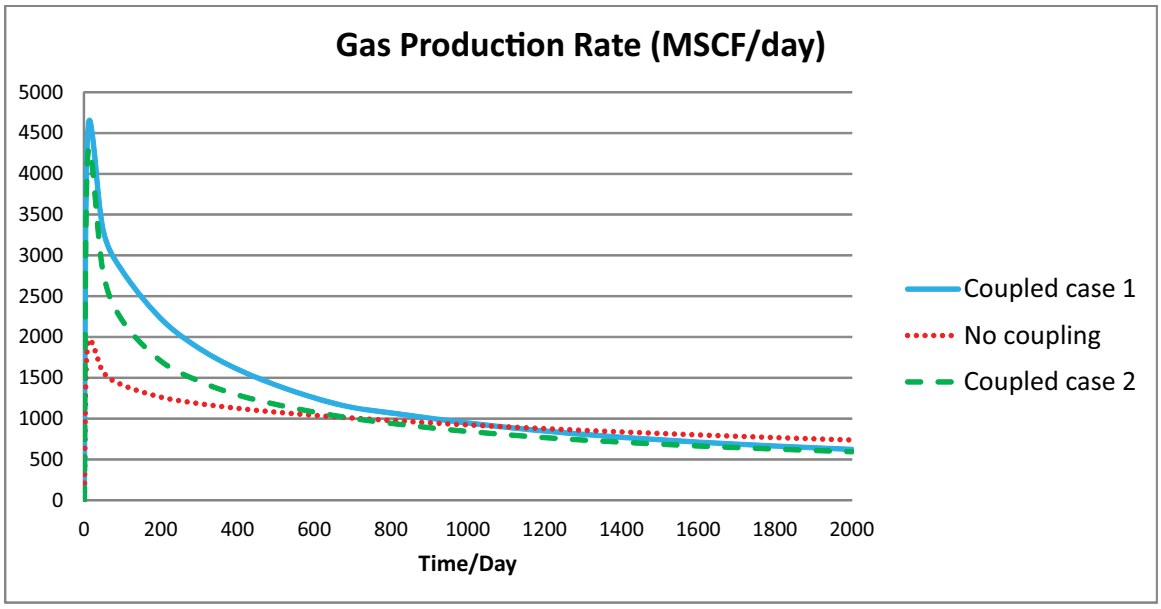

Figure 6.9: Gas production rate for soft coupling case study

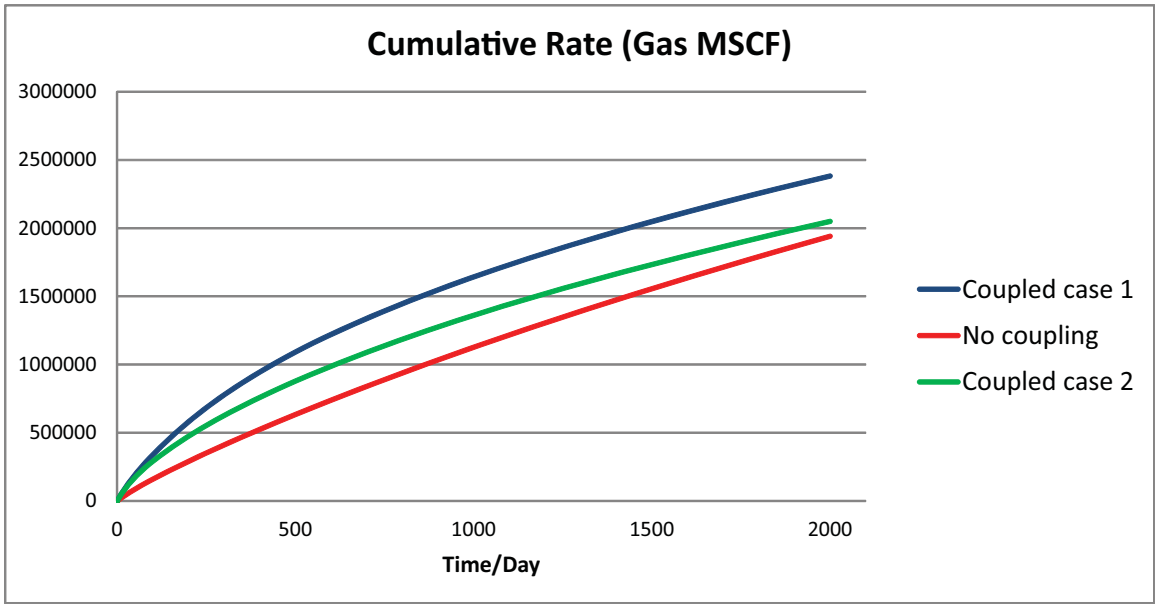

Figure 6.10: Cumulative gas production for soft coupling case study

Overall, soft coupling is a powerful tool which has almost the same computational cost as a conventional reservoir simulation. Furthermore, the effect of proppant can be simulated by using the soft coupling scheme. If we have knowledge of where the proppant goes, the fracture containing the proppant can be assumed to have some minimal permeability, which is implemented in the look-up table in ARTS. In this way, the reservoir simulation would reflect the impact of proppant. A demonstration case study of this kind of application is discussed later.

In order to show the impact of proppant, another case study is performed with soft coupling scheme. The same fluid properties and geometry information are used as the previous application, but the number of fractures and the well control method are changed. The properties and parameters used in this case study are summarized in Table 6.2.

Table 6.2: Summary of important properties of case study for the influence of proppant

Discretization method	CVFE	
Geometry information		
L_x, L_y, $L_z\,(ft)$	820,820,132	
Number of fractures	20	
Number of elements	46449	
Rock property		
ϕ	0.30	
Initial $k\,(mD)$ for matrix	0.1	
Initial $k\,(mD)$ for fracture	100.0	
Initial conditions		
$P\,(PSI)$	3000.0	
S_w	0.3	
S_g	0.7	
Well conditions		
Production	BHP (PSI)	1000
Smart well	Constant BHP (PSI)	1000
Location (Coordinate)	(164,-46,-66)	

Figure 6.11 to 6.13 illustrate the effect of proppant on the gas production. As shown in those figures, we can see that production declines slowly when the proppant exists in certain fractures. The two major fractures with proppant can be identified from the comparison of Figure 6.11 and 6.12. This case study clearly shows the effect of proppant and the potential capability of the soft coupling scheme.

In summary, the soft coupling scheme are applied to a series of case studies to learn the geomechanical effect in the reservoir simulation. This coupling scheme is a powerful tool with a good running speed. But, it is still an approximation of the geomechanical effect, and the decoupled approach may not be appropriate in certain conditions. As a result, the hard coupling scheme is developed in ARTS, and some of the applications using that method are discussed in the following sections.

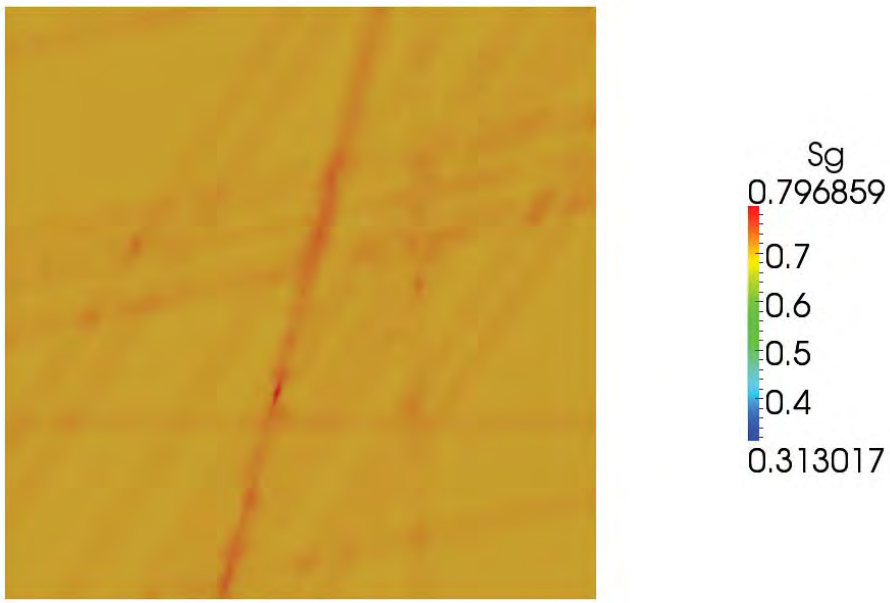

Figure 6.11: Gas saturation distribution for the case without proppant

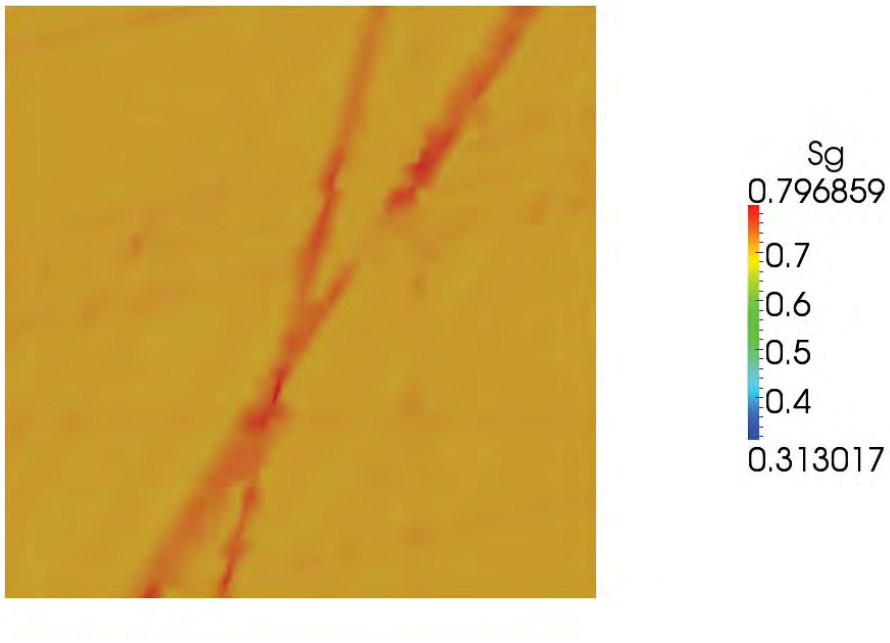

Figure 6.12: Gas saturation distribution for the case with proppant

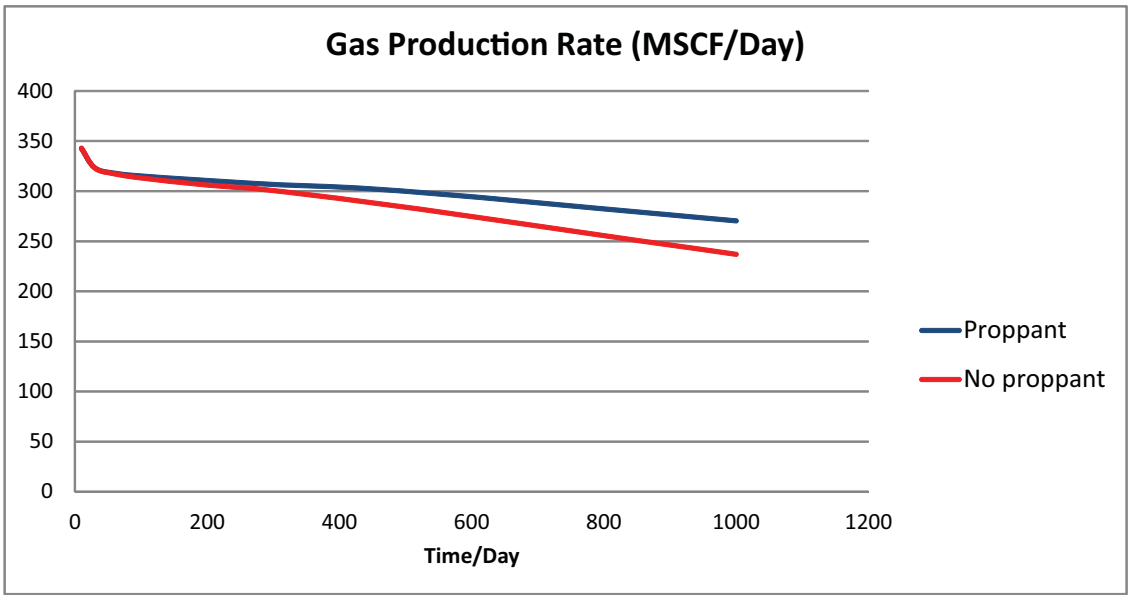

Figure 6.13: Gas production rate for case studies with and without proppant

6.2 Production Problem

During the production process, the permeability and the porosity changes as the pore pressure depletes. These changes may dramatically alter the reservoir behavior and potentially change the production. For example, field observations show that the injected fluid cannot be totally reproduced after hydraulic fracturing process. The geomechanical effect and natural fracture networks are considered to be the possible reasons. With the capability of coupling geomechanics, ARTS is applied to study the geomechanical effect during the production process in a reservoir.

6.2.1 Gas Production from Low Permeability Reservoirs

The first case studied is a gas production problem in a reservoir with three major hydraulic fractures. The goal for this cast study is to learn the general impact of geomechanics in producing gas in an extremely low permeability reservoir. Some of the important reservoir properties used in the simulation are listed in Table 6.3.

In this case study, different mechanical properties of rock are applied to study the importance of each parameter. The magnitude of Young's modulus is a measure of the stiffness of the material and it is an important parameter to determine how the material deforms under external force. In this case study, two values of Young's modulus are selected, the case with a relatively large Young's modulus ($1e7\ PSI$) represents the reservoir filled with stiff rock, which is hard to deform, and the case with a relatively small Young's modulus ($1e5\ PSI$) represents the reservoir filled with soft rock, which is easy to deform. Through these two cases, the impact of Young's modulus on the gas production can be understand, and it may provide some valuable guidance to avoid some unexpected incidents in field operations.

The second mechanical parameter variation is the Poission's ratio, which is a measure of the Poisson's effect. This effect refers to the physical phenomenon that a material tends to expand in directions other than the direction which has a compressive force. The reservoir is assumed to be isotropic and obeys the linear poroelastic constitutive relationship in ARTS, hence the Poission's ratio is usually assumed to be positive and not greater than 0.5. Two values (0.2 and 0.35) are applied in this case study. The impact of the variation of this parameter is discussed later. Generally speaking, a larger Poission's ratio should reduce the volumetric change of the reservoir and hence reduces the coupling effect. The reason is that a larger Poission's ratio induces a larger transverse strain which may offset the compressive strain caused by production and make the volume unchanged overall.

Table 6.3: Summary of important properties of case study for gas production

Discretization method	CVFE	
Geometry information		
L_x, L_y, $L_z\,(ft)$	800,800,200	
Number of fractures	3	
Number of elements	21746	
Rock property		
ϕ	0.10	
Initial $k\,(mD)$ for matrix	0.001	
Initial $k\,(mD)$ for fracture	10.0	
Pore compressibility $\left(\frac{1}{psi}\right)$	4.0E-6	
Biot coefficient	1.0	
Young's modulus (psi)	1e5,1e7	
Poisson's ratio (psi)	0.2,0.35	
Rock density $\left(\frac{lb}{ft^3}\right)$	156.0	
Initial conditions		
$P\,(PSI)$	3500.0	
S_w	0.5	
S_g	0.5	
Boundary conditions		
Top surface load	P (PSI)	0,6000
Top surface displacement	u (ft)	Not confined
Bottom surface displacement	u (ft)	0
Left surface displacement	u (ft)	0
Right surface displacement	u (ft)	0
Front surface displacement	u (ft)	0
Back surface displacement	u (ft)	0
Well conditions		
Production	BHP (PSI)	1000
Smart well	Constant BHP (PSI)	1000
Location (Coordinates)	(200,380,100)	
	(400,380,100)	
	(600,380,100)	

Another parameter that varies in this case study is the surface load. The surface load induced by gravity is assumed to be zero as the incremental formulation is applied in ARTS. In order to artificially increase the deformation in the vertical direction, a surface load at time $t = 0^+$ is applied to see how the reservoir behavior changes. It should be noticed that the surface load is generally assumed to be zero in most case studies discussed in this thesis.

In this case study and other case studies discussed later, an iterative coupling schemes is applied by default. This scheme has been verified and has been used in the industry as a standard. Although other types of hard coupling schemes are also developed in ARTS, only the iterative scheme is applied for case studies discussed in this chapter. Some results from the simulation are discussed and a primary conclusion of the geomechanical impact on gas production is drawn.

Figure 6.14 shows the gas pressure distribution without geomechanical coupling after 1800 days of production. The pressure depletion zone is near the fracture and the minimal pressure in the reservoir is 1300 PSI. Figure 6.15 shows the gas pressure distribution after 1800 days of production with geomechanical coupling (the reservoir is filled with stiff rock). we can see the minimal pressure in the reservoir is 1500 PSI. Figure 6.16 shows the gas pressure distribution after 1800 days of production with geomechanical coupling (the reservoir is filled with soft rock). The minimal pressure in the reservoir is 1450 PSI in this case.

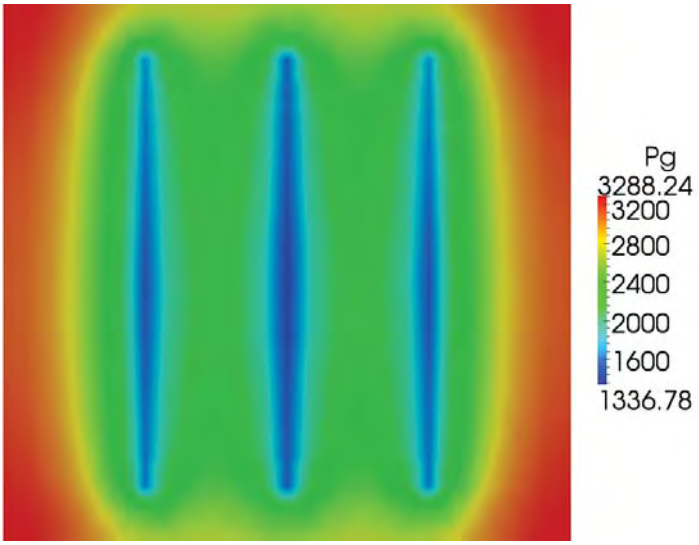

Figure 6.14: Gas pressure distribution at 1800 days without geomechanical coupling

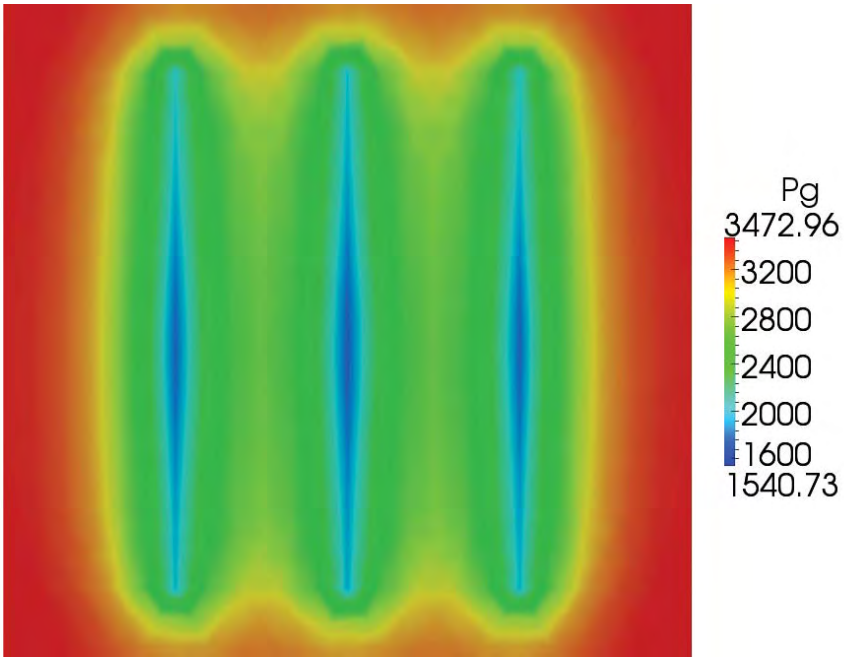

Figure 6.15: Gas pressure distribution at 1800 days with geomechanical coupling (stiff rock)

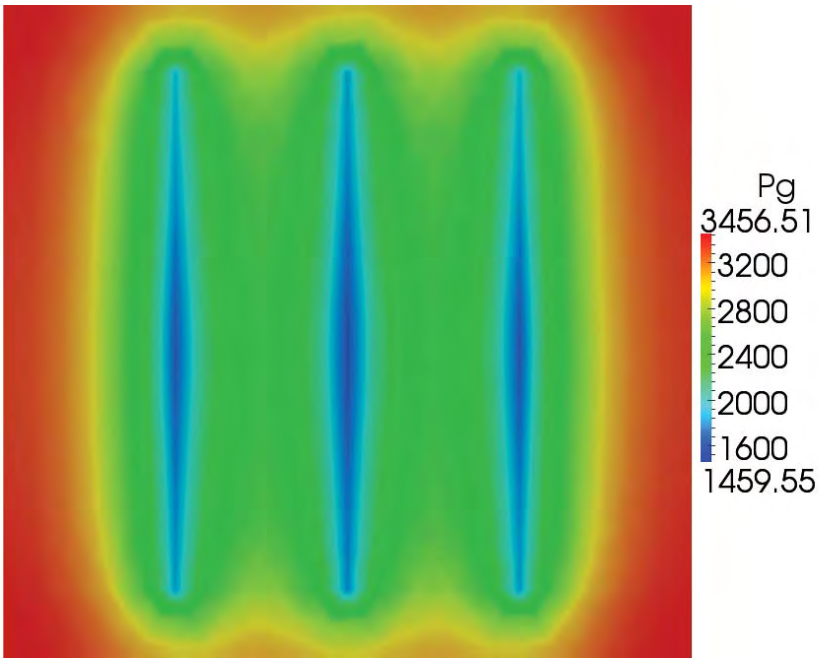

Figure 6.16: Gas pressure distribution at 1800 days with geomechanical coupling (soft rock)

From the comparison of the gas pressure distribution in Figures 6.14 to 6.16, we can see the geomechanical coupling has a huge impact on the pressure depletion of the reservoir. The pressure solution of the reservoir is increased as the geomechanics is coupled, and it seems that the pressure increases most in the reservoir with stiff rock. This dramatically changes the pressure distribution and is supposed to have significant impact on the saturation distribution and the gas production. The reason for this is not trivial, but the geomechanical coupling does impact the reservoir. Some possible reasons are discussed later.

Figure 6.17 shows the gas saturation distribution for the uncoupled case after 1800 days of production. The major region having gas flow is the area near the fractures. The maximal gas saturation is around 0.59. Figure 6.18 shows the gas saturation after 1800 days of production for the coupled case (the reservoir is filled with stiff rock). The maximal gas saturation in the fracture is around 0.55. Figure 6.19 shows the gas saturation for the coupled case (the reservoir is filled with soft rock) after 1800 days of production. The maximal gas saturation in the fracture is around 0.56. The gas saturation distributions are also changed due to the geomechanical coupling and this phenomenon has the potential to dramatically impact gas production.

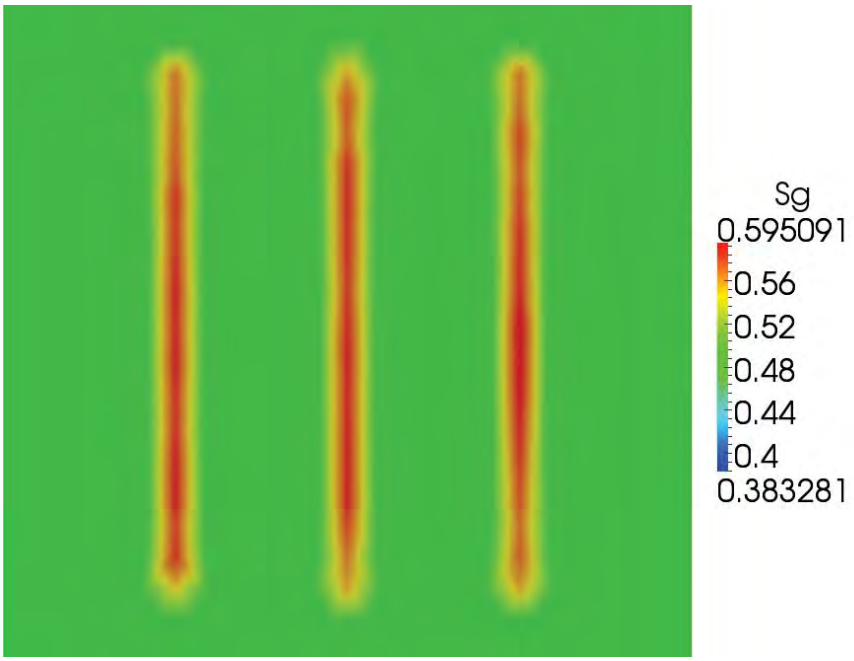

Figure 6.17: Gas saturation distribution at 1800 days without geomechanical coupling

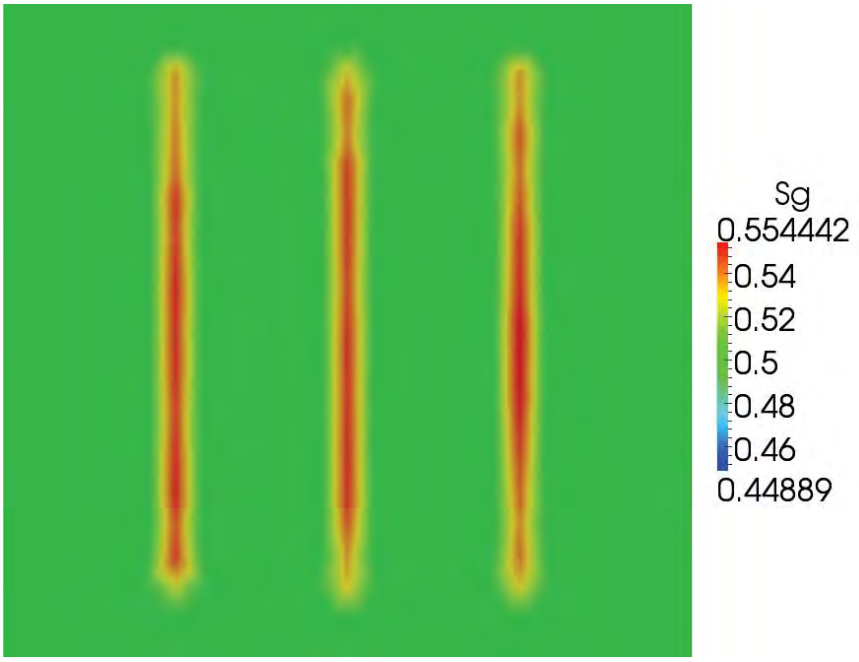

Figure 6.18: Gas saturation distribution at 1800 days with geomechanical coupling (stiff rock)

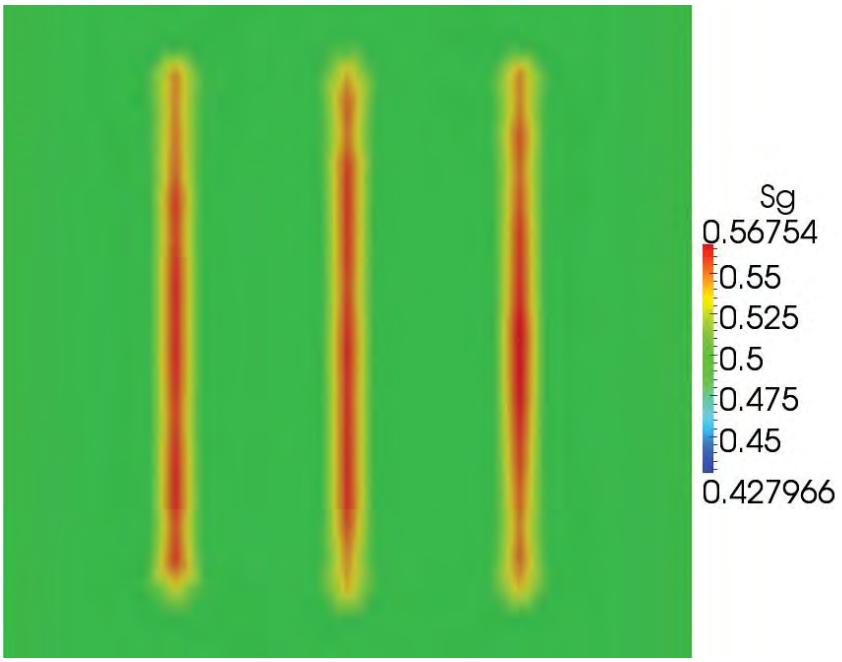

Figure 6.19: Gas saturation distribution at 1800 days with geomechanical coupling (soft rock)

As shown in Figures 6.14 to 6.19, the conclusion that geomechanical coupling is significant in reservoir modeling, can be drawn. The Poisson's ratio is 0.2 and the surface load is zero in all cases discussed above. In the geomechanical coupling process in ARTS, both the porosity and the permeability are updated based on the geomechanical model, and hence the geomechanical impact is mainly from variations of permeability and porosity. It should be noticed that the update of permeability is through the "transmissibility multiplier"in ARTS, and this is a unique feature because most reservoir simulators can not easily updated permeability. With this capability, ARTS has the advantage to learn the geomechanical effect in an accurate manner. As a result of the variation of pressure seen in the pressure distribution figures, the production is expected to be different for the three case studies discussed.

Figure 6.20 shows the comparison of instant gas production rate for uncoupled case, coupled case (stiff reservoir) and coupled case (soft reservoir). The comparison of cumulative gas production is shown in Figure 6.21. In these figures, we can see the geomechanical coupling dramatically changes the gas production, and the impact on production is positive in this case study. The soft rock seems to have larger geomechanical effect as the pressure declines and the resulting production curve varies more dramatically during the production process. In the reservoir with stiff rock, relatively small changes are seen in instant production rates until 1000 days of production. Figure 6.22 shows the volume and permeability change of reservoir with stiff rocks at 1800 days.

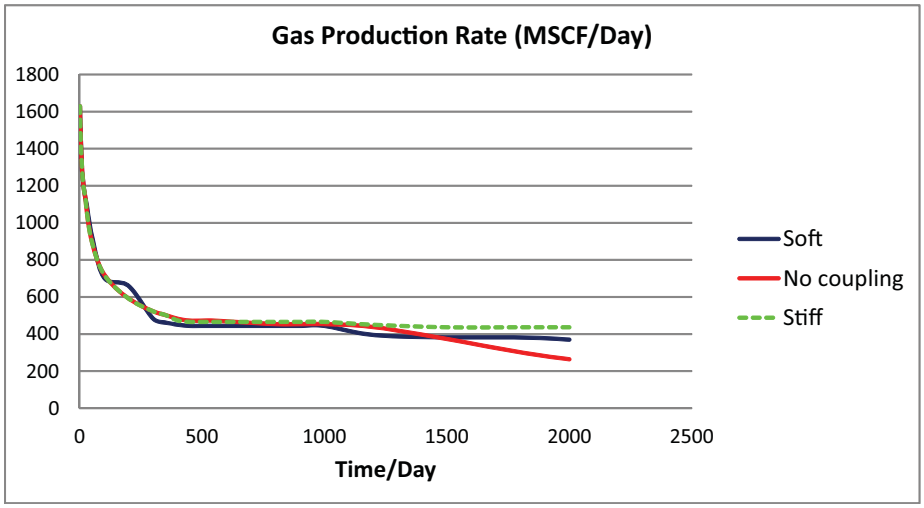

Figure 6.20: Gas production rate comparison (no coupling, soft rock, stiff rock)

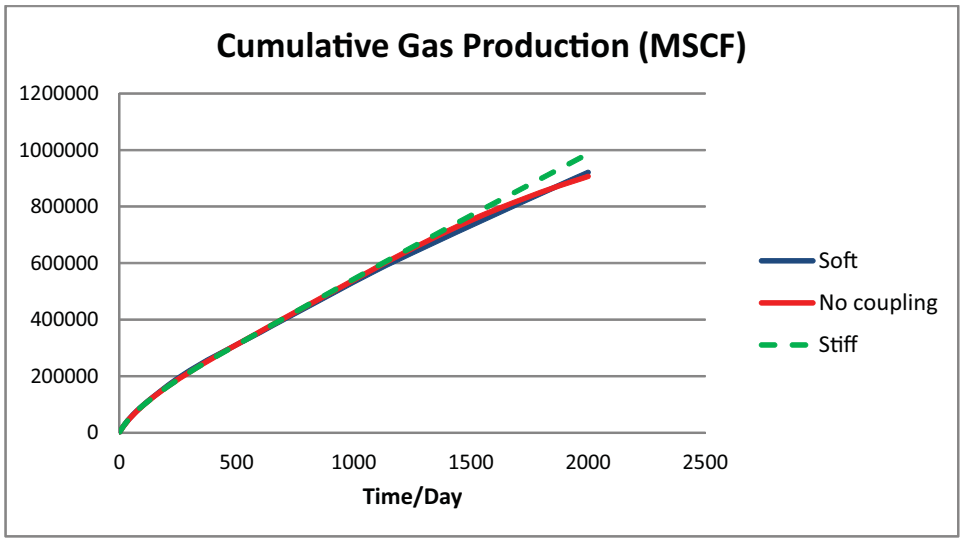

Figure 6.21: Cumulative gas production rate comparison (no coupling, soft rock, stiff rock)

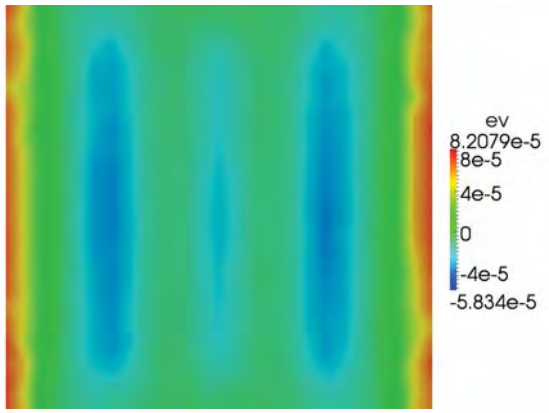

(a) Volumetric change

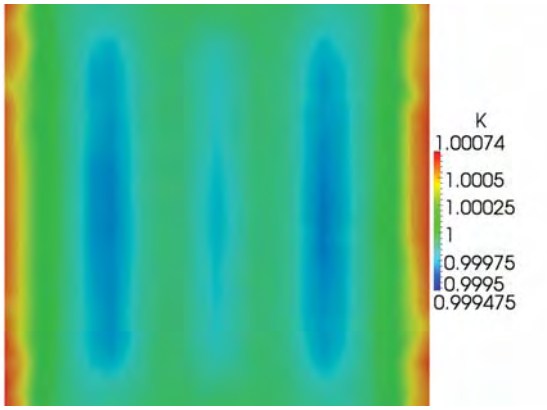

(b) Change of permeability $\frac{K}{K_0}$

Figure 6.22: Volume and permeability changes at 1800 days (stiff rock)

The volume and permeability changes in the stiff reservoir are relatively small, but these smaller changes in the geomechanical properties do cause huge changes to the reservoir production as shown in the instant and cumulative production curves. The geomechanical properties change in a larger scale in the soft reservoir, and the results are shown in Figure 6.23. We can see that permeability reduced to 94.9% in the fracture in the soft reservoir compared with 99.9% in the stiff reservoir. The permeability change is a linear function of volumetric change and the distributions of those two are similar. The production well is located at the center of each fracture and we can see that the production of gas causes a reduction in volume and permeability in the reservoir area near the producing fractures. The different simulation results of soft and stiff reservoirs shown above indicate the impact of Young's modulus. This is discussed further when the results of parameter variation case studies are shown.

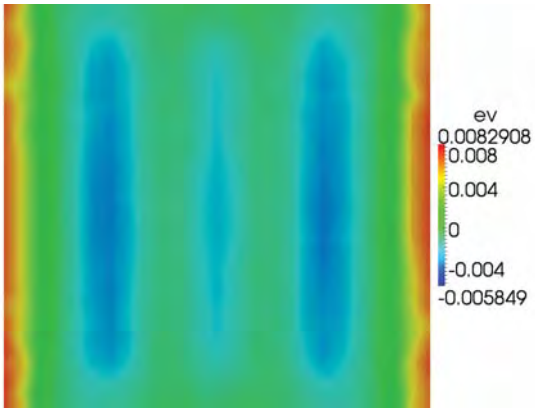

(a) Volumetric change

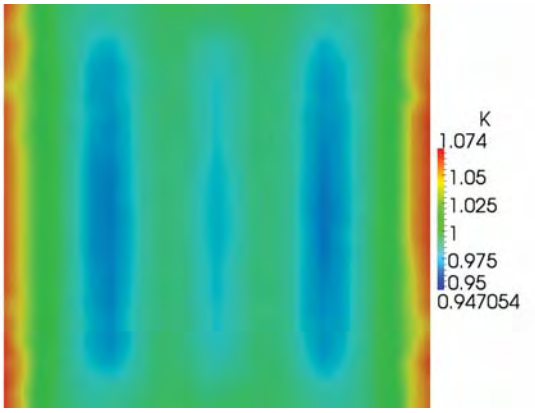

(b) Change of permeability $\frac{K}{K_0}$

Figure 6.23: Volumetric and permeability changes at 1800 days (soft rock)

The influence of geomechanical coupling is significant as seen in this case study. Some possible reasons are proposed as an illustration of the physical phenomenon behind the simulation results. First, the pressure is increased if geomechanical coupling is applied as shown in the gas pressure distribution comparisons. This should have a positive impact on the production because the pressure difference between the well and the reservoir is increased. The reason for the increased pressure is possibly the decrease of the pore volume. This hypothesis is not trivial to illustrate as the system is coupled, but we can take a example in a simple system. Assuming that some fluid is stored in a close container and the volume of the container is somehow reduced as a result of external force, the pressure of the fluid should increase as a result of the shrinking space in the container. The reason for increased pressure in coupled simulation is not as simple as what is described above because the complexity of the multiphase fluid flow system in the reservoir. The impact of shrinking volume inducing higher pressure should be observed in the reservoir.

In order to illustrate the phenomenon of increased pressure further, the average reservoir pressures are compared in Figure 6.24. The average pressure in the reservoir is clearly displayed and we can see that the geomechanical coupling does increase the pressure in the reservoir. The stiff reservoir has the largest average reservoir pressure, the reservoir without geomechanical coupling has the smallest average pressure. However, the reuslt, which shows that the soft reservoir has a smaller average pressure (larger volume change) than the stiff reservoir, may invalidate the hypothesis discussed above. This question actually leads to the second hypothesis which is related to the permeability variation.

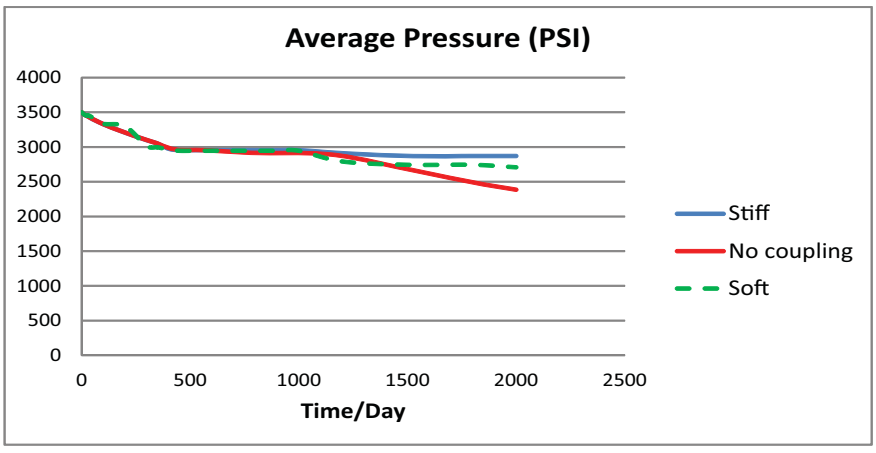

Figure 6.24: Average pressure in the reservoir (no coupling, soft rock, stiff rock)

The second possible reason for the production variation in coupled case study is related to the permeability modification during the production process. As shown in Figures 6.22 and 6.23, the permeability of the reservoir is decreasing during the production, and it has a negative impact on the production. Hence, the decreased permeability has a reverse impact on gas production compared with the decreased volume and the final simulation results show there is a complicated relationship between permeability and volume changes when predicting gas production with coupled geomechanics. Indeed, the reduced permeability also has an impact on the reservoir pressure as the conductivity of fluid flow is changed in the reservoir. This may have positive or negative influence on the production. So the combination effect of volume and permeability changes determines the overall geomechanical coupling effect. The relationship between these two factors is complicated as each individual factor may be positive or negative to gas production .In summary, the geomechanical effect is really a result of the coupled effect and it is hard to quantitatively learn the impact of each parameter separately. However, the hypothesis stated here is that the geomechanical effect on the reservoir behavior (production, pressure, etc.) is a result of the complex combination effect between the volume and permeability changes of the reservoir.

In order to illustrate the complex relationship between volumetric change and permeability change on gas production, several case studies is performed by artificially update only one term (permeability or porosity) during the coupling process. With the same properties and geometry as the case studies discussed above, four additional simulations are studied:

- Case 1: Geomechanical coupling only with updated porosity in soft reservoir
- Case 2: Geomechanical coupling only with updated permeability in soft reservoir
- Case 3: Geomechanical coupling only with updated porosity in stiff reservoir
- Case 4: Geomechanical coupling only with updated permeability in stiff reservoir

The comparisons of average pressure and instant gas production rate of these cases and the baseline cases (both permeability and porosity are updated) are shown in Figure 6.25 and 6.26. In the average pressure comparison, we can see that the pressure change for case 3 is almost the same with the baseline case (stiff reservoir). This means that the porosity modification does have a huge impact on the pressure solution. The results for soft reservoir shows the same trend. From the average pressure curves of case 2 and case 4, we can see that reducing permeability also helps to increase the reservoir pressure. The

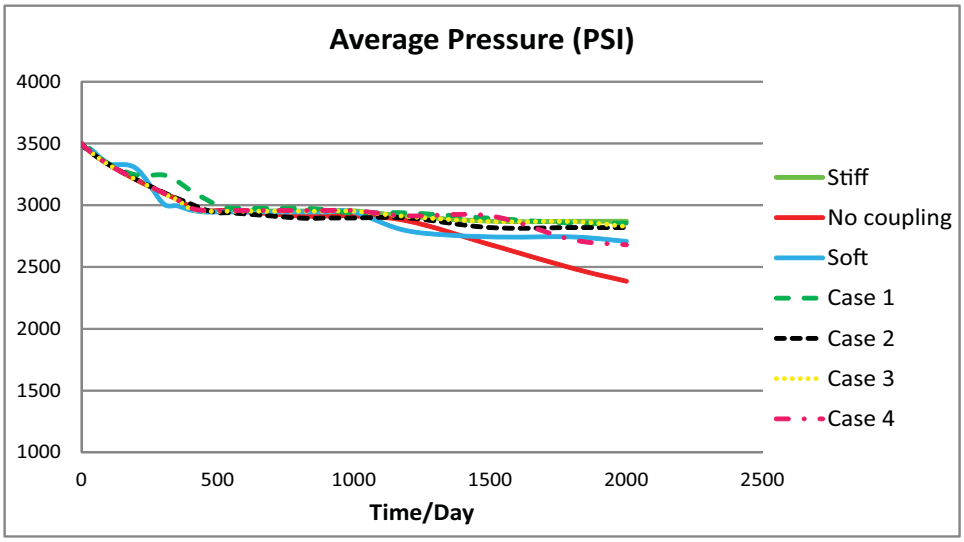

Figure 6.25: Average pressure comparison for case studies on the impact of changing volume and permeability

instant production curve reflects a similar trend which shows the impact of permeability and porosity updating. These results confirm the hypothesis discussed above, but also indicate that the coupled effect is not a simple linear combination of the effects caused by volume and permeability changes.

From the results discussed, we can see that the geomechanical coupling (with updated porosity and permeability) does have a huge impact on the reservoir simulation. The complex combination effect of the changes of volume and permeability decides the overall impact of geomechanical coupling on gas production. In this particular case study, the geomechanical effect acts as a positive factor for production, but it may be a negative factor in certain conditions. For example, if the reduction of permeability is large enough to significantly block most of the fluid flow paths in a reservoir, the production is expected to be less. In this research, the infinitesimal strain theory which assumes a small volumetric strain is applied, and the permeability reduction cannot be very large. Hence the geomechanical effect is a positive factor for production in most case studies.

As mentioned in the beginning of this section, the variation studies are performed to learn the effects of some parameters that govern the geomechanical model implemented in the research. The Young's modulus, Poission's ratio and the surface load are varied to learn the impact of each individual parameter. Some of the cases studied are listed in Table 6.4.

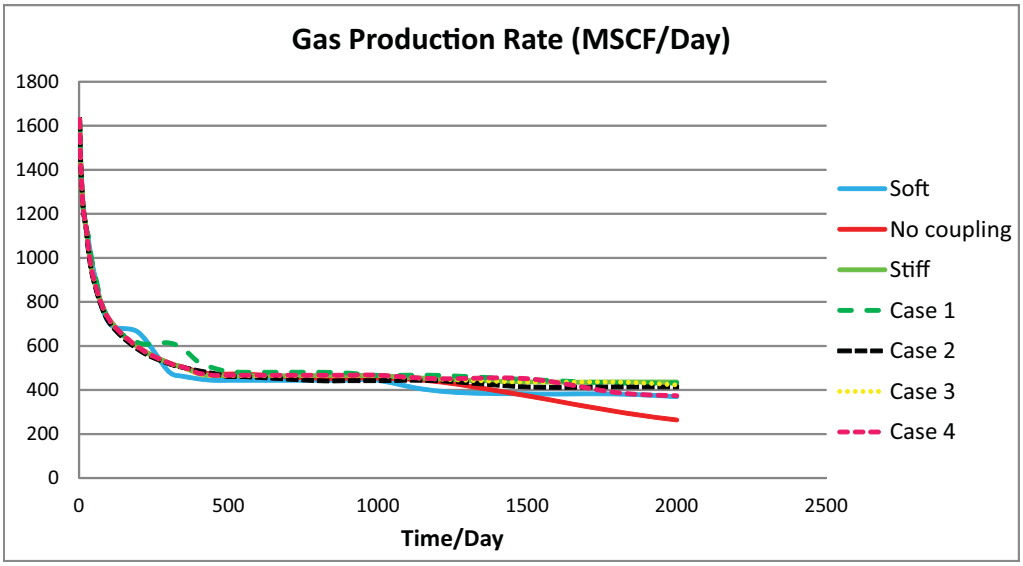

Figure 6.26: Gas production rate comparison for case studies on the impact of changing volume and permeability

Table 6.4: List of case studies for variation of geomechanical parameters

Case name	Young's modulus (PSI)	Poission's ratio	Surface load (t^+, top,PSI)
Case A	1e7	0.2	0,0,0
Case B	1e7	0.35	0,0,0
Case C	1e5	0.2	0,0,0
Case D	1e5	0.35	0,0,0
Case E	1e7	0.2	0,0,6000
Case F	1e7	0.35	0,0,6000
Case G	1e5	0.2	0,0,6000
Case H	1e5	0.35	0,0,6000

Case A and case C are the cases for stiff and soft reservoirs discussed above. These parameter variation case studies can illustrate the general impact of each parameter to the geomechanical model and hence to the reservoir model. The reservoir geometry and other properties are the same with previous case studies and are listed in Table 6.3. As discussed before, the geomechanical parameter is vital for the calculation of volumetric change in the reservoir. The purpose of this case study is to understand the impact of each individual

parameter and this can also help to test the stability of the framework.

The results from case studies listed in Table 6.4 are compared and some primary conclusions regarding the impact of individual parameters are drawn. The parameter applied in this case study is not based on the real field data and some parameters such like surface load are not usually defined in most simulations. After this study, the parameter of geomechanical model is fixed in case studies discussed in the following sections.

Figure 6.27 shows the comparison of volumetric change near fracture in the plane where the production well is located. we can see that the magnitudes of volume changes are different as the Young's modulus varies from $1e7$ to $1e5$, but the distribution of the volume change does not vary significantly. This means the mechanical change of the reservoir with respect to pressure change is mainly determined by Young's modulus. The variation of Poission's ratio alters the distribution of volumetric changes, and we can see the difference of volume change area in the reservoir from the result. The magnitude of volume change does not vary much. This means the Poission's ratio mainly determines the distribution of displacement and hence volumetric change in the reservoir.

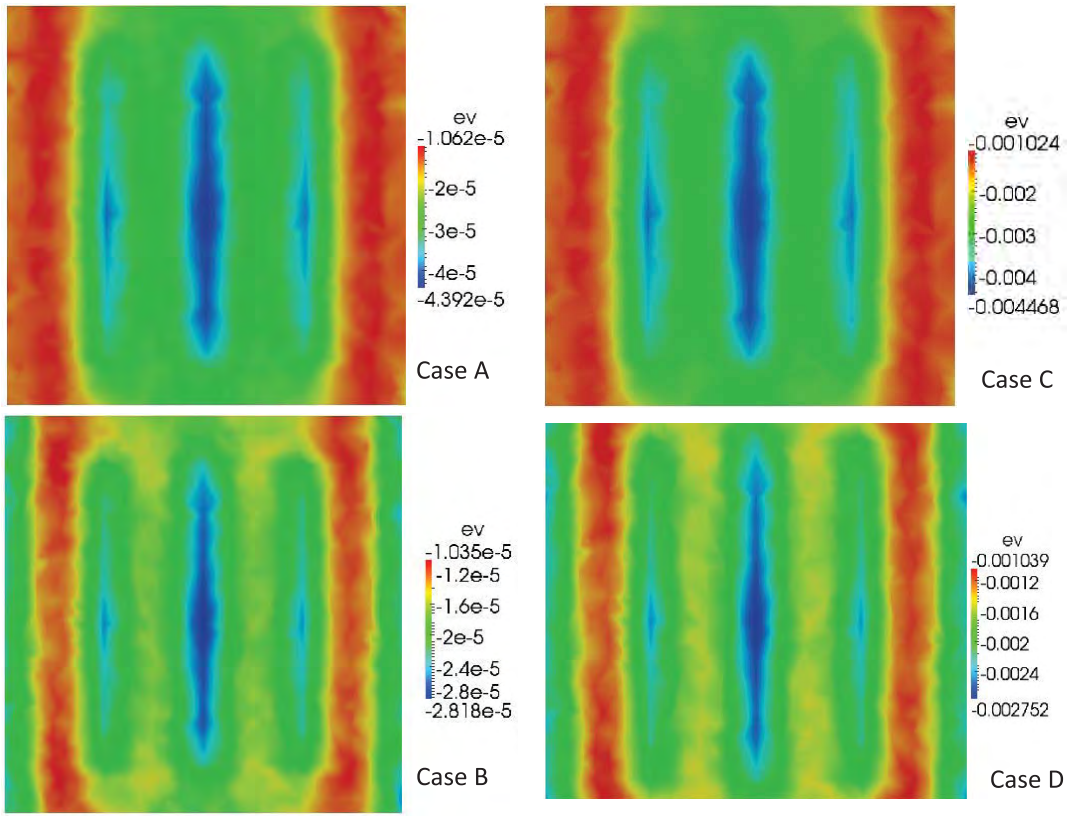

Figure 6.27: Comparison of volumetric change near fractures for case A, B, C and D

From the result of volume change comparison of case A, B, C and D, the impact of Young's modulus and Poission's ratio can be illustrated. But, each individual parameter is related to other parameters used in the coupled system of geomechanical model and reservoir model, and it is hard to identify the influence of an individual parameter. The case study performed here is just a primary illustration of the impact of some parameters used in the coupled simulation, and it would help to understand the geomechanical coupling effect in reservoir simulation and the geomechanical model itself.

Figure 6.28 shows the comparison of volumetric change near fracture in the plane where production well is located when a surface load is applied at $t = 0^+$. The impacts of varying Young's modulus and Poission's ratio are also observed in this figure. Compared with Figure 6.27, we can see differences in the magnitude of the volume change, and this illustrates the impact of the surface load. The influence of surface load is fairly straightforward to understand as this additional force at the surface would force the reservoir to deform in that particular direction.

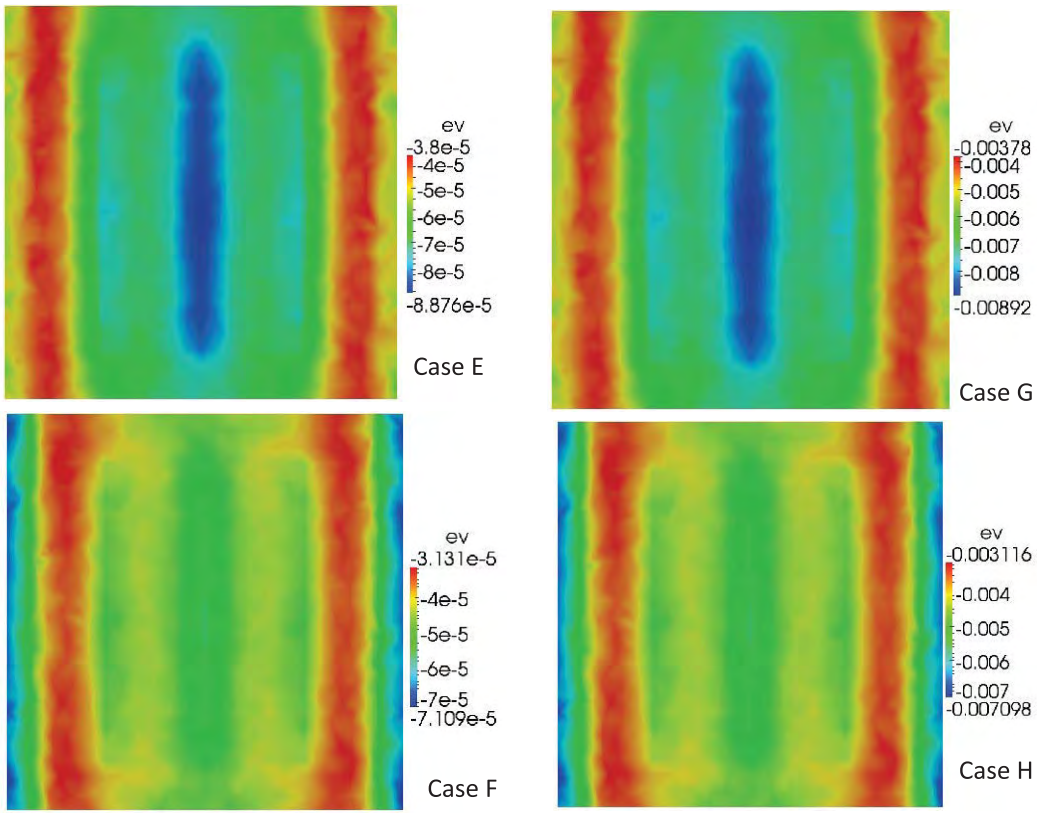

Figure 6.28: Comparison of volumetric change near fractures for case E, F, G and H

Overall, the results for the case studies with surface load are similar to case A, B, C, and D, except in regards to the magnitude of the values (volume change, displacement, etc). Hence, we can conclude that surface load mainly changes the magnitude of the displacement and volume change. Indeed, the results for soft and stiff reservoirs have similar distributions of geomechanical variables like volume change. As a result, only the displacement figures for case C and D are showed to illustrate the displacement distribution in the coupled simulations. Figure 6.29 shows the displacement in x, y and z direction for case C and D. The displacement figures for other cases are similar but with a different magnitude of values.

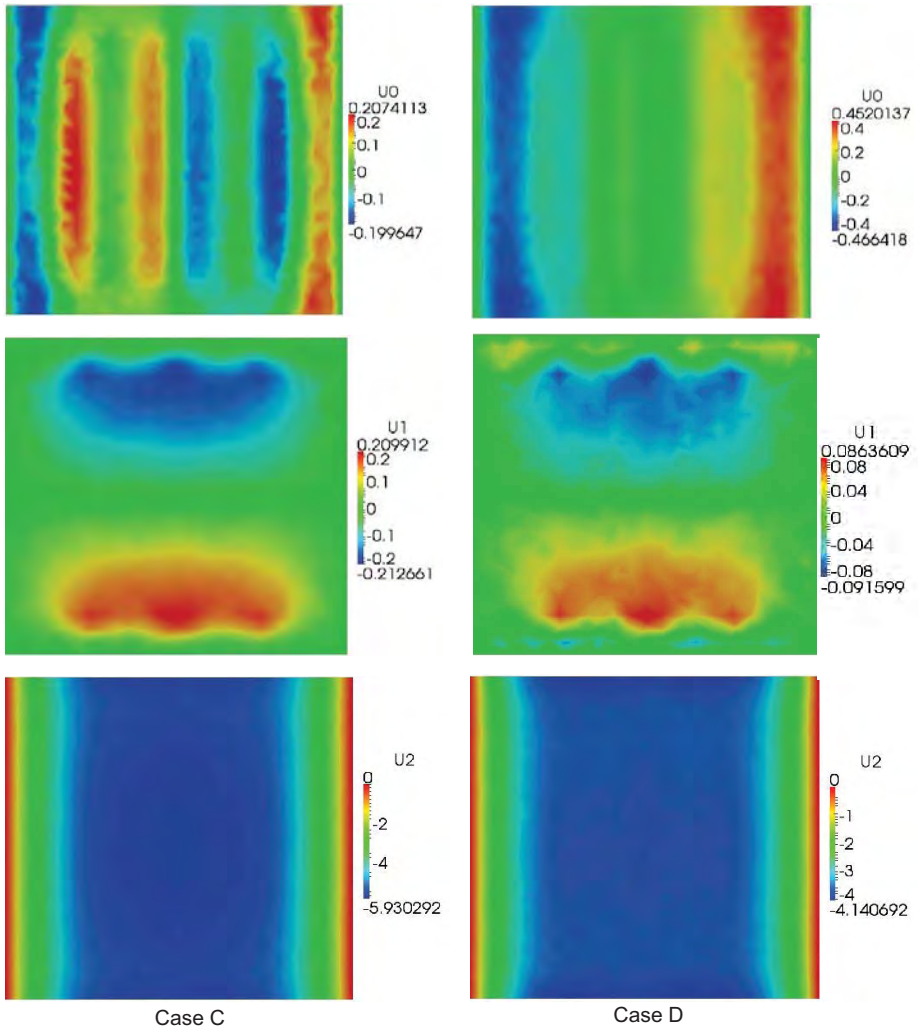

Figure 6.29: Comparison of displacement near fractures for case C and D

The displacement distributions of cases A, B, E, F, G and H have the same patterns compared with case C and D. In Figure 6.29, the difference of displacement distributions for case C and D are well illustrated. The impact of Poission's ratio can be seen again. A relatively large displacement in the vertical direction is seen as well, this means there may be a subsidence in the reservoir during production. The values of the vertical direction displacement may not show the real field scenario as the boundary condition applied in this case (all surfaces are confined expect top surface) does not reflect the real field conditions. In this case, the only way to compensate the pressure change is the deformation of the top surface. In real field simulation, the boundary condition of stress should be given and the value of vertical direction displacement can be larger or smaller than the result seen in this particular case study.

In order to show the impact of varying geomechanical parameters on the production, Figures 6.30 and 6.31 display the instant and cumulative gas productions for case studies listed in Table 6.4. From the production curves, the impacts of different geomechanical parameters on the production are clearly shown, and the complex relationship between volume and permeability changes can be seen again. For example, case G gets less production than the case without geomechanical coupling, which shows that the reducing permeability controls the production process.

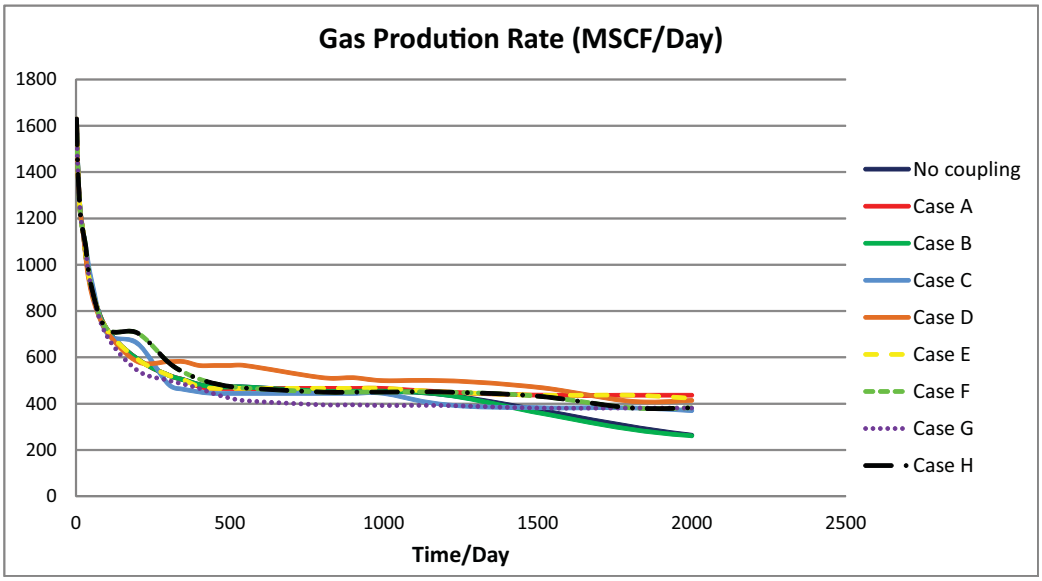

Figure 6.30: Gas production rate for case A, B, C, D, E, F, G, H

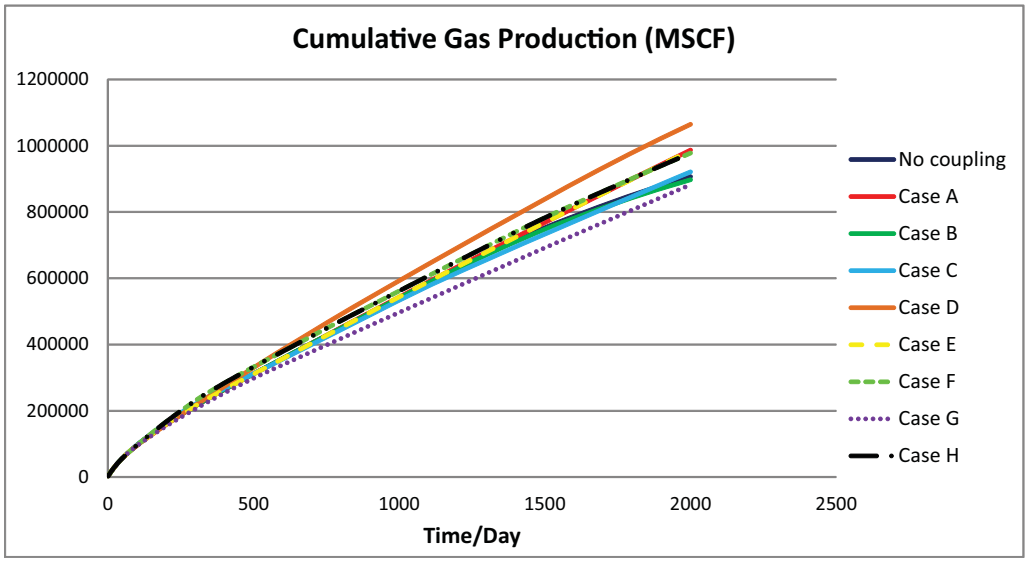

Figure 6.31: Gas production rate for case A, B, C, D, E, F, G, H

In summary, the impacts of different geomechanical parameters and the mechanism for increasing and decreasing production can be seen in the production curves of case studies A to H again. We can conclude that the geomechanical coupling can be a positive or negative factor for production. The varying porosity and permeability are two major factors to determine the overall effect of geomechanical coupling on reservoir simulation and the prediction of production in the coupled model. Indeed, different geomechanical parameters have various impacts on the geomechanical model and hence the reservoir simulation. A set of appropriate geomechanical parameters is needed for the real field reservoir simulation with coupled geomechanics.

6.2.2 Oil Production from Low Permeability Reservoirs

The second reservoir simulation case study performed is the process of producing oil from a low permeability reservoir. The purpose of this simulation is to show the capability of geomechanical coupling with a three-phase black oil model, and the different impacts of geomechanical coupling on oil production are expected to be illustrated. Some important parameters used in this case study are summarized in Table 6.5. The reservoir has extremely low matrix permeability and only has three vertical fractures initially.

Some analysis is stated before the results for the oil production cases are shown. First, the effect of reducing permeability to oil production is supposed to less than that to gas production. The reason is that the viscosity of the oil is much higher than gas, and the

Table 6.5: Summary of important properties of case study for oil production

Discretization method	CVFE	
Geometry information		
L_x, L_y, L_z (ft)	1000,1000,300	
Number of fractures	3	
Number of elements	43666	
Rock property		
ϕ	0.30	
Initial k (mD) for matrix	0.00001	
Initial k (mD) for fracture	1000.0	
Pore compressibility $\left(\frac{1}{psi}\right)$	4.0E-6	
Biot coefficient	1.0	
Young's modulus (psi)	5.8e5	
Poisson's ratio (psi)	0.2	
Rock density $\left(\frac{lb}{ft^3}\right)$	156.0	
Initial conditions		
P (PSI)	5000.0	
S_o	0.8	
S_w	0.2	
RS $\left(\frac{MSCF}{STB}\right)$	1.13	
Boundary conditions		
Top surface load	P (PSI)	6000
Top surface displacement	u (ft)	Not confined
Bottom surface displacement	u (ft)	0
Left surface displacement	u (ft)	0
Right surface displacement	u (ft)	0
Front surface displacement	u (ft)	0
Back surface displacement	u (ft)	0
Well conditions		
Production	BHP (PSI)	1000
Smart well	Constant BHP (PSI)	1000
Location (coordinates)	(300,479,118)	(394,465,126)
(500,480,115)	(586,483,125)	(700,500,148)

mobility term $\frac{KK_r}{\mu}$ is much smaller for oil. Hence, the influence of decreased permeability is relatively small for oil. Indeed, the magnitude of permeability change is relatively small as we see in the gas production case. The dominate factor in predicting the oil production should be the changing pressure due to the porosity (permeability) change, and we expect to see an increase in production as well. Second, the higher permeability ratio between fracture and matrix is important. In this case the matrix permeability is only 0.00001 md and the fracture has a relatively large permeability of 1000 md. This means the fluid flow happens only in the area near fractures. Also, reservoir properties are becoming more heterogeneous due to the introduction of geomechanics. All these factors are important and can potentially change the reservoir production.

Figure 6.32 shows the oil pressure distribution at 2500 days after production, we can see the area where oil pressure declines is near the fracture. Figure 6.33 shows the oil saturation distribution after 2500 days of production and we can see the oil flow mainly occurs in fractures. The pressure and saturation figures are x-y plane view at the surface where $z = 150ft$.

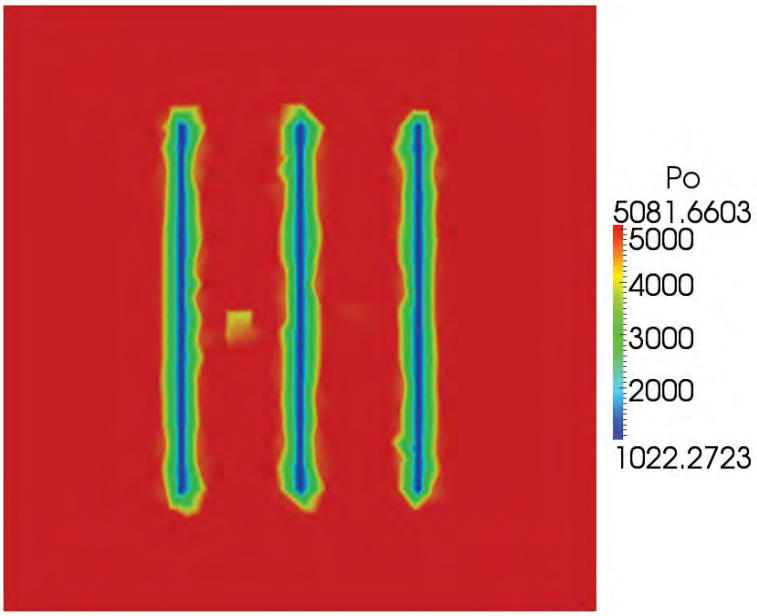

Figure 6.32: Oil pressure distribution at 2500 days with coupled geomechanics (x-y plane $z = 150ft$)

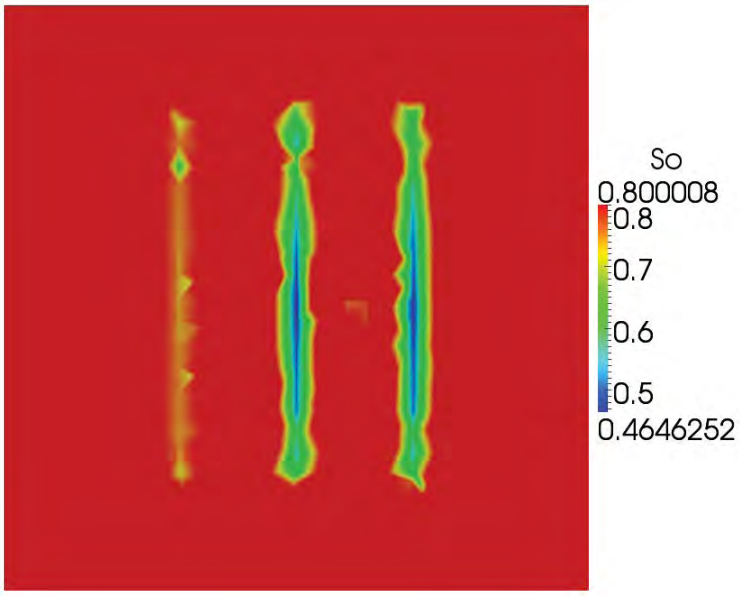

Figure 6.33: Oil saturation distribution at 2500 days with coupled geomechanics (x-y plane $z = 150ft$)

Figure 6.34 shows the average pore pressure for coupled and uncoupled cases, and we can see the coupled case has higher pressure. Figure 6.35 shows the change of permeability in the reservoir after 2500 days of production, and this change is relatively small across the reservoir. As a result of increased pressure and small reduction of permeability, we expect an increase of oil production and this is proved by the simulation results.

As shown in Figure 6.36, coupled simulation result shows a 20% increase of production. This dramatic change is similar with what we saw in the gas production case studies, and shows the combination effect of volume and permeability changes again. The volume change and displacement distributions are shown in figure 6.37. The patterns of volume change and displacement distributions are similar to the case study of gas production, and shrinking pore volumes due to production are observed. The shrinking pore volume can be an additional driving force for oil production and this is also known as compaction driven oil production.

In summary, the case study of oil production from extremely low permeability reservoirs proves the capability of ARTS to perform three-phase black oil simulation with coupled geomechanics. More oil production is predicted by the coupled simulation as a result of additional driving force of decreased pore volume.

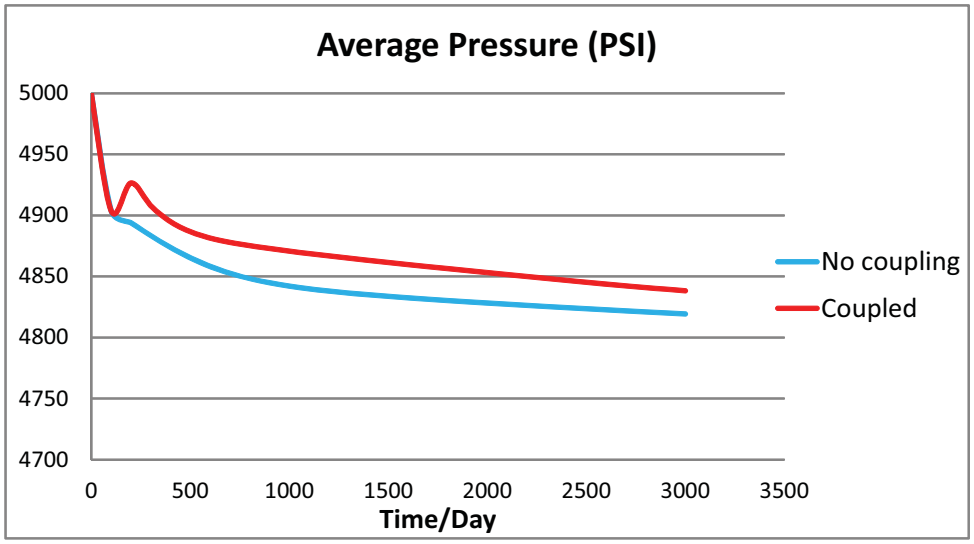

Figure 6.34: Average pressure for the case study of oil production

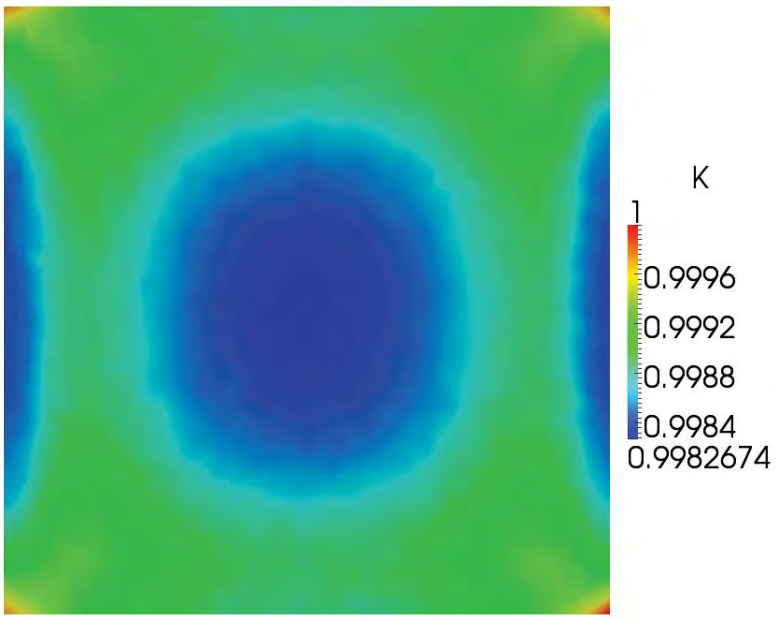

Figure 6.35: $\frac{K}{K_0}$ at 2500 days (x-y plane $z = 150ft$)

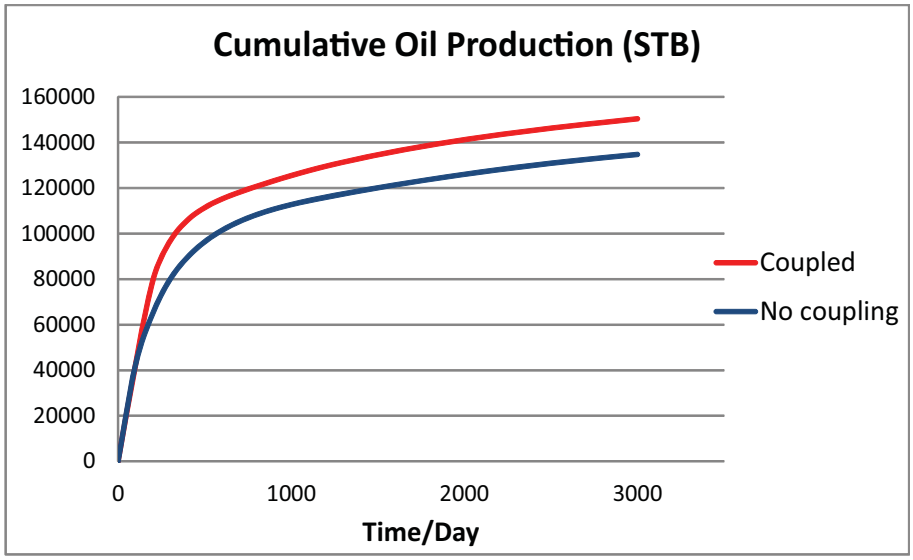

Figure 6.36: Cumulative oil production for case study of oil production

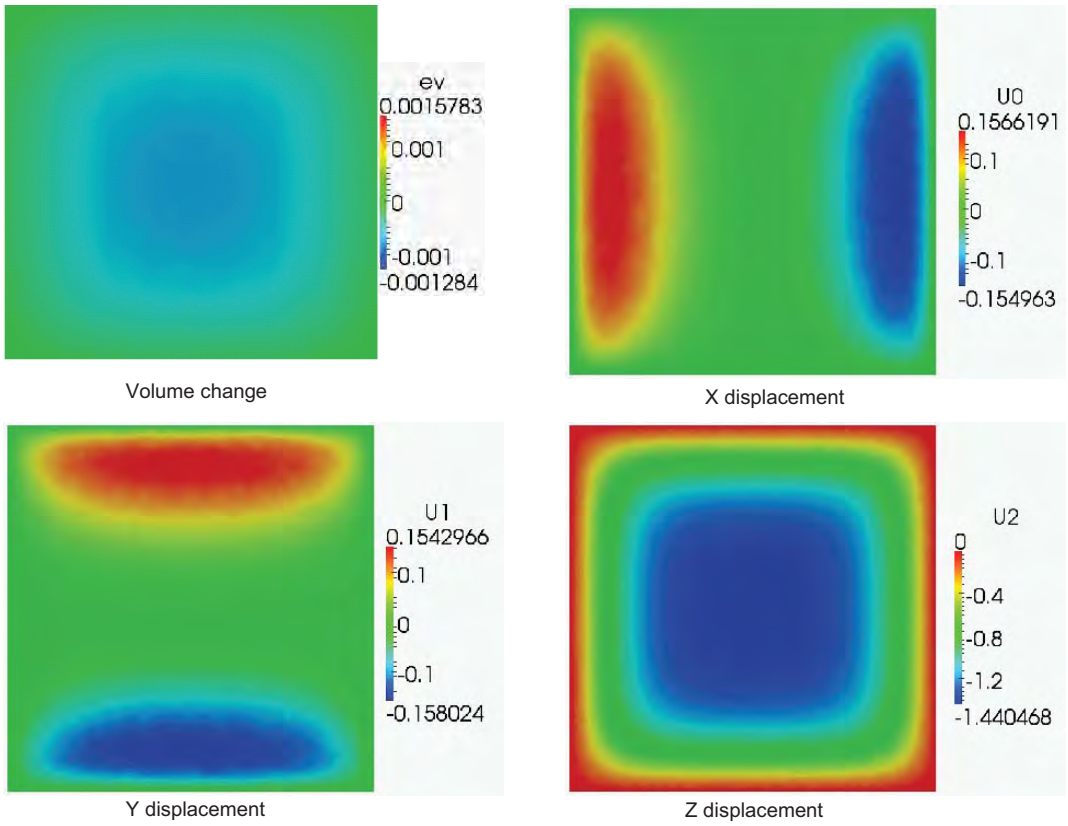

Figure 6.37: Volume change and displacement distribution at 2500 days

6.2.3 Complex Fracture Networks

In previous case studies, the fracture network in the reservoir is relatively simple. However, the real reservoir is always assumed to have complex fracture networks and the impact of geomechanical coupling in those systems is an interesting problem. The goal of this case study is to show the capability of ARTS in simulating complex fracture networks with coupled geomechanics, and some preliminary conclusions of the geomechanical effect in a reservoir with complex fracture networks are drawn. In this case study, a reservoir model which has 44 fractures with different dip angles is created, the basic geometry of the fractured reservoir is shown in Figure 6.38.

As shown in Figure 6.38, the fractures existing in the reservoir are highly connected. This means that more areas with higher permeability exist in the reservoir, and it will have a significant impact on the coupled simulation. The reservoir is assumed to have water and gas in place initially. Some important properties used in this case study are listed in Table 6.6. The matrix permeability is extremely low ($0.00001md$) and the fractures have much higher permeability ($100md$). Nine production wells are located at the top of the reservoir and the production continues for 3000 days.

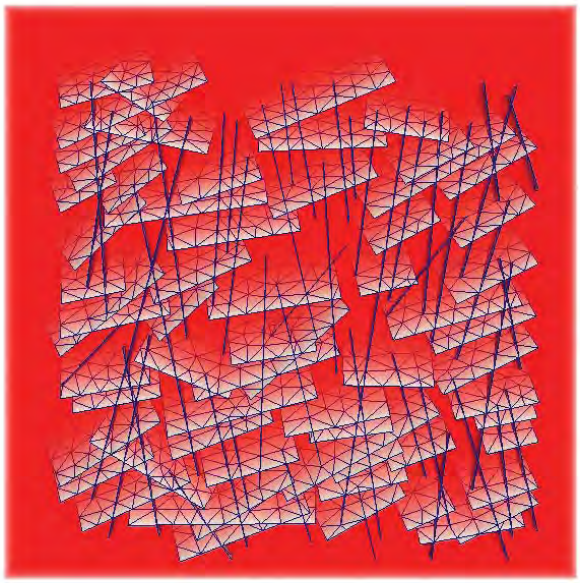

Figure 6.38: Geometry of case study for complex fracture networks

Table 6.6: Summary of important properties of case study for complex fracture networks

Discretization method	CVFE	
Geometry information		
L_x, L_y, $L_z\,(ft)$	1200,1200,200	
Number of fractures	44	
Number of elements	52157	
Rock property		
ϕ	0.20	
Initial $k\,(mD)$ for matrix	0.00001	
Initial $k\,(mD)$ for fracture	100.0	
Pore compressibility $\left(\frac{1}{psi}\right)$	4.0E-6	
Biot coefficient	1.0	
Young's modulus (psi)	1e5	
Poisson's ratio (psi)	0.35	
Rock density $\left(\frac{lb}{ft^3}\right)$	156.0	
Initial conditions		
$P\,(PSI)$	4000.0	
S_w	0.2	
S_g	0.8	
Boundary conditions		
Top surface load	P (PSI)	0
Top surface displacement	u (ft)	Not confined
Bottom surface displacement	u (ft)	0
Left surface displacement	u (ft)	0
Right surface displacement	u (ft)	0
Front surface displacement	u (ft)	0
Back surface displacement	u (ft)	0
Well conditions		
Production	BHP (PSI)	1000
Smart well	Constant BHP (PSI)	1000
Location (coordinates)		
(486,788,200)	(494,532,200)	(470,258,200)
(777,256,200)	(761,256,200)	(786,790,200)
(274,792,200)	(288,531,200)	(258,300,200)

Two sets of simulations are performed. The first simulation is coupled with geomechanics, the second is not. The results from these two simulations are compared to see the geomechanical effect. As we seen in the previous case studies, a positive geomechanical effect is expected in this case study. However, the highly connected fracture networks may change the characteristics of geomechanical coupling. For example, one possible reason for the increasing pressure seen in previous case studies is the relatively low permeability and limited fracture area in the reservoir. This is not valid due to the highly connected fracture networks, and the area of fractures may be large enough to make the reservoir more permeable overall. Furthermore, the geomechanical coupling in these type of reservoirs adds another level of heterogeneity to a heterogeneous system. This makes the system behavior even harder to predict. This case study is an excellent showcase for evaluating the advantage of ARTS in modeling complex fracture network with geomechanical coupling, and we expect a fundamentally different result compared with previous cases.

Figure 6.39 and 6.40 display the gas pressure and saturation distributions at 2800 days after production (coupled geomechanics) in a x-y plane view. The gas pressure and saturation for the uncoupled case is almost the same compared with the coupled case. In order to illustrate the pressure difference between uncoupled and coupled simulations clearly, the variation of average reservoir pressure is shown in Figure 6.41. The pressure differences shown in the result are relatively small, and have both positive and negative values. This is totally different with what we observed in previous case studies and a similar production is expected for these two cases. Figure 6.42 shows the cumulative gas production for coupled and uncoupled cases, and an almost identical production curve is observed. Figure 6.43 shows the difference in cumulative productions between these two cases, and a negligible difference is observed. Indeed, the comparisons of average pressure and cumulative production also illustrate the heterogeneity in the system as the differences observed have both positive and negative values. These results are different than what we saw in previous cases, and the combination effect of fracture networks and geomechanical coupling is the main reason.

Figure 6.44 and 6.45 display the values of $\frac{K}{K_0}$ at 2800 days in the fractures and in the matrix. Figure 6.46 shows the volume change and displacement distribution in the reservoir at 2800 days. The influence of fracture networks is clearly shown, and the heterogeneity in this system can be seen from the volume change and displacement again. This shows that the geomechanical coupling can potentially bring heterogeneity in the reservoir simulation.

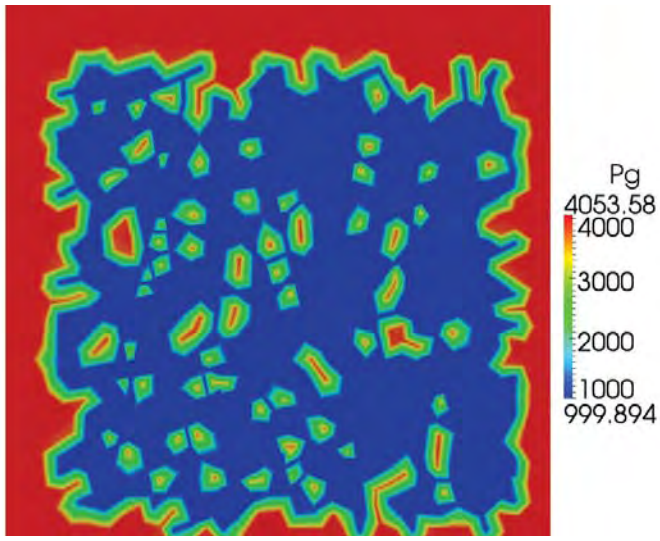

Figure 6.39: Gas pressure distributions at 2800 days with coupled geomechanics (x-y plane $z = 100ft$)

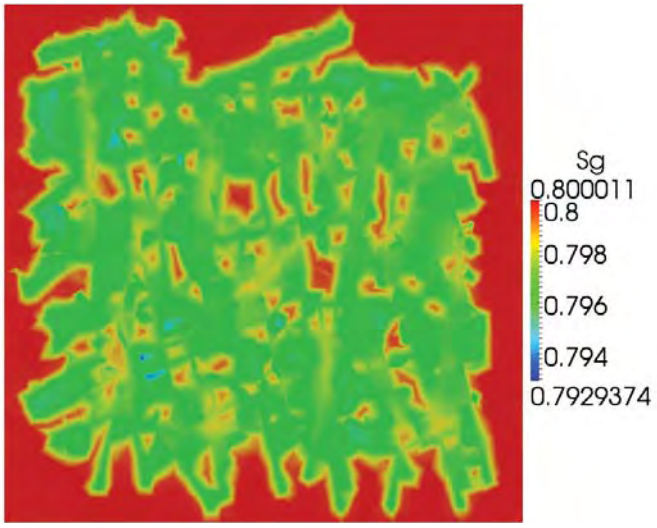

Figure 6.40: Gas saturation distributions at 2800 days with coupled geomechanics (x-y plane $z = 100ft$)

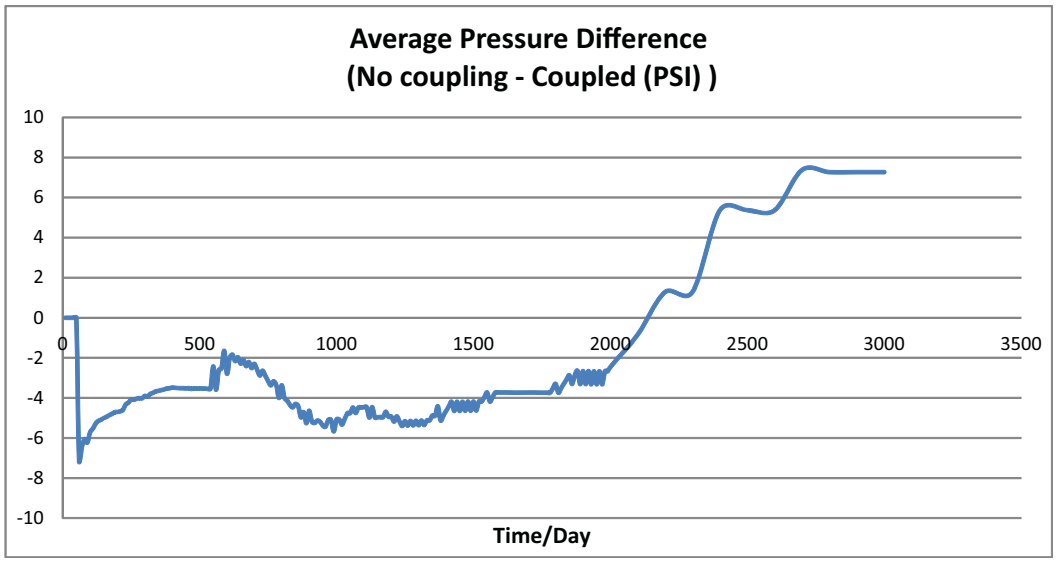

Figure 6.41: Difference of average pressure between coupled and uncoupled cases

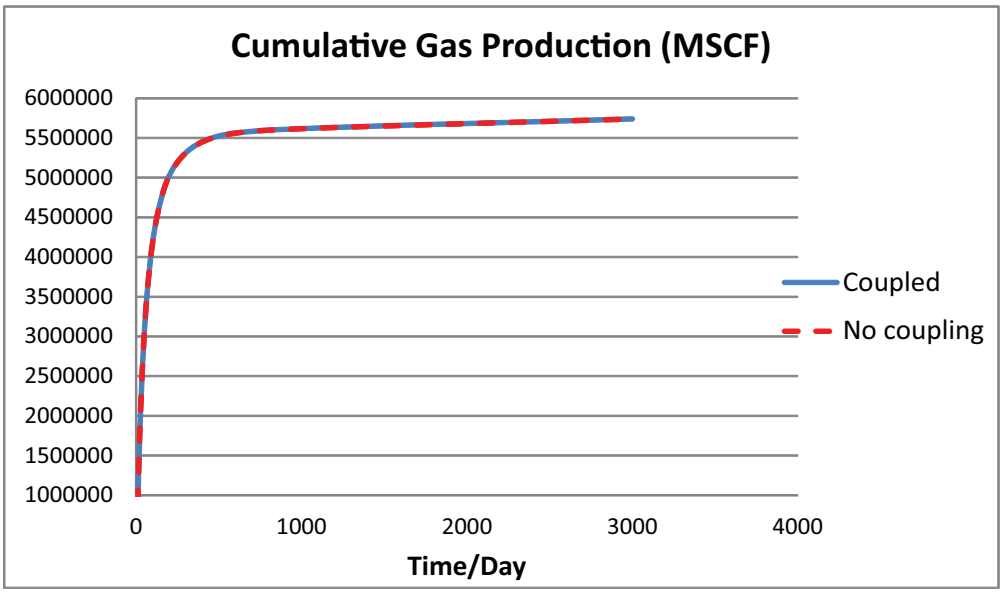

Figure 6.42: Comparison of cumulative gas production

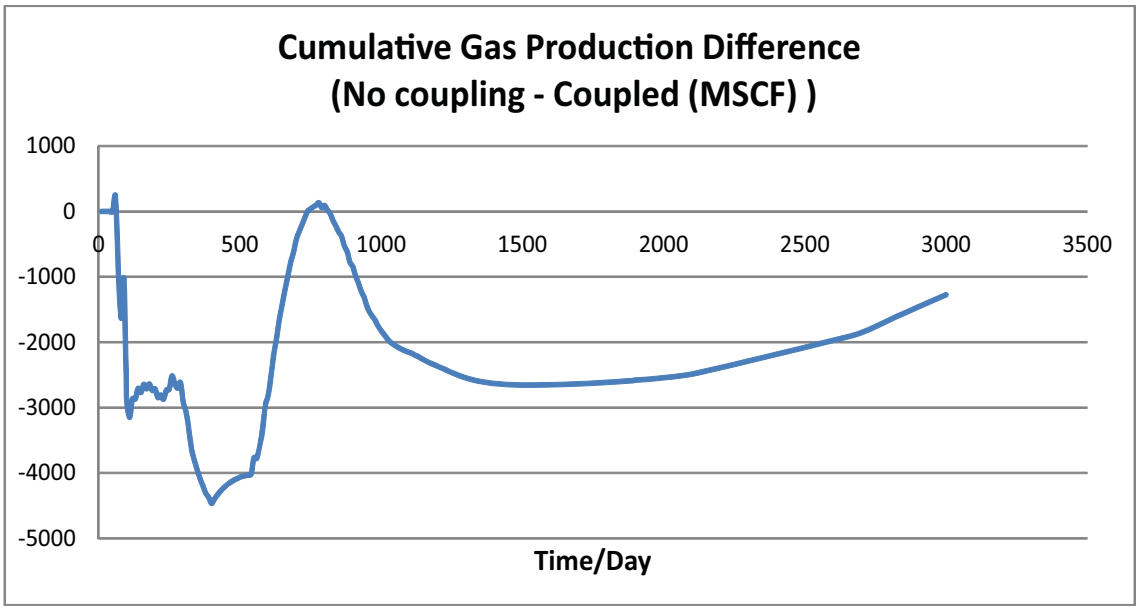

Figure 6.43: Difference of cumulative gas production between coupled and uncoupled cases

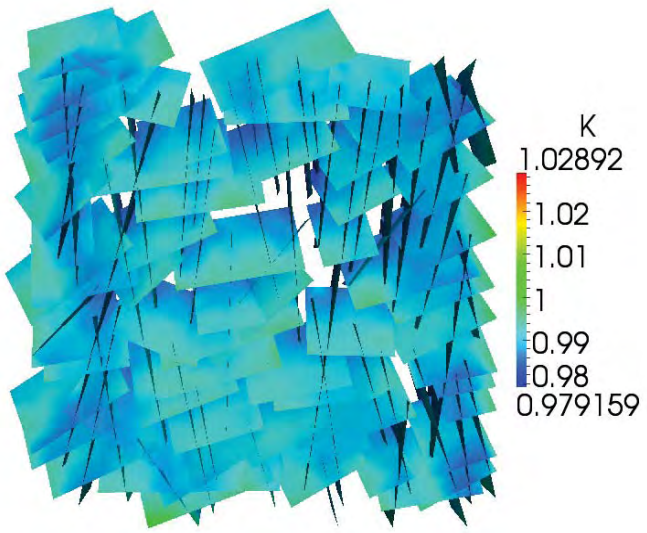

Figure 6.44: $\frac{K}{K_0}$ at 2800 days in fractures

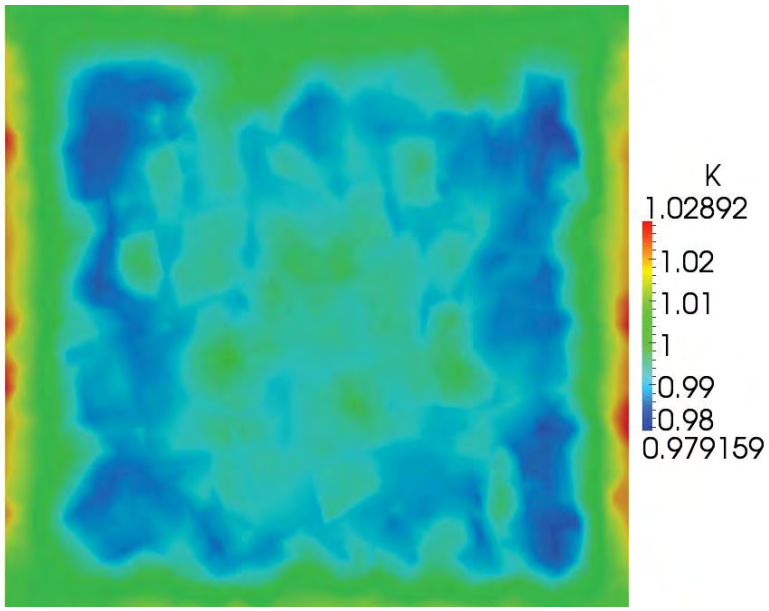

Figure 6.45: $\frac{K}{K_0}$ at 2800 days in matrix

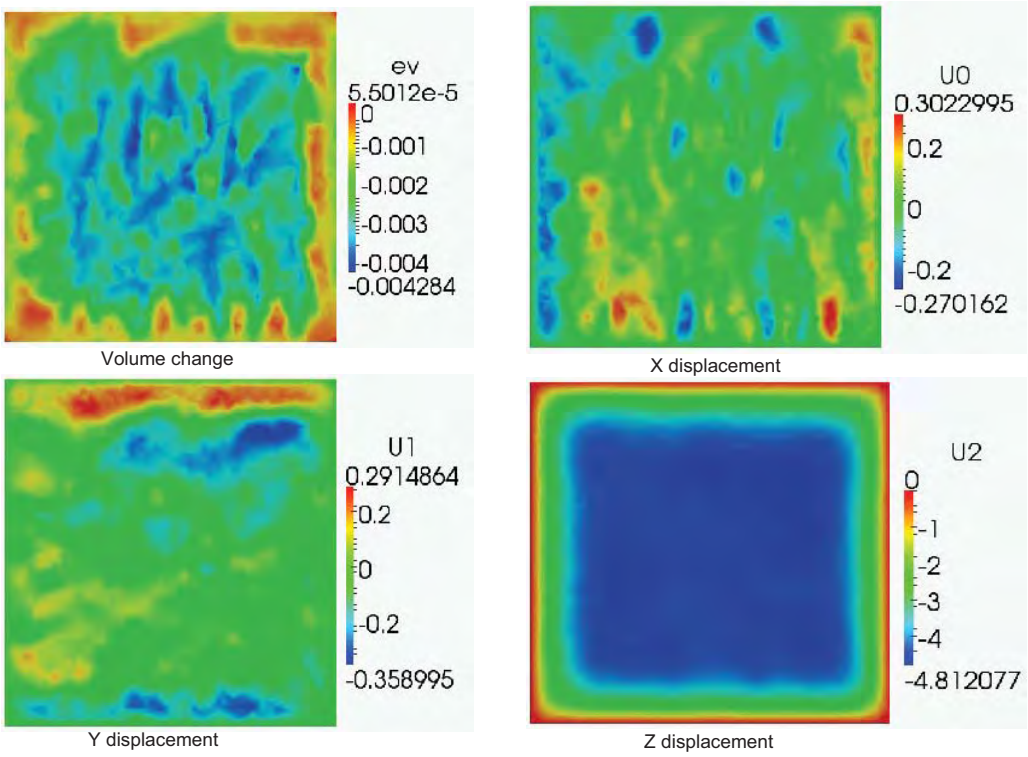

Figure 6.46: volume change and displacement at 2800 day (x-y plane $z = 100ft$)

In summary, this case study demonstrates the capability of ARTS in modeling complex fracture networks with coupled geomechanics. The geomechanical coupling brings heterogeneity in the reservoir system, and the combination effect of geomechanics and fracture networks governs the system. The geomechanical effect in a reservoir with complex fracture networks is fundamentally different from a normal reservoir.

6.2.4 Water Block

As discussed before, water loss has been observed in the field operation and geomechanics is thought to be a factor contributing to this phenomenon. A demonstration case study is designed to learn the possible causes of water loss or how water block happens in the field operation. A reservoir with six major fractures are created, one of the fractures is located in the middle of the reservoir, the other five fractures are perpendicular to this fracture. The matrix permeability is set to be 0.001 md and fractures' permeability is 10 md. The fractures are assumed to be water filled ($S_w = 0.8$), and the matrix has much less water initially. The boundary conditions are adjusted to make the reservoir more deformable overall. Some of the important properties used in this case study are listed in Table 6.7.

Some of the results from the simulation are summarized, Figures 6.47 and 6.48 show the water pressure and saturation distributions at 3000 days. The major pressure depletion area is near the fractures, and there is still a lot of water in the fractures especially vertical fractures at 3000 days. We do not see dramatic difference of the distribution of water pressure for the uncoupled case. In order to illustrates the pressure variation between coupled and uncoupled cases, the average pressure is shown in Figure 6.49. The pressure predicted by coupled model is smaller than that predicted by the uncoupled model. As the average pressure curve suggests, less water production is expected for the coupled model. Figures 6.51 and 6.50 display the instant and cumulative water production curves for uncoupled and coupled simulations. A significant decrease of water production (more than 20%) is observed, and this shows that the water block happening in field operation can be caused by geomechanics.

The volume and permeability change are shown in Figure 6.52 and 6.53. A relatively large change is observed, and this data may not reflect the real field conditions as the demonstration purpose of this case study. We can also see the volume change is large in the area near production well. These results show that the possible reason for declining water production may be the potential closeness of the producing fractures.

Table 6.7: Summary of important properties of case study for water block

Discretization method	CVFE	
Geometry information		
L_x, L_y, L_z (ft)	2000,2000,200	
Number of fractures	6	
Number of elements	56993	
Rock property		
ϕ	0.10	
Initial $k\,(mD)$ for matrix	0.001	
Initial $k\,(mD)$ for fracture	10.0	
Pore compressibility $\left(\frac{1}{psi}\right)$	4.0E-6	
Biot coefficient	1.0	
Young's modulus (psi)	1e5	
Poisson's ratio (psi)	0.35	
Rock density $\left(\frac{lb}{ft^3}\right)$	156.0	
Initial conditions		
$P\,(PSI)$	4000.0	
S_w matrix	0.2	
S_w fracture	0.8	
Boundary conditions		
Top surface load	P (PSI)	6000
Top surface displacement	u (ft)	Not confined
Bottom surface displacement	u (ft)	0
Left surface displacement	u (ft)	Confined in y direction
Right surface displacement	u (ft)	Confined in y direction
Front surface displacement	u (ft)	Confined in x direction
Back surface displacement	u (ft)	Confined in x direction
Well conditions		
Production	BHP (PSI)	500
Smart well	Constant BHP (PSI)	500
Location (coordinates)	(200,1000,100)	(600,1000,100)
(1000,1000,100)	(1400,1000,100)	(1800,1000,100)

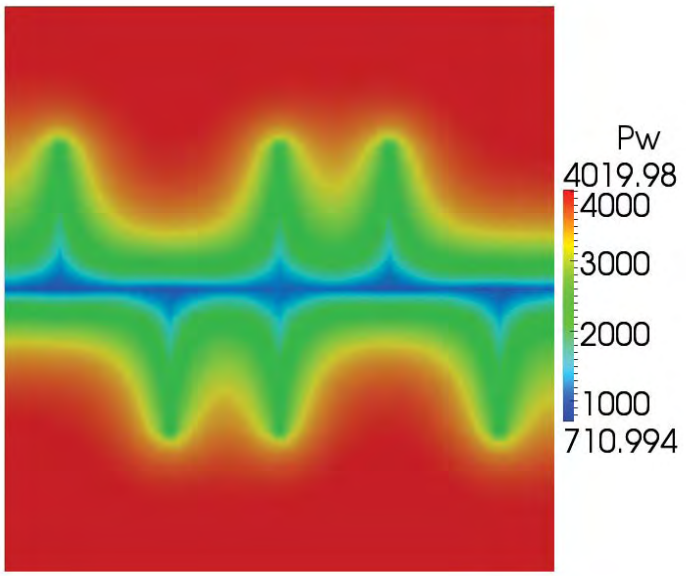

Figure 6.47: Water pressure distribution at 3000 days in the reservoir

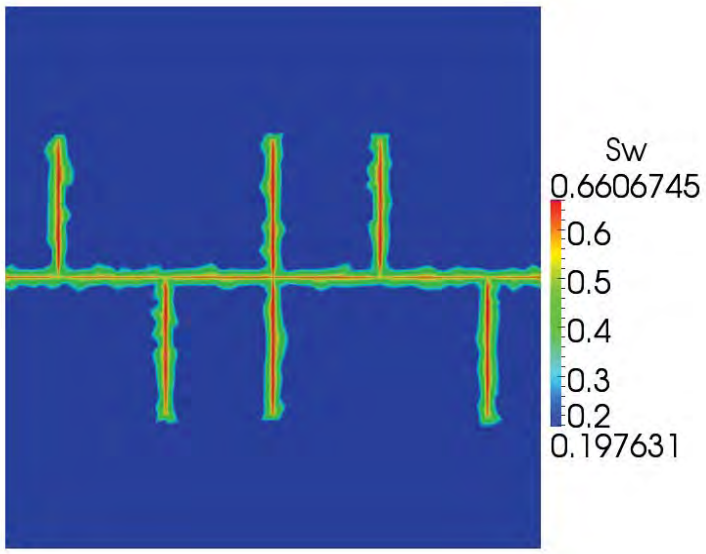

Figure 6.48: Water saturation distribution at 3000 days near production well

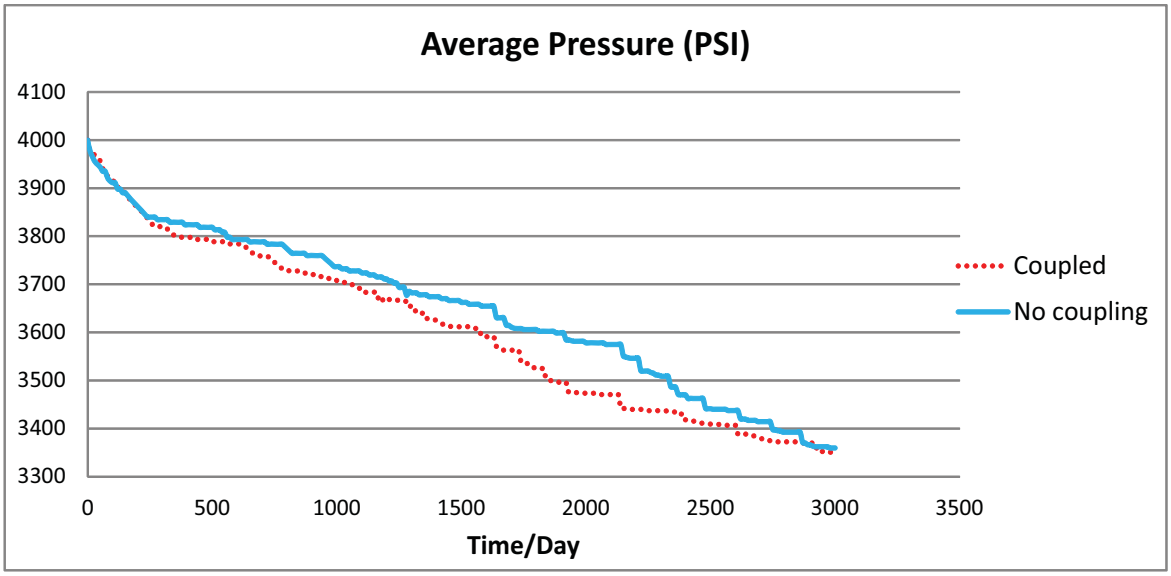

Figure 6.49: Average pressure comparison for water block case study

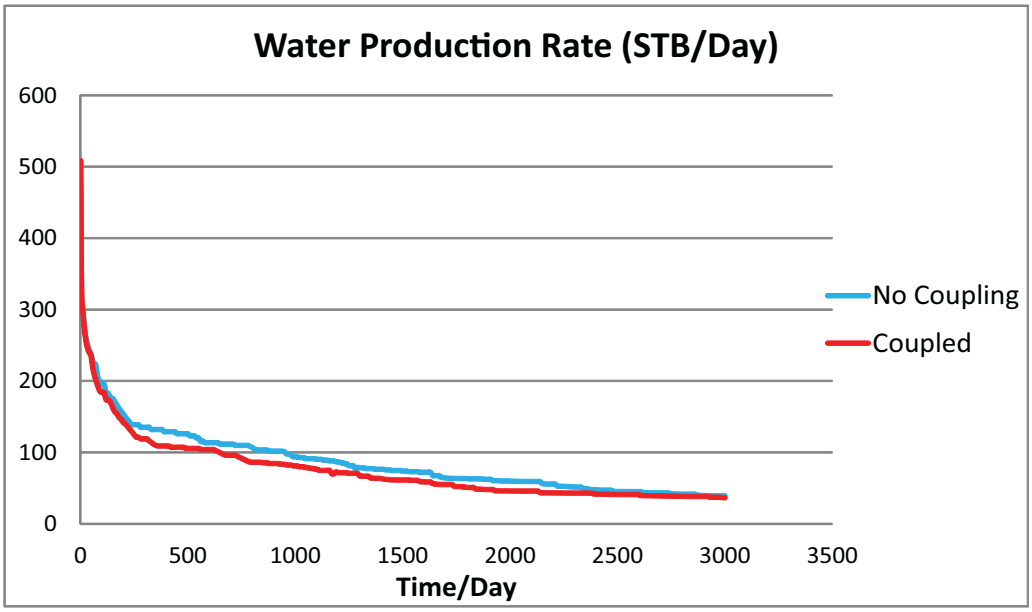

Figure 6.50: Water production rate of water block case study

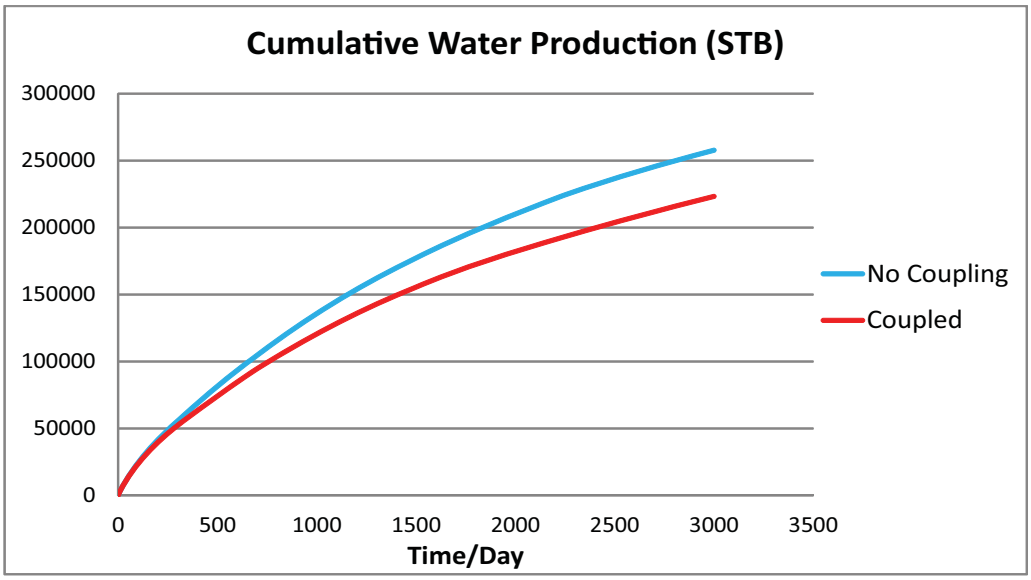

Figure 6.51: Cumulative water production of water block case study

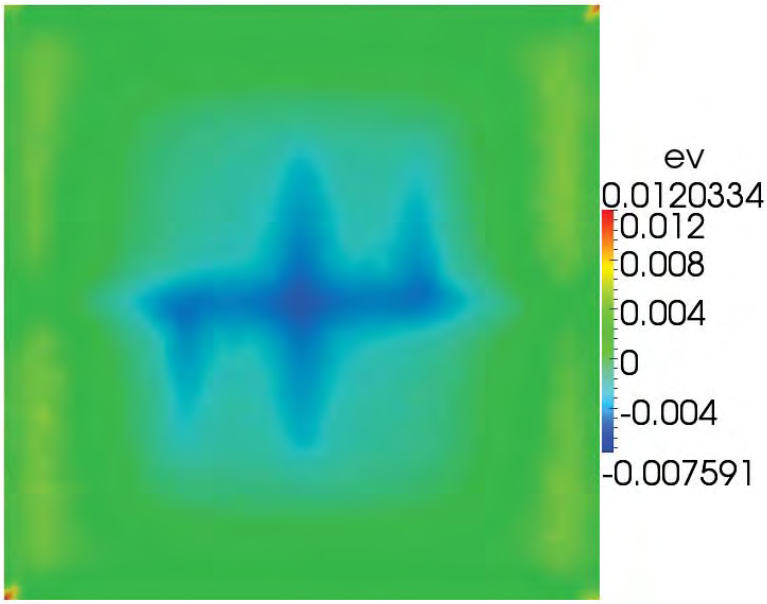

Figure 6.52: Volume change at 3000 days in the reservoir

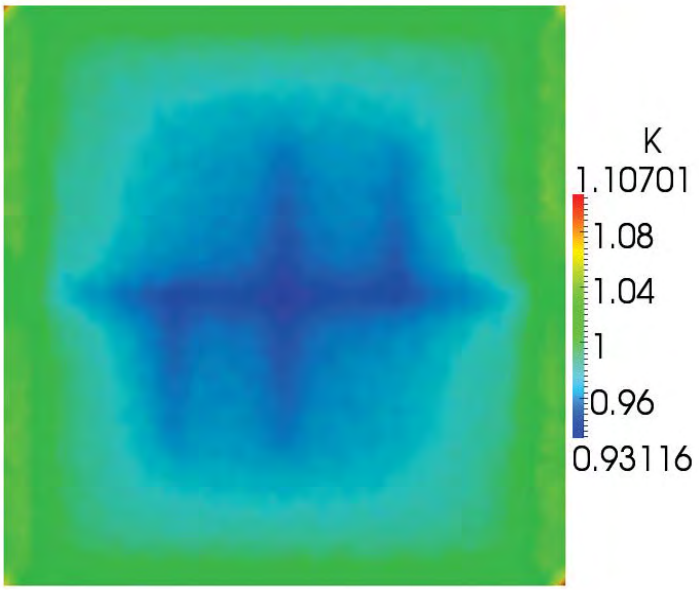

Figure 6.53: $\frac{K}{K_0}$ at 3000 days near production well

Base on the results discussed above, the water may be trapped in the fractures or other natural fractures if the volume change is large enough. The problem is more interesting if different imbibitions are considered. This case study's goal is to demonstrate that the water block can be caused by geomechanics. Additional studies can be performed in ARTS but are not included in this thesis.

In summary, geomechanical effect is a potential factor causing water block in the field operation. This case study supports this through a simple demonstration simulation. ARTS has the capability to simulate this kind of field problems in more detail and helps to find a solution to these problems.

6.3 Summary

In this chapter, several case studies are performed to learn the geomechanical effect in reservoir simulation. We can conclude that the geomechanical coupling is significant and must be considered in an accurate reservoir simulation. All these applications also demonstrate the capability and good performance of ARTS, which is the major purpose of this chapter. ARTS has the potential to simulated a variety of problems with geomechanical coupling, but these applications are not discussed in this thesis. In a word, ARTS is an

effective tool for simulating reservoir transport phenomenons with or without geomechanics. The validity and capability of ARTS is proved through the case studies discussed in this thesis.

CHAPTER 7

SUMMARY AND FUTURE WORK

In this chapter, the summary of the work done in this research is discussed, and some future work is recommended.

7.1 Summary of Research Work

ARTS (Advanced Reactive Transport Simulator) has been developed in this research with geomechanical capabilities. This framework has been verified and validated, through a series of studies. A number of case studies have been performed to understand physical phenomena in tight or unconventional reservoirs. One of the advantages for the geomechanical model in ARTS is the integration of the Discrete Fracture Network (DFN) model. A series of studies has been performed to learn the impact of fractures in unconventional reservoirs. This is a unique and powerful feature in ARTS compared to other simulation tools currently available. The case studies shown that it is important to consider geomechanical effects in certain simulations, particularly when considering simulations with hydraulic and natural fractures.

7.1.1 Major Accomplishments

This research work has three basic contributions: 1). Development of a new generalized reservoir simulation framework. 2) Creation of a geomechanical model within the new framework. 3). Examination of important applications in unconventional oil and gas recovery using the tools developed. This research helped create a better platform for studying unconventional oil and gas reservoir simulation. Some of the important accomplishments and findings of this research are summarized as the following.

1. **Framework development**

   (a) ***Development of ARTS***

   ARTS, a generic and modularized computational framework, is developed in this

research based on the original University of Utah Finite Element Simulators (UFES) with multiple physical models and various discretization methods. A black oil model (single phase, two-phase, three-phase) has been implemented in ARTS. Other models developed in previous research such as compositional K-value thermal model and reactive transport model are also integrated in ARTS. Future modules can be integrated in ARTS efficiently through generic and modularized framework structure. The computation efficiency of ARTS has been improved through the integration of the latest linear solvers and mesh quality control module. Postprocessing codes are developed to visualize results, and several utility tools such as well location selection and production data conversion have also been developed. An entire work flow from the input data to final results has been established in this research through the development of ARTS and other utility tools.

(b) ***Geomechanical model development***

A generic geomechanical model is developed in ARTS using the finite element method. The DFN model is used as the fracture representation method. Several constitutive relationships such as linear poroelasticity and linear thermal poroelasticity are integrated in the geomechanical model. An incremental formulation is used to facilitate the further implementation of nonlinear constitutive relationship. The implementation of the geomechanical model is based on the modularized framework structure of ARTS, and enables effective integration of submodels.

(c) ***Development of soft coupling scheme***

A soft coupling scheme is implemented in ARTS through a look-up table, and this scheme enables communication between ARTS and other geomechanical simulators. 3DEC is used as the external geomechanical simulator to perform soft coupling in this research. The capabilities and usefulness of soft coupling scheme are demonstrated through case studies.

(d) ***Development of hard coupling scheme***

Hard coupling scheme is implemented to couple the reservoir model and the geomechanical model in ARTS. The implementation allows multiple submodels for coupling such as one way, two may and iterative coupling schemes. Iterative

coupling schemes is applied to perform coupled reservoir simulations in this research and has been verified through a variety of case studies.

2. **Verification**

   (a) ***1-D consolidation problem***

   An excellent agreement between the analytical solution and the results from ARTS for a one dimensional consolidation problem is observed. This shows the one-dimensional problem is solved correctly and the right physical phenomena are captured.

   (b) ***2-D consolidation problem***

   The comparison of the simulation result and the analytical solution for a two-dimensional consolidation problem shows the validity of the geomechanical implementation in ARTS. ARTS also captures the pore pressure and deformation response to a surface load correctly.

   (c) ***Indexing method: benchmark with STARS***

   A reservoir with single phase fluid is simulated using ARTS and STARS (commercial reservoir simulator with geomechanics) in three dimensions. A reasonable agreement between the results from those two simulators is observed. ARTS is an unstructured mesh simulator and can be used to solve problems in complex geometry. This shows that ARTS can be used to solve the real field problems and the result from ARTS can be trusted.

3. **Studies of geomechanical impact on reservoir simulations**

   (a) ***Gas production forecasting with soft coupling***

   The impact of using soft coupling was studied in a case where a hydraulic fracture was embedded in a tight naturally fractured reservoir. The geomechanical simulator was 3DEC, and the fracture network properties (permeabilities) were transferred to ARTS as the reservoir pressure changed. It was observed that the gas production increased with soft coupling in comparison to the baseline case where the fracture properties were static. Fracture permeabilities increased and caused this effect. Impact of the presence of the proppant was also examined. When the proppant holds the main fracture open, the gas production decline rate is arrested.

(b) ***Gas production in a fractured reservoir***

The hard coupling scheme of combining geomechanics and flow was used to study the effect of incorporating geomechanics in simulating production of gas in fractured reservoirs. Geomechanical coupling may result in increased or reduced gas production in a fractured reservoir. The decreased pore volume caused by production is a positive factor for production, but the decreased permeability of the entire reservoir (fracture and matrix) may be a negative factor for production. The complex combination effect of the variations of permeability and porosity due to volume changes determines the overall impact of geomechanics on production. Young's modulus was observed to be the most important of the geomechanical parameters in parameter sensitivity studies conducted. Poission's ratio and surface load have limited impact on geomechanical calculation and hence the production.

(c) ***Oil production in a fractured reservoir***

Hard coupling was also used to study the effect of incorporating geomechanics in simulating oil reservoirs. Three-phase black oil model was the physical model used in this study. Geomechanical coupling was observed to increase production in an oil reservoir. Possible reasons are the relatively low mobility of oil and extremely low matrix permeability. The capability of ARTS in performing multiphase reservoir simulation with geomechanics was demonstrated through this case study. Indeed, the extremely low matrix permeability used in the case shows the potential of ARTS in simulating a large variety of unconventional reservoir simulations.

(d) ***Complex fractured reservoirs***

Most of the studies described previously examined situations with only a few fractures. In this study, geomechanics and flow were combined to study gas production in a 44-fracture discrete-fracture network model. The fractures were planes in three dimensions and were assigned arbitrary lengths, angles and penetrations. In this particular case, incorporating geomechanics did not change gas production significantly. The heterogeneity and relatively larger surface area of fractures were primary reasons. The capability and advantage of ARTS in simulating complex fracture networks were demonstrated through this case study.

(e) ***Water block***

Water blockage is a phenomenon where the water occupies certain areas of the fracture network and is trapped when the fracture contracts on pressure depletion. Using ARTS as a tool to study this phenomenon was demonstrated by using a handful of fractures off of a horizontal well. As microseimic sensing is used to pinpoint fracture locations, this type of identification of possible water blockage in exact locations will be particularly applicable.

7.2 Recommendation of Further Work

Possible future work is discussed for three fields. The first includes some elements that are very important to geomechanical simulation but not yet implemented in our model. In the second, some work related to computation efficiency improvement is discussed. Finally, some suggestions are made on future framework development and potential submodels which are needed in reservoir simulation.

1. Geomechanical model:

   (a) ***Nonlinear constitutive relationships***

   The rock or soil media always behaves nonlinearly in the field, it is important to model the nonlinearity in some cases. In ARTS, the geomechanical model is already solved in the incremental form, which is the basis for implementing a nonlinear constitutive relationship. Hence, the nonlinear models can be implemented in ARTS in a fairly easy manner. The computational efficiency may be a potential problem if a nonlinear model is applied.

   (b) ***Nonisotropic geomechanical parameter***

   The mechanical properties of rock are assumed to be isotropic in ARTS. In some cases, nonisotropic parameters are important and it is worth it to implement this functionality in the geomechanical model. The parameter I/O part of geomechanical model and coefficient calculation parts in ARTS need to be modified for the implementation of this functionality.

   (c) ***Dynamical modeling***

   In order to model the fracture growth and propagation in an appropriate way, a dynamical model is needed in ARTS. The difference between the dynamical model and the static model implemented in ARTS, is the time derivative term in the geomechanical model. Some advanced technologies for the discretization of

time are needed to resolve the potential instability involved in adding this term to the governing equations.

(d) ***New fracture representation methods***

One limitation for modeling geomechanics dynamically in ARTS is the fracture representation method. As introduced in the previous chapter, the DFN model, which models the fracture as a surface with no volume, is applied in the geomechanical model. The impact of volume change is limited because the fracture does not have aperture or volume in this model. A modified DFN model, which models the fractures as surfaces with virtual apertures and volumes, is worth implementing in ARTS to overcome this limitation. A accumulation term due to the virtual volume should be added for fractures. In this way, the fracture growth can be simulated using ARTS.

(e) ***Other discretization methods***

The finite element method applied in the discretization of geomechanical governing equations is sufficient in most applications, but more alternative discretization methods have been developed as the running speed is improving. Discrete element method and boundary element method are recommended for implementation in ARTS, to extend the functionality of the geomechanical model. Other methods like material point method and mesh free method are also worth a try in modeling geomechanics. However, in order to take advantage of the integration of the DFN model and geomechanics, only finite element based methods are recommended to be implemented in ARTS.

(f) ***Calibration with field data***

In this study, the framework has been verified and validated with some problems that have known solutions and with the commercial software. This is sufficient to validate the code but a calibration with field data is needed to make this framework applicable in solving field problems. Indeed, the model can be improved based on the calibration of field data, hence a new model can be applied to future study. A work flow can be created in this way as the calibration and model improvement are done iteratively.

2. Computation efficiency improvement:

(a) ***Linear solver improvement***

PETSC and Trilinos are used as the linear solver packages in this research. Generally, these two solvers are stable and fast. However, as the physical problems solved in the framework vary, different schemes need to be implemented to solve different linear systems. Further work is recommended to implement a model to construct different solving schemes and preconditioners for different linear system.

(b) ***Optimization in the assembling process***

Assembling the matrix and vector is a time consuming part in the simulation. The element by element scheme applied in ARTS is efficient and accurate. However, it is still slow when the problem becomes complex. There are some potential methods to optimize the assembling scheme to improve the speed. For example, changing the data structure to store and pass the matrix and vector may improve the speed for the whole process.

(c) ***Nonlinear solver improvement***

As some new technologies are developed for solving a nonlinear system in recent years. It is worth it to implement new schemes in the nonlinear solver model of ARTS. The improvement in nonlinear solver can potentially reduce the running time of simulation, dramatically. Secant method and bisection method are recommended to be implemented in ARTS to improve the running speed in certain scenarios.

(d) ***Alternating implicitness level***

The stability of a numerical solution is related to the implicitness of a formulation. Generally, higher implicitness method is more stable. However, the high implicitness method costs more computational effort since a nonlinear equation is solved in each iteration for all variables. However, it may not be necessary to treat each property with the same implicitness method as some variables are changing much less over time. To optimize the computational efficiency, a function is needed to switch the implicitness level for different variables. It is even possible to apply explicit method for some variables during the simulation. For example, the implicit level should be different for solving the variables near or far away from the well.

3. Framework development:

   (a) ***Independent solver module***

   In order to modularize further, an independent solver module is needed. In this way, future submodels are more easily integrated in ARTS. To implement this, a generalized data structure for matrix and vector needs to be developed to separate the solver from the physical model.

   (b) ***Data sharing module***

   Some data like pressure and saturation are needed in both PM and DM. If DM needs to know pressure from PM, then DM needs to initialize a function to fetch the data and vice versa. A data sharing module may be valuable as the efficiency to pass data in that way is not great. The data sharing module should store the common data in memory level and be a derived module of the modules which need the stored data. In this way, no information passing is needed in the framework.

   (c) ***GUI integration***

   A GUI is needed in order to form an entire work flow from geological data to final reservoir simulation results. A GUI module should be integrated with ARTS for a better user experience. Java and Phyton can be applied to implement the user interface. Also a web-based interface is highly recommended to integrate in ARTS.

   (d) ***Potential future modules***

   In order to apply ARTS to solve more types of reservoir problems, some suggestions are made to implement potential modules in ARTS. Diffusion module is important to learn the mechanism for producing oil from an ultra low permeability system. Adsorption module is also needed in certain gas reservoirs. An equation of state module is recommended to learn gas condensate reservoir. All these modules will make ARTS more powerful in solving the existing problems in reservoir simulations.

REFERENCES

[1] "Natural Gas Annual 2009," Energy Information Administration, Tech. Rep., December 2010.

[2] "Annual Energy Review 2010," Energy Information Administration, Tech. Rep., October 2011.

[3] M. Harrison, P. Campbell, F. Coelho, C. Grecco, C. Ikeocha, X. Wang, and M. Economides, "Natural Gas: Overcoming Limitations Toward Energy Supremacy," presented at SPE Annual Technical Conference and Exhibition, 2006.

[4] A. Settari and V. Sen, "The Role of Geomechanics in Integrated Reservoir Modeling," *The Leading Edge*, pp. 622–627, May 2007.

[5] D. Tran, L. Nghiem, and L. Buchanan, "Aspects of Coupling Between Petroleum Reservoir Flow and Geomechanics," presented at 43rd US Rock Mechanics Symposium 4th U.S.-Canada Rock Mechanics Symposium, 2009.

[6] *ECLIPSE Technical Description*, Schlumberger, 2009.

[7] *STARS User's Guide*, 2011.10 ed., CMG, 2011.

[8] H. Cao, "Development of Techniques for General Purpose Simulators," Ph.D. dissertation, Stanford University, Palo Alto, California, 2002.

[9] M. Parashar, J. Wheeler, G. Pope, K. Wang, and P. Wang, "A New Generation EOS Compositional Reservoir Simulator: Part II — Framework and Multiprocessing," presented at SPE Reservoir Simulation Symposium, Dallas, Texas, June 1997.

[10] J. Wheeler, "Integrated Parallel Accurate Reservoir Simulator (IPARS)," presented at 8th Annual Industrial Affiliates Meeting, 1998.

[11] P. Wang, S. Balay, K.Sepehrnoori, J. Wheeler, J. Abate, B. Smith, and G. Pope, "A Fully Implicit Parallel EOS Compositional Simulator for Large Scale Reservoir Simulation," presented at SPE Reservoir Simulation Symposium, Houston, Texas, February 1999.

[12] X. Gai, R. H. Dean, M. F. Wheeler, and R. Liu, "Coupled Geomechanical and Reservoir Modeling on Parallel Computers," presented at SPE Reservoir Simulation Symposium, Houston, Texas, February 2003.

[13] J. Kim, D. Yang, G. Moridis, and J. Rutqvist, "Numerical Studies on Two-Way Coupled Fluid Flow and Geomechanics in Hydrate Deposits," presented at SPE Reservoir Simulation Symposium, 2011.

[14] H. Florez, M. Wheeler, A. Rodriguez, and J. Palomino Monteagudo, "Domain Decomposition Methods Applied to Coupled Flow-Geomechanics Reservoir Simulation," presented at SPE Reservoir Simulation Symposium, 2011.

[15] L. Thomas, L. Chin, R. Pierson, and J.E. Sylte, "Coupled Geomechanics and Reservoir Simulation," *SPE Journal*, pp. 350–358, December 2003.

[16] M. Bagheri and A. Settari, "Modeling of Geomechanics in Naturally Fractured Reservoirs," *SPE Reservoir Evaluation & Engineering*, pp. 108–118, February 2008.

[17] "The Niobrara: A Look into the Weird Science of Tight, Light Oil Plays," TUDOR-PICKERING HOLT & CO, Tech. Rep., August 2011.

[18] D. Tran, L. Nghiem, L. Buchanan, M. Geilikman, T. Leshchyshyn, S. Hannan, and S.-w. Wong, "Modelling Thermal Geomechanical Effects on Simulation Porosity," presented at 42nd US Rock Mechanics Symposium 2nd U.S.-Canada Rock Mechanics Symposium, 2008.

[19] F. Pan, K. Sepehrnoori, and L. Y. Chin, "A New Solution Procedure for a Fully Coupled Geomechanics and Compositional Rservoir Simulator," 2009.

[20] N. Zhao, J. McLennan, and M. Deo, "Morphology and Growth of Fractures in Unconventional Reservoirs," presented at Canadian Unconventional Resources Conference, 2011.

[21] J. McLennan, D. Tran, N. Zhao, and S. Thakur, "Modeling Fluid Invasion and Hydraulic Fracture Propagation in Naturally Fractured Formations: A Three-Dimensional Approach," presented at SPE International Symposium and Exhibition on Formation Damage Control, 2010.

[22] D. Tran, A. Settari, and L. Nghiem, "New Iterative Coupling between a Reservoir Simulator and a Geomechanics Module," *SPE Journal*, vol. 9, no. 3, pp. 362–369, 2004.

[23] V. Shrivastava, D. Tran, L. Nghiem, and B. Kohse, "Use of Improved Gridding Technique in Coupled Geomechanics and Compositional Reservoir Flow Simulation," presented at SPE Middle East Oil and Gas Show and Conference, 2003.

[24] H. Chang and Y. Chen, "Data Assimilation of Coupled Fluid Flow and Geomechanics via Ensemble Kalman Filter," presented at SPE Reservoir Simulation Symposium, 2009.

[25] P. J. Melchior, *The Tides of the Planet Earth*, 2nd ed. Pergamon, New York, 1983.

[26] O. E. Meinzer, "Compressibility and Elasticity of Artesian Aquifers," *Economic Geology*, vol. 23, pp. 263–291, 1928.

[27] W. E. Pratt and D. W. Johnson, "Local Subsidence of the Goose Creek Oil Field," *Journal of Geology*, vol. 34, pp. 577–590, 1926.

[28] K. Terzaghi and R. B. Peck, *Soil Mechanics in Engineering Practice*. John Wiley, 1996.

[29] K. Terzaghi, *Theoretical Soil Mechanics*. John Wiley & sons, inc.; Chapman and Hall, limited, 1943.

[30] A. Nur and G. Simmons, "Stress-Induced Velocity Anisotropy in Rock: An Experimental Study," *Journal of Geophysical Research*, vol. 74, no. 27, pp. 6667–6674, 1969.

[31] A. Nur and J. Byerlee, "An Exact Effective Stress Law for Elastic Deformation of Rock with Fluids," *Journal of Geophysical Research*, vol. 76, no. 26, pp. 6414–6419, 1971.

[32] M. Boit, "General Theory of Three-Dimensional Consolidation," *Journal of Applied Physics*, vol. 12, 1941.

[33] M. A. Biot, "Theory of Propagation of Elastic Waves in a Fluid Saturated Porous Solid," *Journal of the Acoustical Society of America*, vol. 28, pp. 168–191, 1956.

[34] A. E. Green, "Flow of Fluid Through an Elastic Solid," *Acta Mechanica*, vol. 9, pp. 329–340, 1970.

[35] M. A. Biot, "Mechanics of Deformation and Elastic Propagation in Porous Media," *Journal of Applied Physics*, vol. 33, pp. 1482–1498, 1962.

[36] J. H. Prevost, "Consolidation of Anelastic Porous Media," *Journal of the Engineering Mechanics Division*, pp. 169–186, February 1981.

[37] M. A. Boit, "Theory of Elasticity and Consolidation for a Porous Anisotropic Solid," *Journal of Applied Physics*, vol. 50, pp. 182–185, 1955.

[38] L. Bergamaschi, S. Mantica, and G. Manzini, "A Mixed Finite-Element Volume Formulation of the Black-Oil Model," *SIAM Journal of Scientific Computing*, vol. 20, pp. 970–997, 1998.

[39] J. Latham, J. Xiang, J. Harrison, and A. Munjiza, "Development of virtual geoscience simulation tools, vgest for irregular blocky rock apllications in rock engineering using the combined finite discrete element method, femdem," presented at 44th US Rock Mechanics Symposium and 5th U.S.-Canada Rock Mechanics Symposium, 2010.

[40] *3DEC 4.0 Theoretical Background*, 2009.

[41] Oleg and Vorobiev, "Generic Strength Model for Dry Jointed Rock Masses," *International Journal of Plasticity*, vol. 24, no. 12, pp. 2221 – 2247, 2008.

[42] R. Davis and A. Selvadurai, *Plasticity and Geomechanics*. Cambridge University Press, 2002.

[43] R. M. Sulack and J. Danielson, "Reservoir Aspects of Ekofisk Subsidence," *Journal of Petroleum Technology*, pp. 709–716, July 1989.

[44] R. Sulak, "Ekofisk Field: The First 20 Years," *Journal of Petroleum Technology*, pp. 1265–1271, October 1991.

[45] R. M. Sulack, L. K. Thomas, and R. R. Boade, "3D Reservoir Simulation of Ekofisk Compaction Drive," *Journal of Petrolume Technology*, pp. 1272–1278, October 1991.

[46] J. H. Prevost and L. Chin, "A Constitute Model for Simulating Reservoir Compaction under a Constrianed Stress Path that Leads to High Shear," *Computer Method and Advances in Geomechanics*, pp. 2139–2144, 1994.

[47] D. Allen, "Physical Changes of Reservoir Properties Caused by Subsidence and Repressurizing Operations, Wilmington Field, California," *Journal of Petroleum Technology*, pp. 23–29, 1968.

[48] T. Hegdal, R. Dixon, and R. Martinsen, "Production Forcasting of an Unstable Compacting Chalk Field Using Uncertainty Analysis," *SPE Reservoir Evaluation and Engineering*, vol. 3, pp. 189–196, June 2000.

[49] C. Chase and J. Ditrich, "Compaction within the South Belridge Diatomite," *SPE Reservior Engineering*, pp. 422–428, November 1989.

[50] R. Lewis, "Numerical Simulation of Three-Phase Flow in Deforming Fractured Reservoirs," *Oil & Gas Science and Technology*, vol. 57, no. 5, pp. 499–514, 2002.

[51] K. Aziz and A. Settari, *Petroleum Reservoir Simulation*. London : Applied Science Publishers, 1979.

[52] R. W. Lewis and Y. Sukirman, "Finite Element Modelling of Three-Phase Flow in Deforming Saturated Oil Reservoirs," *International Journal for Numerical and Analytical Methods in Geomechanics*, vol. 17, no. 8, pp. 577–598, 1993.

[53] H. F. Wang, *Theory of Linear Poroelasticity with Applications to Geomechanics and Hydrogeology*. Princeton University Press, 2000.

[54] F. Pan, K. Sepehrnoori, and L. Y. Chin, "Development of a Coupled Geomechanics Model for a Parallel Compositional Reservoir Simulator," 2007.

[55] J. A. White, "Stabilized Finite Element Method for Flow and Geomechanics," Ph.D. dissertation, Stanford University, 2009.

[56] A. Masud and T. J. Hughes, "A Stabililzed Mixed Finite Element Method for Darcy Flow," *Computer Methods in Applied Mechanics and Engineering*, vol. 191, pp. 4341–4370, 2002.

[57] M. Preisig and J. H. Prevost, "Stabilization Procedures in Coupled Poromechanics: A Critical Assessment," presented at 44th US Rock Mechanics Symposium and 5th U.S.-Canada Rock Mechanics Symposium, 2010.

[58] R. Abdel-Ghani, "Single Porosity Simulation of Fractures with Low to Medium Fracture to Matrix Permeability Contrast," presented at SPE/EAGE Reservoir Characterization and Simulation Conference, 2009.

[59] N. Henn, B. Bourbiaux, and M. Quintard, "Modelling Fluid Flow in Reservoirs Crossed by Multiscale Fractures: A New Approach," presented at 7th European Conference on the Mathematics of Oil Recovery, 2000.

[60] M. Oda, "Permeability Tensor for Discontinuous Rock Masses," *Geotechnique*, vol. 35, no. 4, pp. 483–495, 1985.

[61] M. F. Lough, S. H. Lee, and J. Kamath, "An Efficient Boundary Integral Formulation for Flow through Fractured Porous Media," *Journal of Computational Physics*, vol. 143, no. 462-483, 1998.

[62] S. H. Lee, L. J. Durlofsky, M. F. Lough, and W. H. Chen, "Finite Difference Simulation of Geologically Complex Reservoirs with Tensor Permeabilities," *SPE Reservoir Evaluation and Engineering*, vol. 1, no. 6, pp. 567–574, 1998.

[63] C. Hearn, "Simulation of Stratified Waterflooding by Pseudo Relative Permeability Curves," *Journal of Petroleum Technology*, vol. 23, no. 7, pp. 805–813, 1971.

[64] M. Telleria, C. Virues, and M. Crotti, "Pseudo Relative Permeability Functions. Limitations in the Use of the Frontal Advance Theory for 2-Dimensional Systems," presented at Latin American and Caribbean Petroleum Engineering Conference, 1999.

[65] J. E. Warren and P. J. Root, "The Behavior of Naturally Fractured Reservoirs," *SPE Journal*, vol. 3, no. 3, pp. 245–255, 1963.

[66] H. Kazemi, L. Merill, K. Poorterfield, and P. Zeman, "Numerical Simulation of Water-Oil Flow in Naturally Fractured Reservoirs," *SPE Journal*, no. 6, pp. 317–326.

[67] J. R. Gilman and H. Kazemi, "Improvement of Simulation of Naturally Fractured Reservoirs," *SPE Journal*, vol. 23, no. 4, pp. 695–707, 1983.

[68] F. Sonier and R. Eymard, "A New Simulator for Naturally Fractured Reservoirs," presented at SPE Symposium on Reservoir Simulation, San Antonio, Texas, February 1987.

[69] J. E. L. de Guevara Torres, F. R. de la Garza, and A. Galindo-Nava, "Gravity Drainage and Oil Reinfiltration Modeling in Naturally Fractured Reservoir," presented at International Oil Conference and Exhibition in Mexico, Veracruz, Mexico, June 2007.

[70] K. Pruess and T. N. Narasimhan, "A Practical Method for Modeling Fluid and Heat Flow in Fractured Porous Media," *SPE Journal*, vol. 25, no. 1, pp. 15–26, 1985.

[71] B. Bourbiaux, S. Granet, P. Landereau, B. Noetinger, S. Sarda, and J.-C. Sabathier, "Scaling up Matrix-Fracture Transfers in Dual-Porosity Models: Theory and Application," presented at SPE Annual Technical Conference and Exhibition, Houston, Texas, October 1999.

[72] P. Sarma and K. Aziz, "New Transfer Functions for Simulation of Naturally Fractured Reservoirs with Dual Porosity Models," presented at SPE Annual Technical Conference and Exhibition, Houston, Texas, September 2004.

[73] A. C. Hill and G. W. Thomas, "A New Approach for Simulating Complex Fractured Reservoirs," presented at SPE Reservoir Simulation Symposium, Dallas, Texas, February 1985.

[74] L. S. K. Fung and D. A. Collins, "An Evaluation of the Improved Dual Porosity Model for the Simulation of Gravity Effects in Naturally Fractured Reservoirs," *J. Can. Pet. Tech.*, vol. 30, no. 3, pp. 61–68, 1991.

[75] C. R. Wilson and P. A. Witherspoon, "Steady State Flow in Rigid Networks of Fractures," *Water Resources Research*, vol. 10, no. 2, pp. 328–335, 1974.

[76] A. B. Gureghian, "A Study by the Finite-Element Method of the Influence of Fractures in Confined Aquifers," *SPE Journal*, vol. 15, no. 2, pp. 181–191, 1975.

[77] J. Noorishad and M. Mehran, "An Upstream Finite Element Method for Solution of Transient Transport Equation in Fractured Porous Media," *Water Resources Research*, vol. 18, no. 3, pp. 588–596, 1982.

[78] R. G. Baca, R. C. Arnett, and D. W. Langford, "Modelling Fluid Flow in Fractured-Porous Rock Masses by Finite-Element Techiques," *Int. J. Num. Meth. Fluids*, vol. 4, pp. 337–348, 1984.

[79] M. Karimi-Fard and A. Firoozabadi, "Numerical Simulation of Water Injection in 2D Fractured Media using Discrete-Fracture Model," presented at SPE Annual Technical Conference and Exhibition, New Orleans, Louisiana, September 2001.

[80] M. Karimi-Fard, L. J. Durlofsky, and K. Aziz, "An Efficient Discrete-Fracture Model Applicable for General-Purpose Reservoir Simulators," *SPE Journal*, vol. 9, no. 2, 2004.

[81] J. G. Kim and M. D. Deo, "Comparison of the Performance of the Discrete-Fracture Multiphase Model with Those using Conventional Methods," presented at SPE Reservoir Simulation Symposium, Houston, Texas, September 1999.

[82] Y.-K. Yang, "Finite-Element Multiphase Flow Simulator," Ph.D. dissertation, University of Utah, 2003.

[83] Y. Fu, "Multiphase Control Volume Finite Element Simulation of Fracured Reservoirs," Ph.D. dissertation, University of Utah, 2007.

[84] Y. Fu, Y. Yang, and M. D. Deo, "Three-Dimensional, Three-Phase Discrete-Fracture Reservoir Simulator Based on Control Volume Finite Element (CVFE) Formulation," presented at SPE Reservoir Simulation Symposium, 2005.

[85] C.-K. Huang, "Development of A General Thermal Oil Reservoir Simulator Under A Modularized Framework," Ph.D. dissertation, University of Utah, 2009.

[86] Z. Gu, "A Geochemical Compositional Simulator for Modeling CO_2 Sequestration in Geological Formations," Ph.D. dissertation, University of Utah, 2010.

[87] J. E. P. Monteagudo and A. Firoozabadi, "Control-Volume Method for Numerical Simulation of Two-phase Immiscible Flow in Two- and Three-Dimensional Discrete-Fractured Media," *Water Resources Research*, vol. 40, no. 7, pp. 1–20, 2004.

[88] S. K. Matthäi, A. Mezentsev, and M. Belayneh, "Control-Volume Finite-Element Two-Phase Flow Experiments with Fractured Rock Represented by Unstructured 3D Hybrid Meshes," presented at SPE Reservoir Simulation Symposium, Houston, Texas, January 2005.

[89] S. Geiger, S. Matthäi, and J. Niessner, "Black-Oil Simulations for Three-Component-Three-Phase Flow in Fractured Porous Media," presented at EUROPEC/EAGE Conference and Exhibition,, London, U.K., June 2007.

[90] S. Balasubramanian, "A Compositional Model For Fractured Reservoir Simulation," Ph.D. dissertation, University of Utah, 2007.

[91] Y. Yang and M. D. Deo, "Modeling of Multilateral and Maximum Reservoir-Contact Wells in Heterogeneous Porous Media," 2006.

[92] W. Narr, D. Schechter, and L. Thompson, *Naturally Fractured Reservoir Characterization*. Richardson, Texas: Textbook Series, SPE, 2006.

[93] *SCons User Guide 2.1.0*, 2010.

[94] P. J. Deitel and H. M. Deitel, *C++ for Programmers*. Pearson Educational, Inc., 2009.

[95] P. Witherspoon, "Validity of Cubic Law for Fluid Flow in a Deformable Rock Fracture," *Water Resources*, vol. 16, no. 6, pp. 1016–1024, 1980.

[96] B. Li, Y. Jiang, L. Yang, Y. Tanabashi, and X. Xiong, "Evaluation of Validity of Cubic Law And Hydro-mechanical Properties of Rock Fracture Using Coupled Shear-Flow Tests And 3-D Numerical Simulation," presented at 44th US Rock Mechanics Symposium and 5th US-Canada Rock Mechanics Symposium, 2010.

[97] E. Anderson, Z. Bai, C. Bischof, S. Blackford, J. Dongarra, J. Demmel, J. Du Curoz, A. Greenbaum, S. Hamarling, A. Mckenney, and D. Sorensen, *LAPACK Users' Guide*, 3rd ed. SIAM, 1999.

[98] S. C. Chapra, *Numerical Methods for Engineers*. McGraw-Hill Higher Education, 2010.

[99] M. T. Heath, *Scientific Computing An Introductory Survey*, 2nd ed. Scientific Computing, 2002.

[100] R. Plato, Ed., *Concise Numerical Mathematics*. Providence, Rhode Island: American Mathematical Society, 2003.

[101] D. Kincaid and W. Cheney, *Numerical Analysis: Mathematics of Scientific Computing*. American Mathematical Society, 2009.

[102] K. E. Atkinson, Ed., *An Introduction to Numerical Analysis*. New York City, New York: John Wiley & Sons, 1978.

[103] H. Klie, J. Monteagudo, H. Hoteit, and A. Rodriguez, "Towards a New Generation of Physics Driven Solvers for Black Oil and Compositional Flow Simulation," presented at SPE Reservoir Simulation Symposium, 2009.

[104] M. Heroux, R. Bartlett, V. H. R. Hoekstra, J. Hu, T. Kolda, R. Lehoucq, K. Long, R. Pawlowski, E. Phipps, A. Salinger, H. Thornquist, R. Tuminaro, J. Willenbring, and A. Williams, "An Overview of Trilinos," Sandia National Laboratories, Tech. Rep. SAND2003-2927, 2003.

[105] M. A. Heroux and J. M. Willenbring, "Trilinos Users Guide," Sandia National Laboratories, Tech. Rep. SAND2003-2952, 2003.

[106] S. Balay, K. Buschelman, V. Eijkhout, W. Gropp, D. Kaushik, M. Knepley, L. C. McInnes, B. Smith, and H. Zhang, *PETSc Users Manual*, 3.2 ed., Argonne National Laboratory, 9700 South Cass Avenue, Argonne, Illinois 60439, September 2011.

[107] D. Buntinas, G. Mercier, R. Butler, A. Chan, D. Goodell, W. Gropp, J. Krishna, R. Latham, E. Lusk, G. Mercier, R. Ross, and R. Thakur, "MPICH2 Users Guide," Tech. Rep., 2011.

[108] J. R. Fanchi, *Principles of Applied Reservoir Simulations*, 3rd ed. Elsevier, 2006.

[109] Z. Chen, *Reservoir Simulation: Mathematical Techniques in Oil Recovery*. SIAM, 2007.

[110] R. A. Nelson, *Geologic Analysis of Naturally Fractured Reservoirs*. Burlington, Massachusetts: Gulf Professional, 2001.

[111] J. E. P. Monteagudo and A. Firoozabadi, "Control-Volume Model for Simulation of Water Injection in Fractured Media: Incorporation Matrix Heterogeneity and Reservoir Wettability Effects," *SPE Journal*, vol. 12, no. 3, pp. 355–366, 2007.

[112] S. S. Rao, *The Finite Element Method in Engineering*, 2nd ed. Butterworth-Heinemann, 1999.

[113] M. S. Gockenbach, *Understanding and Implementing the Finite Element Method*. SIAM, 2006.

[114] J. N. Reddy, *An Introduction to the Finite Element Method*, 3rd ed. New York City, New York: McGraw-Hill, 2006.

[115] D. L. Logan, *A First Course in the Finite Element Method*, 2nd ed. PWS Publishing Company, 1993.

[116] D. W. Peaceman, "Interpretation of Well-Block Pressure in Numerical Reservoir Simulation," *SPE Journal*, vol. 18, no. 3, pp. 183–194, 1978.

[117] L. S. K. Fung, A. D. Hlebert, and L. X. Nghiem, "Reservoir Simulation with a Control-Volume Finite-Element Method," *SPE Reservoir Evaluation and Engineering*, vol. 7, no. 3, pp. 349–357, 1992.

[118] J. C. Jaeger, N. G. W. Cook, and R. W. Zimmerman, *Fundamentals of Rock Mechanics*, 4th ed. Blackwell, 2007.

[119] D. Znidarcic and R. L. Schiffman, "On Terzaghi's Concept of Consolidation," *International Journal of Rock Mechanics and Mining Sciences Geomechanics Abstracts*, vol. 20, no. 2, pp. A37–A37, 1983.

[120] P. J. Fox, "Solution Charts for Finite Strain Consolidation of Normally Consolidated Clays," *Journal of Geotechnical and Geoenvironmental*, no. October, pp. 847–867, 1999.

[121] E. T. Hanrahan, "The Theory of One-Dimensional Consolidation of Saturated Clays: Discussion," *Canadian Geotechnical Journal*, vol. 19, no. 1, pp. 115–116, 1982.

[122] E. Conte and A. Troncone, "One-Dimensional Consolidation under General Time-Dependent Loading," *Canadian Geotechnical Journal*, vol. 43, no. 11, pp. 1107–1116, 2006.

[123] G. A. Korn and T. M. Korn, *Mathematical Handbook for Scientists and Engineers: Definitions, Theorems, and Formulas for Reference and Review (Dover Civil and Mechanical Engineering)*, 2nd ed. Dover Publications, 2000.

[124] J. Mandel, "Consolidation Des Sols (Étude Mathématique)," *Géotechnique*, vol. 3, no. 7, pp. 287–299, 1953.

[125] C. W. CRYER, "A Comparison of the Three-Dimensional Consolidation Theories of Biot and Terzaghi," *The Quarterly Journal of Mechanics and Applied Mathematics*, vol. 16, no. 4, pp. 401–412, 1963.

[126] R. E. Gibson, A. Gobert, and R. L. Schiffman, "On Cryer's Problem with Large Displacements," *International Journal for Numerical and Analytical Methods in Geomechanics*, vol. 13, no. 3, pp. 251–262, 1989.

[127] A. Selvadurai and A. Shirazi, "MandelCryer Effects in Fluid Inclusions in Damage-susceptible Poroelastic Geologic Media," *Computers and Geotechnics*, vol. 31, no. 4, pp. 285–300, 2004.

[128] J. McKinley, "Coupled Consolidation of a Solid, Infinite Cylinder using a Terzaghi Formulation," *Computers and Geotechnics*, vol. 23, pp. 193–204, 1998.

[129] J. Kim, "Numerical Simulation of the Noordbergum Effect Resulting from Groundwater Pumping in a Layered Aquifer System," *Journal of Hydrology*, vol. 202, no. 1-4, pp. 231–243, 1997.

[130] J. T. Christian and J. W. Boehmer, "Plane Strain Consolidation by Finite Elements," *Journal of the Soil Mechanics and Foundations Division,*, vol. 96, no. 4, 1970.

[131] O. Coussy, *Poromechanics*. John Wiley & Sons Ltd, 2004.

[132] A. H. D. Cheng, Y. Abousleiman, E. Detournay, L. Cui, and J. C. Roegiers, "Mandel's problem revisited," *Géotechnique*, vol. 46, no. 2, pp. 187–195, 1996.

[133] A. W. Skempton, "The Pore-Pressure Coefficients A and B," *Géotechnique*, vol. 4, no. 4, 1954.

[134] L. Cui, A. H. D. Cheng, V. N. Kaliakin, Y. Abousleiman, and J.-C. Roegiers, "Finite Element Analyses of Anisotropic Poroelasticity: A Generalized Madel's Problem and An Inclined Borehole Problem," *International Journal for Numerical and Analytical Methods in Geomechanics*, vol. 20, no. 6, pp. 381–401, 1996.

[135] V. X. Nguyen and Y. N. Abousleiman, "Poromechanics Solutions to Plane Strain and Axisymmetric Mandel-Type Problems in Dual-Porosity and Dual-Permeability Medium," *Journal of Applied Mechanics*, vol. 77, no. 1, 2010.

[136] M. F. Wheeler and X. Gai, "Iteratively Coupled Mixed and Galerkin Finite Element Methods for Poro-elasticity," *Numerical Methods for Partial Differential Equations*, vol. 23, no. 4, pp. 785–797, 2007.

[137] A. P. Boresi and K. P. Chong, *Elasticity in Engineering Mechanics*, 2nd ed. John Wiley & Sons Ltd, 2000.

[138] C. Dennis, T. Bernard, and T. David, "Coupled Hydro-Geomechanical Modelling of the Cold Production Process," presented at SPE International Thermal Operation and Heavy Oil Symposium, 2001.

[139] D. Tran, V. Shrivastava, and L. Nghiem, "Geomechanical Risk Mitigation for CO2 Sequestration in Saline Aquifers," presented at SPE Annual Technical Conference and Exhibition, 2009.